

## University of Southampton Research Repository

Copyright © and Moral Rights for this thesis and, where applicable, any accompanying data are retained by the author and/or other copyright owners. A copy can be downloaded for personal non-commercial research or study, without prior permission or charge. This thesis and the accompanying data cannot be reproduced or quoted extensively from without first obtaining permission in writing from the copyright holder/s. The content of the thesis and accompanying research data (where applicable) must not be changed in any way or sold commercially in any format or medium without the formal permission of the copyright holder/s.

When referring to this thesis and any accompanying data, full bibliographic details must be given, e.g.

Thesis: Jie Xu (2022) " Nonlinear optical frequency generation enabled by 2D structuring of matter", University of Southampton Optoelectronics Research Centre, PhD Thesis, pagination.

Data: Jie Xu (2022) Dataset for Nonlinear optical frequency generation enabled by 2D structuring of matter. <https://doi.org/10.5258/SOTON/D1969>



**University of Southampton**

Faculty of Physical Sciences and Engineering

Optoelectronics Research Centre

**Nonlinear optical frequency generation  
enabled by 2D structuring of matter**

by

**Jie Xu**

ORCID ID 0000-0002-8421-5097

Thesis for the degree of Doctor of Philosophy

January 2022



# University of Southampton

## Abstract

Faculty of Physical Sciences and Engineering

Optoelectronics Research Centre

Doctor of Philosophy

## **Nonlinear optical frequency generation enabled by 2D structuring of matter**

by

Jie Xu

Optical nonlinearity is determined by the structure of materials and, therefore, nanostructuring provides an opportunity to engineer nonlinear optical properties. In this thesis:

- **I have developed the first Coulomb-coupled-oscillator model of nonlinear optical frequency generation in 2D dielectric nanostructures.** The model demonstrates that in the confined geometry of a 2D nanoparticle the collective nonlinear response of the atomic array can arise from the Coulomb interactions of the optical electrons, even if the individual atoms exhibit no nonlinearity.
- **I have discovered that, within the Coulomb-coupled-oscillator model, a 2D nanoparticle's odd order nonlinearities scale with its area, while its even order nonlinearities scale with its perimeter.** This result facilitates the design and optimization of nonlinear dielectric nanostructures for nanophotonics.
- **I have observed that the presence of defects in 2D nanoparticles can lead to harmonic generation within the Coulomb-coupled oscillator model.** The results show that defects have a large influence on even harmonic generation of 2D nanostructures. Information could be encoded in atomic defects via defect engineering and read by its harmonic generation signature.
- **I have demonstrated the first fibre integrated all-dielectric metasurface for second harmonic generation.** The metasurface is a double chevron array that supports a closed-mode resonance for the fundamental wavelength at 1.5  $\mu\text{m}$  with a quality factor of 30. A normalized second harmonic conversion efficiency of  $8 \times 10^{-3}/\text{GW}$  has been demonstrated, exceeding the previously achieved value for a silicon metamaterial by two orders of magnitude.

The results of this thesis can be applied to design nonlinear metamaterials and provide guidance on enhancing and controlling the nonlinear response of nanoscale planar optical devices.



# Table of Contents

<b>Table of Contents</b> .....	<b>iii</b>
<b>Table of Tables</b> .....	<b>vii</b>
<b>Table of Figures</b> .....	<b>ix</b>
<b>Research Thesis: Declaration of Authorship</b> .....	<b>xiii</b>
<b>Acknowledgements</b> .....	<b>xv</b>
<b>Chapter 1 Introduction</b> .....	<b>1</b>
1.1 Motivation .....	1
1.2 Platform for second harmonic generation.....	2
1.3 Symmetry-allowed components of the $\chi^{(2)}$ tensor.....	7
1.4 Second harmonic generation in metamaterials.....	10
1.4.1 Local field enhancement by resonant modes of metamaterials .....	10
1.4.2 Second harmonic generation by metallic and dielectric nanostructures .....	12
1.5 Theoretical models of nonlinearity of films .....	16
1.6 Outline of the thesis .....	17
<b>Chapter 2 Microscopic Coulomb-coupled-oscillator model of optical nonlinearity</b> .....	<b>19</b>
2.1 Introduction.....	19
2.2 Microscopic Coulomb-coupled-oscillator model .....	19
2.3 Taylor expansion .....	21
2.4 Fourier transformation.....	24
2.5 Parameters .....	25
2.6 Summary .....	26
<b>Chapter 3 Model of second harmonic generation due to structuring of centrosymmetric films</b> .....	<b>27</b>
3.1 Introduction.....	27
3.2 Second order nonlinear response in nanostructures of D3 symmetry.....	27
3.3 Effect of particle symmetry on its nonlinearity.....	29
3.4 Effect of particle size on its nonlinearity.....	31
3.5 Optimization strategy.....	32
3.6 Summary .....	34

**Chapter 4 Model of harmonic and sum frequency generation by 2D nanostructures..35**

4.1 Introduction ..... 35

4.2 Harmonic and sum-frequency generation in nanostructures of D4 symmetry ..... 36

    4.2.1 Harmonic and sum-frequency generation in a square particle..... 36

    4.2.2 Electric dipole moment distribution in a square particle ..... 39

    4.2.3 Pump power and size dependence of a square particle’s electric dipole ..... 41

4.3 Harmonic and sum-frequency generation in nanostructures of D3 symmetry ..... 42

    4.3.1 Harmonic generation in a triangle particle..... 42

    4.3.2 Pump power and size dependence of a triangle particle’s electric dipole..... 44

    4.3.3 Sum frequency generation in a triangle particle ..... 46

4.4 Multipole contributions to harmonic generation..... 49

4.5 Discussion..... 51

4.6 Summary ..... 51

**Chapter 5 Model for defects induced nonlinearity in 2D nanostructures.....53**

5.1 Introduction ..... 53

5.2 Modelling defect-induced optical nonlinearity of 2D nanoparticles..... 54

5.3 Defect induced nonlinearity in a square nanoparticle ..... 55

5.4 Effects of defect position ..... 57

5.5 Defect induced nonlinearity in a hexagonal nanoparticle..... 58

5.6 Nonlinear QR codes ..... 60

5.7 Summary ..... 62

**Chapter 6 Design and fabrication of nonlinear fibre-integrated all-dielectric metasurface.....63**

6.1 Introduction ..... 63

6.2 Design of fibre-integrated all-dielectric metasurface..... 63

6.3 Fabrication of fibre-integrated all-dielectric metasurface ..... 67

6.4 Linear optical property characterization ..... 69

6.5 Summary ..... 71

**Chapter 7 Second harmonic generation in a fibre integrated all-dielectric metasurface**



7.1	Introduction.....	73
7.2	Experimental setup for second harmonic generation measurements .....	74
7.3	Second harmonic signal arising from mesoscopic structuring.....	75
7.4	Optical conversion efficiency .....	76
7.5	Contribution of each allowed $\chi^{(2)}$ component .....	79
7.5.1	Pump field .....	79
7.5.2	SHG intensity .....	80
7.5.3	Linear and circular polarization experiments .....	81
7.6	Discussion .....	83
7.7	Summary .....	83
<b>Chapter 8 Conclusions and outlook .....</b>		<b>85</b>
8.1	Conclusion .....	85
8.2	Outlook.....	86
8.2.1	Further improve SH efficiency.....	86
8.2.2	Explore other nonlinear effects .....	88
<b>Appendix A Specifications of major equipment .....</b>		<b>89</b>
<b>Appendix B Multi-resonant silicon metamaterial .....</b>		<b>91</b>
<b>Appendix C Publications .....</b>		<b>93</b>
C.1	Journal publications .....	93
C.2	Conference contributions.....	93
<b>Bibliography .....</b>		<b>95</b>

## Table of Contents

## Table of Tables

<b>Table 1.1</b> Allowed $\chi^{(2)}$ tensor components for 2D point groups .....	8
<b>Table 7.1</b> Comparison of our Si metamaterial with the nearest state of the art .....	78
<b>Table 7.2</b> Second harmonic photon counts for selected pump polarizations.....	81



## Table of Figures

Figure 1.1 Schematic image of metamaterials integrated on fibre .....	2
Figure 1.2 Schematic of second harmonic generation .....	3
Figure 1.3 Classic nonlinear crystals .....	4
Figure 1.4 Surface second harmonic generation .....	4
Figure 1.5 Artificial nonlinear materials.....	6
Figure 1.6 Metamaterials of structures that allow or forbid SHG .....	10
Figure 1.7 Modelled energy of the electric field trapped inside a Si nanoparticle.....	11
Figure 1.8 Enhanced SHG from double resonant plasmonic antenna .....	12
Figure 1.9 Second harmonic generation by a metamaterial with D1 symmetry.....	13
Figure 1.10 SEM images of damaged metallic nanostructures.....	14
Figure 1.11 SHG by a SiN resonant waveguide grating.....	15
Figure 1.12 SHG by metamaterials consisting of C1 symmetry meta-atoms .....	16
Figure 2.1 Model for the optical response of interacting atoms in a dielectric nanoparticle ....	20
Figure 2.2 Schematic of calculating electric dipole via Fourier transformation .....	24
Figure 2.3 A particle cut from two-dimensional material of hexagonal lattice .....	25
Figure 3.1. Second order nonlinear response in a triangular nanoparticle .....	28
Figure 3.2 Symmetry dependence of total linear and second order electric diepole .....	29
Figure 3.3. Second order nonlinear electric dipole distribution in a triangle and a rectangle ....	31
Figure 3.4. Effect of a nanostructure's size on its linear and nonlinear response.....	32
Figure 3.5 Optimization of the second harmonic dipole response via nanostructuring .....	33
Figure 4.1 Harmonic generation in a nanoparticle of D4 symmetry .....	37
Figure 4.2 Sum frequency generation in a nanoparticle of D4 symmetry.....	37
Figure 4.3 Sum frequency generation in a nanoparticle of D4 symmetry.....	38

## Table of Figures

Figure 4.4 Electric dipole moment distribution at harmonic frequencies in a square particle...	39
Figure 4.5 Electric dipole moment distribution at sum frequencies in a square particle .....	40
Figure 4.6 Pump power dependence of a square particle's electric dipole moment .....	41
Figure 4.7 Size dependence of a square particle's electric dipole moment.....	42
Figure 4.8 Harmonic generation in a nanoparticle of D3 symmetry .....	43
Figure 4.9 Pump power dependence of a triangle particle's electric dipole moment.....	44
Figure 4.10 Size dependence of a triangle particle's electric dipole moment .....	45
Figure 4.11 Sum frequency generation in a D3 structure with co-polarized pumping .....	47
Figure 4.12 Sum frequency generation in a D3 structure with cross-polarized pumping.....	48
Figure 4.13 Power radiated by different multipoles as a function of particle perimeter .....	50
Figure 5.1 Defect-induced optical nonlinearity .....	54
Figure 5.2 Harmonic generation in a square nanoparticle without and with defects .....	56
Figure 5.3 Total electric dipole moment as a function of the position of a single vacancy defect	57
Figure 5.4 Harmonic generation in a hexagon nanoparticle without and with single defects ...	58
Figure 5.5 Total electric dipole moment $P$ as a function of defect position .....	60
Figure 5.6 Harmonic generation in a square nanoparticle with atomic defect patterns.....	61
Figure 6.1 Nanostructure design criteria for second harmonic generation.....	64
Figure 6.2 Schematic of the metasurface fabricated from centrosymmetric dielectric .....	64
Figure 6.3 Refractive index of the fabricated amorphous silicon thin film .....	65
Figure 6.4 Simulated transmission spectra and field map of chevron groove pairs .....	66
Figure 6.5 Electric field enhancement at the silicon interfaces .....	67
Figure 6.6 Fabrication process diagram.....	67
Figure 6.7 Nonlinear silicon metamaterial on a fibre tip.....	68
Figure 6.8 SEM images of nonlinear silicon metamaterial on a fibre tip .....	69

Figure 6.9 Experimental setup for transmission measurements.....	70
Figure 6.10 Measured linear transmission spectrum of the metamaterial.....	70
Figure 7.1 Photo and schematic of the experimental setup.....	74
Figure 7.2 Observation of second harmonic generation .....	76
Figure 7.3 Power dependence of second harmonic generation by the metamaterial.....	77
Figure 7.4 Pump polarization angle relative to metamaterial.....	80
Figure 7.5 Contribution of each allowed $\chi^{(2)}$ component .....	82
Figure 8.1 Images of a multi-resonant metamaterial .....	87
Figure 8.2 Linear and nonlinear spectra of the new metamaterial.....	87
Figure 8.3 Transient nonlinear transmission from the new metamaterial.....	88





## Research Thesis: Declaration of Authorship

Print name: Jie Xu

Title of thesis: Nonlinear optical frequency generation enabled by 2D structuring of matter

I declare that this thesis and the work presented in it are my own and has been generated by me as the result of my own original research.

I confirm that:

1. This work was done wholly or mainly while in candidature for a research degree at this University;
2. Where any part of this thesis has previously been submitted for a degree or any other qualification at this University or any other institution, this has been clearly stated;
3. Where I have consulted the published work of others, this is always clearly attributed;
4. Where I have quoted from the work of others, the source is always given. With the exception of such quotations, this thesis is entirely my own work;
5. I have acknowledged all main sources of help;
6. Where the thesis is based on work done by myself jointly with others, I have made clear exactly what was done by others and what I have contributed myself;
7. Parts of this work have been published as journal papers and conference contributions listed in Appendix C.

Signature:

Date: January 2022



## Acknowledgements

Achieving a PhD is one of my life goals. After many years of study, I finally arrive here. During the very long journey, I got countless help and support from my teachers, friends, and families.

I would like to thank my supervisors Prof. Nikolay Zheludev, Dr. Eric Plum and Dr. Vassili Savinov. Pushing optical nonlinear devices down to the nano-scale is an interesting as well as challenging research topic. Professor Zheludev as leading researcher of the field provided me with very important guidance throughout my PhD studies. He helped me solve many key problems. Dr. Eric Plum helped me achieve every milestone during my PhD life, from writing my PhD research proposal till finally finishing my PhD thesis. Especially during Covid time, he gives me great support and helps me keep on the track of achieving my PhD. Dr. Vassili Savinov taught me almost all the skills I needed for my PhD research. When I started my studies, I did not have much knowledge and skills of developing metamaterials. With his patient instruction and demonstration, I learned how to do modelling, fabricate samples on fibres, build an experimental setup and use computer to control it. To some degree, I am a sensitive and emotional person. Dr. Plum and Dr. Savinov always encourage me when I get upset. I am very lucky to have them as my supervisors.

I would like to thank all the members of the Nanophotonics & Metamaterials group. I would like to thank Dr. Jun-Yu Ou. He is a very nice and warm-hearted person, who can always help me find the experimental components I need and gave me much advice on focused ion beam (FIB) fabrication. I would like to thank Hao Li, Jinxiang Li, Dimitrios Papas, Apostolos Zdagkas and Tongjun Liu for sharing all the bright and dark moments of PhD life. We have spent countless happy hours together.

I would like to thank Dr. Alexander Buchnev, Neil Sessions and Libe Arzubiaga Totorika for the training in cleanrooms. I would like to thank Glenn Topley for helping me manufacture sample holders and install optical tables. I would like to thank Dr. Idris Ajia for his help on the experiments.

I would like to thank my friends Dong Wu, Meng Ding, Peipei Chen, Yanjie Zhao, Bingqin Wang, Yifeng Deng, Meng Xia, Xingyuan Zhang, Linxi Chen and Yongmei Li for their company and encouragement.

I would like to thank my family for their great supports, unconditional love and trust. Because of them, I can chase my dreams without burdens and hesitation.

I would like to acknowledge the Chinese Scholarship Council for funding my PhD research.

“The way ahead is long; I see no ending, yet high and low I will search with my will unbending”.

Thank you!

## Acknowledgements

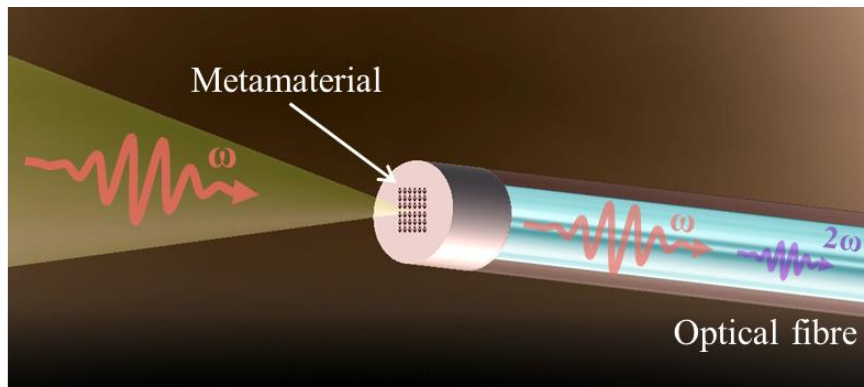
# Chapter 1 Introduction

## 1.1 Motivation

Nonlinear optics is an important branch of modern optics research. Although intensity-dependent absorption was observed in uranium-doped glass in 1926, nonlinear optics has not become important until the invention of the laser in 1960 [1]. Different types of energy exchange between light and matter distinguish nonlinear optics from linear optics. In nonlinear optics, the response of an optical medium is a nonlinear function of the applied electromagnetic field. Nonlinear optics includes various effects, such as optical parametric oscillation (OPO), sum and difference frequency generation as well as harmonic generation. Nonlinear optics has a vast range of applications, such as all-optical information processing, controlling the intensity of lasers by optical switching, and compressing laser pulse widths by Q-switching and mode locking, redistributing optical energy between different carrier wavelengths, as well as developing optical logic devices and optical storage devices.

Metamaterials are a kind of artificial composite materials. The prefix 'meta' is from Greek, which means beyond. The name 'metamaterial' was first used in an article published in 2000 [2]. In the paper, Smith et al. reported a structured material with negative permeability and permittivity at microwave frequencies. In 2001, this research group experimentally verified negative refraction [3], which was first explored by Veselago in 1968 [4]. Metamaterials can exhibit unconventional physical properties [5-9], such as giant, zero or negative refractive indices. Through artificial structuring of materials on the sub-wavelength scale, optical properties of materials can be designed and enhanced according to need. A series of extraordinary properties has been obtained that are unattainable in natural materials. The building blocks of a metamaterial are called meta-atoms or meta-molecules. The size of each meta-molecule and their distance from neighbouring meta-molecules should be on the sub-wavelength scale in order for electromagnetic waves to interact with metamaterials without diffraction as with conventional bulk optical media. Depending on target wavelength range, metamaterials can be divided into microwave metamaterials, terahertz metamaterials and optical metamaterials. The dimensions of meta-molecules of optical metamaterials should be on the order of hundreds of nm. Patterning on such scale is well within the reach of modern nanofabrication techniques. Metamaterials have been exploited in various fields, and have been used to demonstrate exotic photonic devices such as 'superlenses' [10, 11] and electromagnetic cloaks [12, 13], as well as to explore nonlinear optical phenomena [14-18].

A very important feature for nonlinear optics is its sensitivity to symmetry. For example, even order nonlinearity is usually suppressed in materials with inversion symmetry. Therefore, non-centrosymmetric crystals (such as BBO, KDP) are very popular nonlinear media for even order nonlinear processes. Efficient nonlinear effects typically require thick non-centrosymmetric crystals with a strictly controlled orientation of the crystalline axes. These rigid requirements hamper the potential for miniaturization of photonic devices, which in turn limits the speed, efficiency and scalability of photonic technology. Recent progress in the field of metamaterials promises to revolutionize nonlinear optics, by providing a way to achieve desired nonlinear response through nano-scale design. Photonic two-dimensional metamaterials, often referred to as metasurfaces, could offer a great alternative to traditional bulk nonlinear optics. Indeed, even though even-order nonlinearity is forbidden in centrosymmetric media, regular inhomogeneities created in structured metamaterials provide access to efficient even order harmonic generation, especially second order harmonic generation, in structures made from centrosymmetric media [19-28]. Moreover, with the well-developed nanofabrication techniques, metasurfaces can even be fabricated on platforms suited for integration with guided light-waves, see **Figure 1.1**.



**Figure 1.1 Schematic image of metamaterials integrated on fibre**

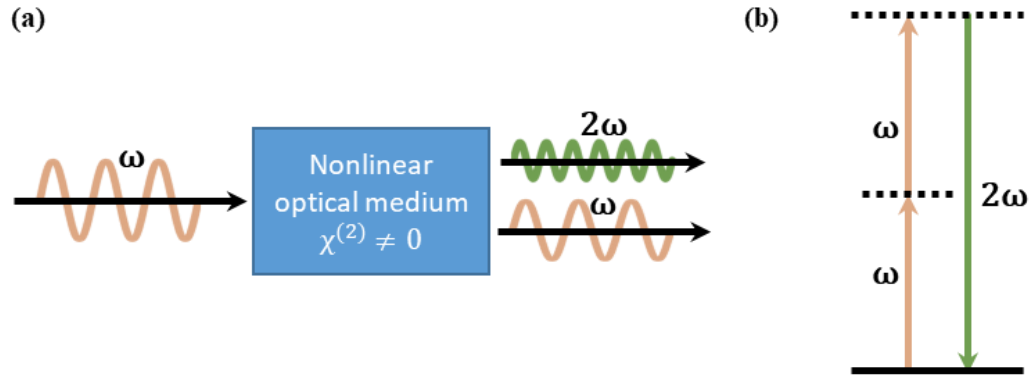
The metamaterial is integrated on a fibre facet and can exhibit a nonlinear effect, such as second harmonic generation.

This thesis focuses on studying structuring induced nonlinearity, both theoretically and experimentally.

## 1.2 Platform for second harmonic generation

Second harmonic generation (SHG) is of key importance for wavelength conversion of optical signals and optical information processing [29, 30]. The achievement of second harmonic generation by Franken et al [31] was a major step forward in the research field of nonlinear optics. Optical second harmonic generation is the conversion of radiation at a fundamental frequency into

radiation at twice the frequency of the fundamental frequency, as shown in **Figure 1.2**. Therefore, the second harmonic generation process is also called frequency-doubling. In the dipole approximation, the optical second harmonic generation process only appears in materials that lack inversion symmetry [32].



**Figure 1.2 Schematic of second harmonic generation**

(a) Schematic of how second harmonic is generated. (b) Energy level scheme of the SHG process [32].

The optical response of matter, including the SHG, arises primarily due to oscillation of electrons, part of the matter, about their equilibrium distribution. Generation of second harmonics can only arise if the potential wells that hold the electrons in place are asymmetric.

Following [32], in media without inversion symmetry, the equation of motion can be described by:

$$m\ddot{x} + 2m\gamma\dot{x} + m\omega_0^2x + max^2 = -qE(t) \quad (1.1)$$

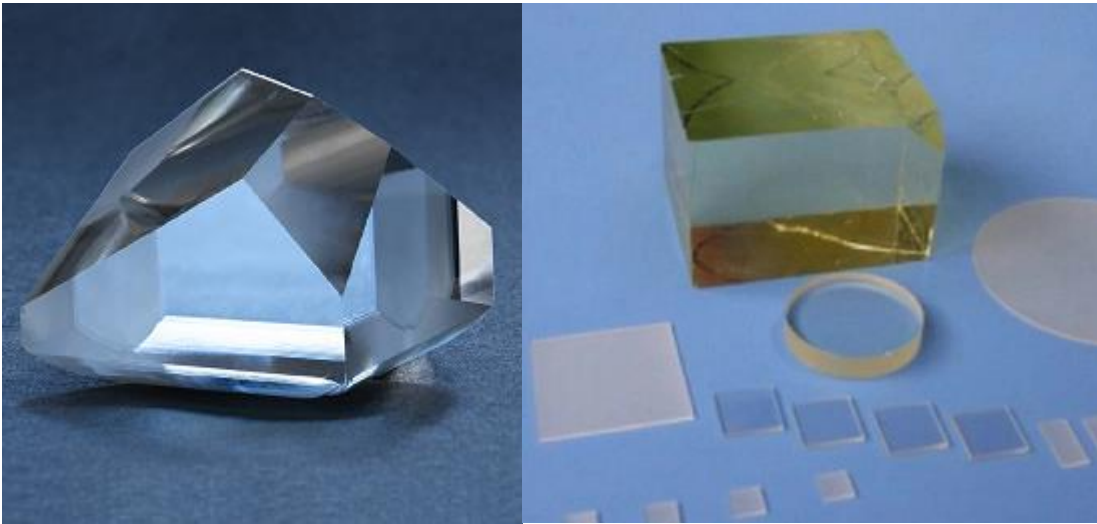
In this equation,  $x$  is the displacement of electron and  $E(t)$  is the applied electric field.  $-q$  is the charge of the electron and  $a$  is a parameter that characterizes the strength of nonlinearity.  $-2m\gamma\dot{x}$  is the damping force and the restoring force is:

$$F_{restoring} = -m\omega_0^2x - max^2 \quad (1.2)$$

Then we can get the potential energy function of the electron:

$$U(x) = -\int F_{restoring} dx = \frac{1}{2}m\omega_0^2x^2 + \frac{1}{3}max^3 \quad (1.3)$$

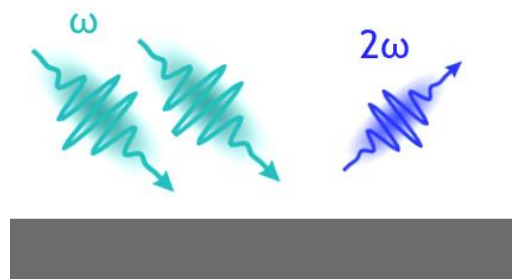
The potential energy function  $U(x)$  contains both even and odd powers of  $x$  for a non-centrosymmetric medium, while for a centrosymmetric medium ( $a=0$ ), only even powers of  $x$  are allowed, because the symmetry requires  $U(x)=U(-x)$ .



**Figure 1.3 Classic nonlinear crystals**

Considering phase matching conditions, nonlinear crystals are usually cut along specific directions. Long crystals can enable high nonlinear efficiency, while short crystals can have a wide phase matching range.

Optical second harmonic generation was first discovered in bulk non-centrosymmetric crystals. SHG was first observed in quartz [31]. With the progress of SHG studies, other frequency-doubling crystals emerged, such as potassium titanyl phosphate (KTP), lithium niobate ( $\text{LiNbO}_3$ ), lithium triborate (LBO), beta barium borate (BBO) as well as potassium dihydrogen phosphate (KDP). **Figure 1.3** shows how typical nonlinear crystals look. The conversion efficiency of these crystals is controlled by phase matching conditions [32] and the crystal nonlinearity. In general, to generate second harmonic signals efficiently, thick non-centrosymmetric crystals with a strictly controlled orientation of the crystalline axes are needed.



**Figure 1.4 Surface second harmonic generation**

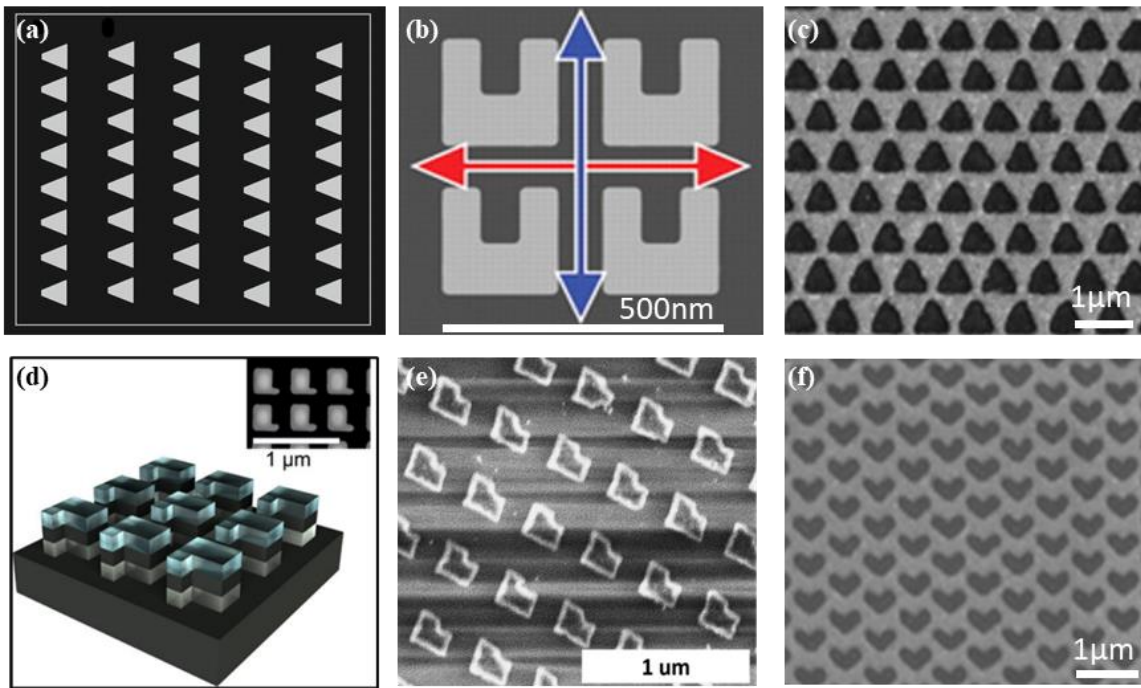
Pumping electric field at frequency  $\omega$  is incident on a surface, exciting a new electric field at frequency  $2\omega$ .

In addition to bulk crystals, the SHG effect is also observed on surfaces and interfaces of materials, where inversion symmetry is broken by the natural discontinuity at the interface [33, 34], see **Figure 1.4**. The surface SHG process has been applied in probing surfaces, interfaces and quality of films



[35]. Electromagnetic waves that propagate along an interface between two media and decay exponentially away from the interface are called surface waves [36]. Although surface SHG only happens in thin layers of surfaces and interfaces, it is still readily observable. Since the surface wave is confined to a thin layer of the order of a wavelength in thickness, at the surface boundary, the surface wave can be very sensitive to small perturbations on the surface. If a large fraction of pumping laser energy can be coupled into the surface wave, the field intensity of a surface wave will become very high [36]. Second harmonic signals have been detected both from metallic and dielectric surfaces, such as silver [37], amorphous silicon films [25, 38, 39] as well as amorphous silicon nitride films [40].

Moreover, photonic two-dimensional metamaterials, often referred to as metasurfaces, offer another alternative to traditional bulk nonlinear optics. Research has shown that even a single layer of nanoscale patterning can be sufficient to modify light [41-47]. Compared with flat films, the nanoscale patterning in a photonic metamaterial increases the sample surface area, which can boost the contribution of surface nonlinearity and introduce inhomogeneity and asymmetry. Besides, metamaterials can be designed to be resonant at the pump wavelength and SH wavelength for enhanced second harmonic generation. Due to these advantages, a variety of structuring enabled nonlinear metamaterials have been demonstrated based on different nanostructures, such as triangle, split ring, and L-shaped structures, using both metallic and dielectric materials [17, 19, 25, 34, 48-50], as shown in **Figure 1.5**.



**Figure 1.5 Artificial nonlinear materials**

Through structuring, inversion symmetry of media can be broken, enabling otherwise forbidden nonlinear processes, such as second harmonic generation. (a) Phase matched SHG from plasmonics [34], (b) SHG from magnetic metamaterial [17], (c) SHG from metal hole arrays [19], (d) SHG from III–V semiconductor metasurface [50], (e) SHG from dielectric metasurface [25] and (f) SHG from L-shaped metallic metamaterial [19].

What are the advantages and disadvantages of these different nonlinear media? The conventional second harmonic crystals offer a high conversion efficiency and are commercially available. However, large size of such crystals hampers the potential for miniaturization of photonic devices. Surfaces of materials support surface SHG but usually require oblique incidence and the conversion efficiency is relatively low [38-40], compared with SHG crystals. However, it can be applied in surface probing and monitoring. 2D metamaterials can enhance the conversion efficiency of second harmonic generation due to surface nonlinearity. Besides, the two-dimensional nature of ultrathin metasurfaces allows for more compact optical devices made from a wider selection of readily available materials, such as silicon. The miniaturization offered by photonic metasurfaces will enable denser integration of all-optical information processing devices (important in the context of data-centres). However, 2D metamaterials are not yet widely commercially available.

### 1.3 Symmetry-allowed components of the $\chi^{(2)}$ tensor

We already know that nonlinear optics is sensitive to symmetry [32, 51]. Now, we will discuss in detail how the symmetry of structures affects second order nonlinearity.

The second order response of a material to applied electric fields can be described by the following **Equation 1.4** [32]. Summation is implied over the repeated indices:

$$P_i^{(2)} = \varepsilon_0 \chi_{i,j,k}^{(2)} E_j E_k \quad (1.4)$$

Where  $P_i^{(2)}$  is the induced second order nonlinear polarization.  $E_j$  and  $E_k$  are the applied electric fields.  $\varepsilon_0$  is the vacuum permittivity.  $\chi_{i,j,k}^{(2)}$  is the second-order nonlinearity susceptibility tensor (with rank of 3). For simplicity we assume the Cartesian basis with  $[i,j,k]=[x,y,z]$ .

For equation above to be apt description of a physical process, it must be the same for any observer. Consider the change in the quantities of **Equation 1.4** as a result of changing the reference frame, i.e. considering the physical process from the point of view of a different observer. The new quantities will be  $P_i^{NL} \rightarrow P_i'^{NL}, E_i \rightarrow E_i', \chi^{(2)} \rightarrow \chi'^{(2)}$ . However, for it to be a consistent description of the physical process, the **Equation 1.4** must still be the same, i.e.:

$$P_i'^{NL} = \chi_{i,j,k}'^{(2)} E_j' E_k' \quad (1.5)$$

It is well-known that electric field and polarization density transform as polar vectors under change of reference frame [52]. Let such transform be given by matrix  $M_{iq}$ , i.e.:

$$E_i \rightarrow E_i' = M_{iq} E_q \quad (1.6)$$

$$P_i^{NL} \rightarrow P_i'^{NL} = M_{iq} P_q^{NL} \quad (1.7)$$

In order for **Equation 1.4** to be invariant (under change of reference frame) it follows that  $\chi^{(2)}$  must transform as (i.e. like a rank-3 polar tensor [51]):

$$\chi_{i,j,k}'^{(2)} = M_{iq} M_{jv}^{-1} M_{kw}^{-1} \chi_{q,v,w}^{(2)} \quad (1.8)$$

Periodic structures such as crystals (usually 3-dimensional) or metasurfaces (2-dimensional) can be classified into point groups [53]. Point transformation is a transformation that keeps one point fixed, i.e. rotations and reflections. Point group of a crystal/metamaterial is a group of point symmetries that leave the structure unchanged. There are two families of 2D point group, cyclic groups and dihedral groups. The cyclic groups  $C_n$  ( $C_1, C_2, C_3, C_4, C_6$ ) have  $n$ -fold rotational symmetry, while the dihedral groups  $D_n$  ( $D_1, D_2, D_3, D_4, D_6$ ) have  $n$ -fold rotation and reflection symmetry. According to Neumann's principle [54], if a material is invariant with respect to certain symmetry operations,

Chapter 1

any of its physical properties must also be invariant with respect to the same symmetry operations, which means the second-order tensor should not change under point group symmetry operations. This translates into the following selection rule [51]:

$$\chi_{i,j,k}^{(2)} = M_{iu}M_{jp}^{-1}M_{kt}^{-1}\chi_{u,p,t}^{(2)} \tag{1.9}$$

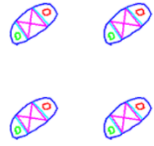


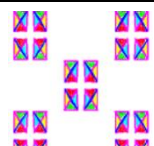
For purposes of second-harmonic generation, the second order susceptibility tensor is also restricted by its intrinsic permutation symmetry [32] - the second order susceptibility is unchanged by interchange of its last two indices:

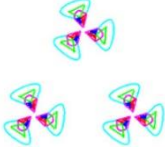
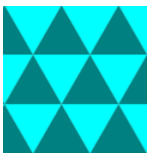

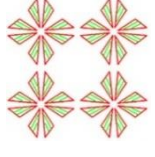

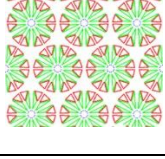
$$\chi_{i,j,k}^{(2)} = \chi_{i,k,j}^{(2)} \tag{1.10}$$

$$P_i^{(2)} = \epsilon_0\chi_{i,j,k}^{(2)}E_jE_k = \epsilon_0\chi_{i,k,j}^{(2)}E_kE_j \tag{1.11}$$

Based on the transformation properties of the susceptibility tensor as well as the intrinsic permutation symmetry, the allowed components of  $\chi^{(2)}$  tensor components for all 2D point group symmetries are found, shown in **table 1.1**. Here we consider the allowed second order nonlinear responses of a periodic 2D structure in the xy plane, for illumination along z.

**Table 1.1** Allowed  $\chi^{(2)}$  tensor components for 2D point groups

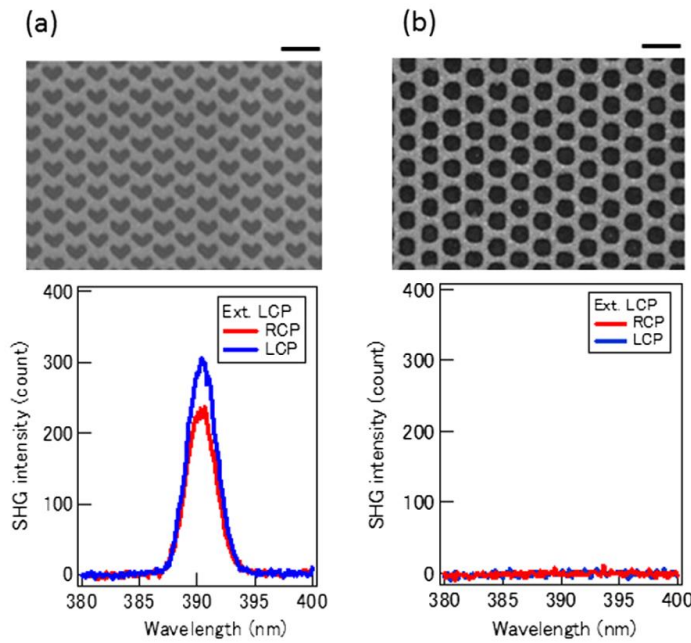
2D Point group	Example	Number of allowed $\chi^{(2)}$	Allowed $\chi^{(2)}$ components
C1		6	$\chi^{(2)}_{xxx}, \chi^{(2)}_{xyy}, \chi^{(2)}_{yxx}, \chi^{(2)}_{yxy} = \chi^{(2)}_{yyx},$ $\chi^{(2)}_{.xy} = \chi^{(2)}_{.yx}, \chi^{(2)}_{.yy}$
D1		3	$\chi^{(2)}_{.xy} = \chi^{(2)}_{.yx}, \chi^{(2)}_{.yxx}, \chi^{(2)}_{.yyy}$
C2		0	
D2		0	

C3		2	$\chi^{(2)}_{yxx} = \chi^{(2)}_{xxy} = \chi^{(2)}_{xyx} = -\chi^{(2)}_{yyy},$ $-\chi^{(2)}_{xxx} = \chi^{(2)}_{xyy} = \chi^{(2)}_{yyx} = \chi^{(2)}_{yxx}$
D3		1	$\chi^{(2)}_{yxx} = \chi^{(2)}_{xxy} = \chi^{(2)}_{xyx} = -\chi^{(2)}_{yyy}$
C4		0	
D4		0	
C6		0	
D6		0	

The images are from Wikipedia: Wallpaper group ([https://en.wikipedia.org/wiki/Wallpaper\\_group](https://en.wikipedia.org/wiki/Wallpaper_group))

From **Table 1.1**, C2, D2, C4, D4, C6 as well as D6 symmetries have no symmetry-allowed second order  $\chi^{(2)}$  tensor. Only the C1, D1, C3 and D3 symmetries have non-vanishing  $\chi^{(2)}$  components.

The symmetry dependence of second harmonic generation has been explored in L-shaped [19, 55], T-shaped [56] and triangular shaped nanostructures [19] or even more complicated shapes [57] and their results follow the symmetry selection rules for second harmonic generation. For example, in **Figure 1.6**, the author reported second harmonic generation from a L-shaped-hole array (C1 symmetry) sample and no SHG was observed in a circular-hole array (D6 symmetry) sample with normally incident left circular polarization (LCP) pump beam.



**Figure 1.6 Metamaterials of structures that allow or forbid SHG**

Scanning electron microscopy (SEM) images and measured SHG spectra with LCP excitation of (a) L-shaped-hole-array sample and (b) circular-hole-array sample. Lengths of the scale bars correspond to 1  $\mu\text{m}$  [19].

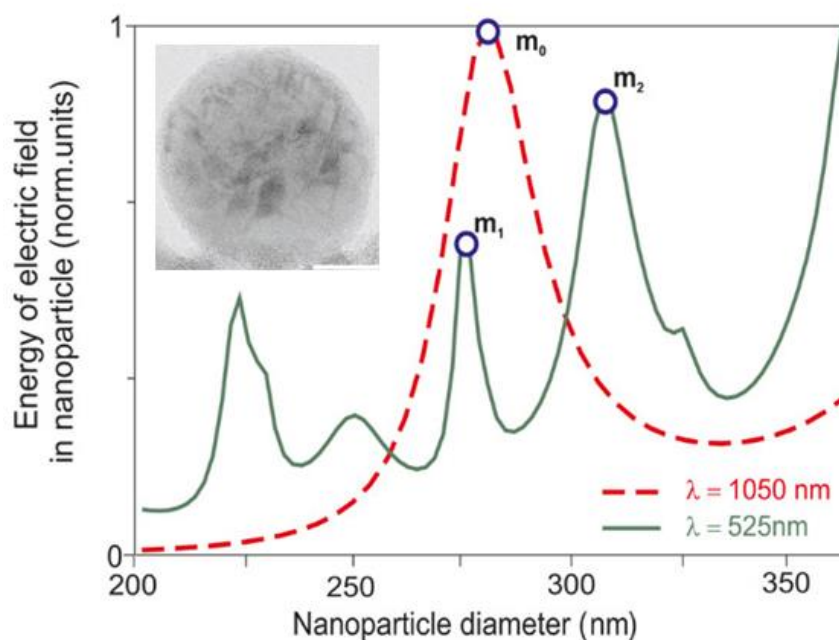
## 1.4 Second harmonic generation in metamaterials

### 1.4.1 Local field enhancement by resonant modes of metamaterials

The surface SHG effects in subwavelength scale structures can be improved by enhancing local fields [58]. Metamaterials can be designed to be resonant at the pump wavelength. Compared to off-resonant response, a metamaterial with quality factor  $Q$ , will display an increase in second harmonic generation efficiency by  $Q^2$ , when driven at resonance. Structured optical materials can support resonant modes which are related directly to how the material was structured [59-61] and it is possible to achieve multiple resonances in one structured medium [58, 62]. If the local fields at both fundamental frequency and second harmonic frequency are enhanced by resonant modes in a structured medium, the efficiency of second harmonic generation effects will increase substantially [62].

**Figure 1.7** shows the simulated multi-resonant dependence of the electric field energy accumulated inside silicon nanoparticles as a function of their diameter under irradiation by a plane electromagnetic wave at a pump wavelength of 1050 nm and a SH wavelength of 525 nm. Three modes are labelled as  $m_0$ ,  $m_1$  and  $m_2$ . The spectral and spatial overlap of these modes supported

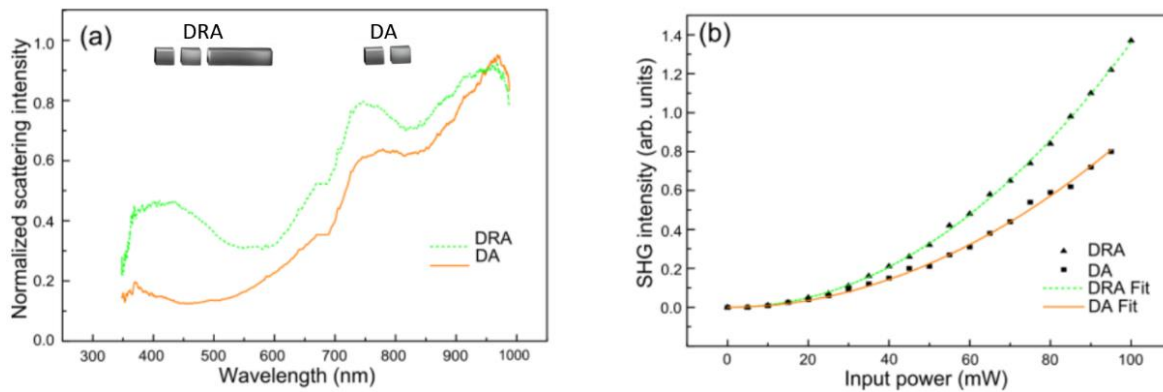
by the nanoparticles can enhance local fields at both fundamental and second harmonic wavelengths, 1050 nm and 525 nm respectively.



**Figure 1.7 Modelled energy of the electric field trapped inside a Si nanoparticle**

Numerically modelled energy of the electric field trapped inside a Si nanoparticle under illumination at pump (red dashed curve) and SH (green solid curve) wavelengths. Three resonances are labelled as  $m_0, m_1, m_2$ , respectively [62]. The insert shows a Si nanoparticle.

Enhanced second harmonic generation has been observed from a double resonant plasmonic antenna, see **Figure 1.8**. The authors compared the second harmonic generation from a standard dipole antenna of a resonance at about 800 nm wavelength to the SHG from a double resonant antenna with resonances at both the fundamental wavelength (800 nm) and the second harmonic wavelength (400 nm). Finally, they found that the double resonant antenna produced a SH intensity almost twice that of the dipole antenna (see **Figure 1.8b**) due to the local field enhancement at both fundamental and second harmonic wavelengths.



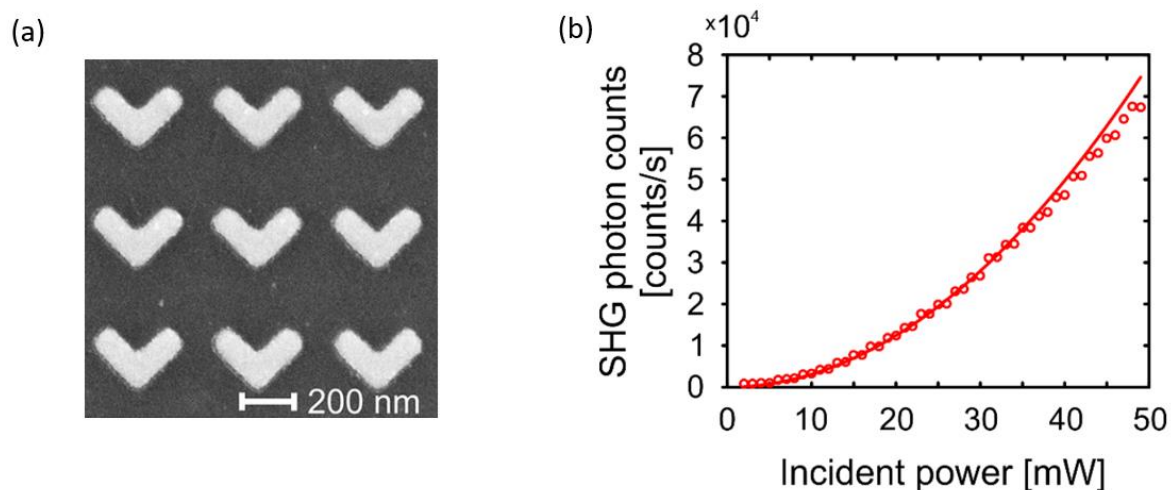
**Figure 1.8 Enhanced SHG from double resonant plasmonic antenna**

(a) Scattering spectra of the standard dipole antenna (DA) and the double resonant antenna (DRA). The double structure shows a clear enhancement of the scattering around  $\lambda = 400\text{nm}$ , both structures are made of aluminium. (b) A comparison of the experimental SHG signal with a quadratic fit, for a DA and a DRA shows the enhanced SHG from the DRA [58].

#### 1.4.2 Second harmonic generation by metallic and dielectric nanostructures

Both metallic and dielectric nanostructures have been exploited to demonstrate enhanced SHG [62-65]. Noble metallic nanostructures support collective oscillations of conduction electrons, known as surface plasmons, which strongly affect their optical response. When plasmonic nanostructures are illuminated on resonance, the incident electromagnetic field is significantly enhanced on their surfaces, which can enable strong nonlinear optical effects at relatively low excitation powers.



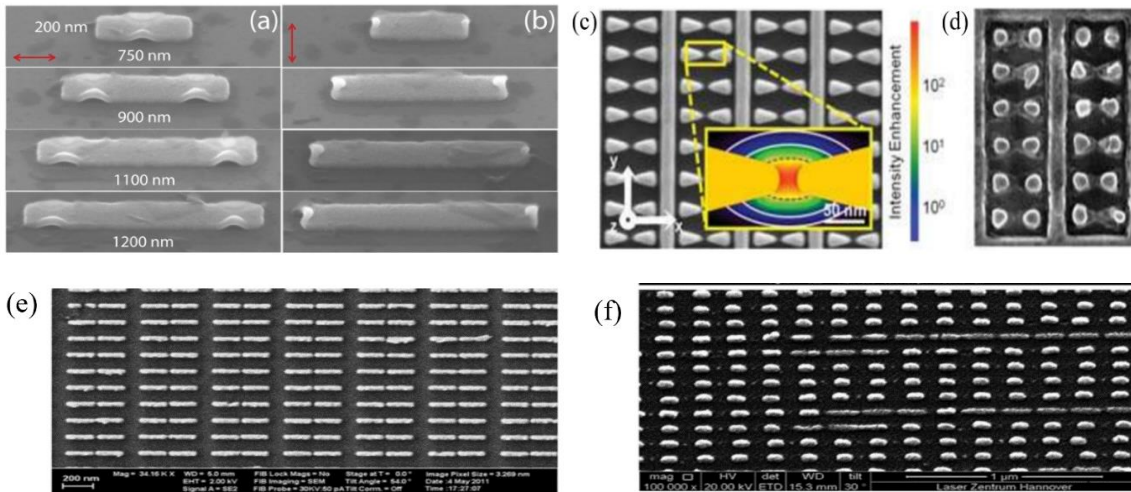


**Figure 1.9** Second harmonic generation by a metamaterial with D1 symmetry

(a) SEM image of the metamaterial. (b) Measured power dependence of the detected SHG signal. The dependence was close to quadratic for input powers below 40 mW, as is seen by the good agreement between the measured signal (open circles) and the fit (solid line) [49].

Optical second harmonic generation from metasurfaces, where noncentrosymmetric V-shaped gold nanoparticles are arranged in regular array configurations, has been observed [49], see **Figure 1.9**. The V-shaped meta-atom belongs to the D1 symmetry group, which has 3 independent symmetry-allowed  $\chi^{(2)}$  components, making it possible to get second harmonic generation at normal incidence. The wavelength of generated second harmonic signal can be tuned from 500 nm to 650 nm, corresponding to a pump wavelength range from 1000 nm to 1300 nm. The highest SHG was achieved at about 575 nm. However, sample damages occurred when the excitation average power is above 40mW.

Although using higher peak intensities can achieve considerably higher conversion efficiencies, the conversion efficiency is mostly restricted by the material damage via heating. Metallic structures suffer from low damage thresholds. If high pump power is used, heat will accumulate in the these structures, which may damage the sample [66-68], for example, **Figure 1.10** shows three examples of laser induced deformation in metallic nanostructures. Clearly, melting leads to significant changes in the sizes of these nanostructures as well as the gaps between them, which may result in a reduced electric field enhancement.

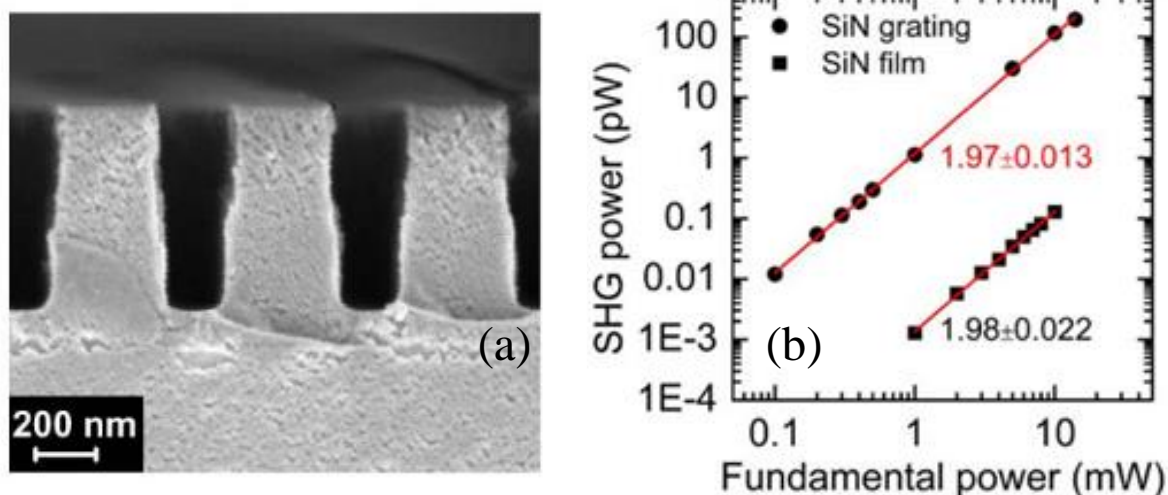


**Figure 1.10 SEM images of damaged metallic nanostructures**

(a)-(b) Ni nanostripes with plasmon-induced permanent deformations. The nanostripe is excited by single light pulses with polarization oriented (a) along the nanostructures and (b) perpendicular to the nanostructures [66]. (c) Au bowtie array fabricated by the FIB process and (d) bowties damaged by laser pulse [67]. (e)- (f) Au rod-type optical antennae before (e) and after (f) illumination with the laser pulses [68].

Compared to metallic nanostructures, dielectric nanostructures have the advantage of low dissipative losses and high damage threshold. Therefore, the latter can avoid the problems of the former. Furthermore, dielectric photonic structures can exhibit narrow resonances due to the high reflective index of some low-loss dielectrics. Among dielectric materials, silicon nitride and silicon are excellent candidates for all-dielectric devices, since they are highly compatible with the optical fibre and semiconductor fabrication ecosystem. Furthermore, thin layers of silicon nitride and silicon can be transparent for both fundamental and SHG lights. For example, when the fundamental light is at 1550 nm wavelength (see **Figure 6.3**).

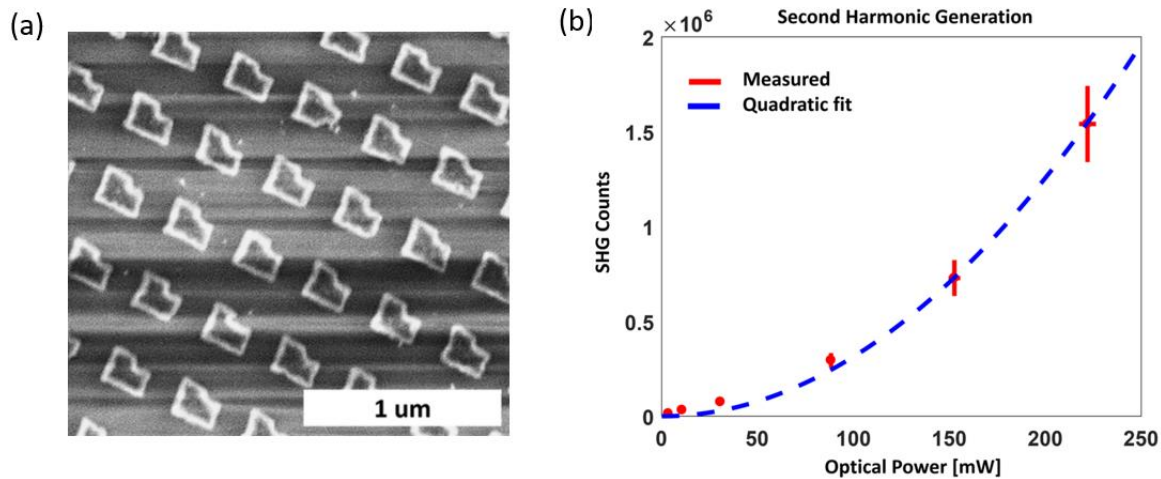
Efficient second-harmonic generation in silicon nitride resonant waveguide gratings has been reported [69]. The waveguide grating was built by etching a layer of silicon nitride (SiN) film. **Figure 1.11(a)** shows a SEM image of the SiN resonant waveguide grating. The enhanced SHG signal from the silicon nitride resonant waveguide grating is three orders of magnitude higher than that from a flat SiN film, which is attributed to the enhanced local fields in the nanostructure. However, this structure (D2 symmetry) requires an oblique incident pump beam for SHG.



**Figure 1.11 SHG by a SiN resonant waveguide grating**

(a) SEM image of the SiN resonant waveguide grating. (b) Measured SH power as a function of fundamental laser power on a log-log scale. The squares represent SH power for the reference film and the circles for the resonant waveguide gratings. The solid lines are their fits [69].

Second harmonic generation from amorphous silicon ( $\alpha$ -Si) metasurfaces consisting of L-shaped (C1 symmetry) meta-atoms has been observed as well [25], see **Figure 1.12**. The structure consists of identical L-shaped meta-atoms with a period of 390 nm in a  $200 \mu\text{m} \times 200 \mu\text{m}$  arrays. An excellent fit of the detected SHG signal at 420 nm wavelength to the square of the power of an excitation laser at 840 nm wavelength was observed. The second harmonic generation is confirmed to originate from the patterned C1 symmetry structure, rather than the materials, as the authors used centrosymmetric amorphous silicon as working medium and normally incident pumping.



**Figure 1.12 SHG by metamaterials consisting of C1 symmetry meta-atoms**

(a) SEM micrograph of the fabricated L-shaped  $\alpha$ -Si meta-atoms. (b) SHG obtained from the metasurface as a function of illumination intensity. An excellent fit of the detected SHG signal to the square of the illumination power was observed [25].

There are no universal best materials or best structures for SHG metamaterials. One should design SHG metamaterials according to the needs. My goal is to develop a nonlinear metamaterial with high second-order nonlinearity that can be integrated with photonic devices. Therefore, Silicon is chosen because it has a relatively high refractive index and low loss at the telecommunication wavelength bands, which enables high quality factor resonances. Also, compared with metallic structures such as gold and silver, silicon has a higher damage threshold, and can therefore withstand a higher pump laser intensity. Moreover, silicon is highly compatible with the optical fibre and semiconductor fabrication ecosystem, which enables developing integrated nonlinear photonic devices.

Then, another question is how the nanostructures should be chosen. To answer this question, theoretical analysis is needed.

## 1.5 Theoretical models of nonlinearity of films

The quadratic surface nonlinearity has been discovered in 1960s [37, 70], and has remained an active area of research ever since. A lot of attention has been paid to nonlinear response at the surfaces of unstructured metals and dielectrics [71-74], surfaces with adsorbed or admixed molecules [75-79], and, more recently, surfaces of nanoparticles and metamaterials [19, 20, 25, 27, 28, 80-93]. The advance of nanofabrication to smaller and smaller scales provides an opportunity to engineer the nonlinear properties of particles and (meta)surfaces on the nanoscale. Such engineering depends on understanding the dependence of nonlinear optical properties on the

arrangement of atoms. Full ab-initio quantum treatments of surface nonlinearity have been demonstrated, but only for specific materials and under specific conditions [94-100], whilst experimental measurements, of surface nonlinearity, require pristine surfaces and strict control over the bulk effects [35, 71, 80, 82, 88]. Sophisticated classical/quantum test models have been previously developed for metals [34, 86], ‘dipolium’ dielectrics [100, 101], and few dielectric particles of quite specific shapes [81]. Second harmonic generation strongly depends on geometry, i.e. the shape of particles or the unit cell of periodic structures. Symmetry-based selection rules [84, 102] identify cases where second harmonic generation is forbidden, but cannot predict its magnitude where it is allowed. The resulting optimization challenge has led to a substantial research effort, studying second harmonic generation by nanostructures of various shapes [21, 22, 80, 86, 92, 103, 104].

A model that applies macroscopic Maxwell equations to the resonant interaction of electromagnetic radiation and dielectric crystals consisting of molecules coupled via retarded dipole fields is investigated [105], but only studies linear macroscopic properties of dielectrics. Similar approaches have been employed to study nonlinear properties of dielectrics [106], harmonic generation by metallic structures [107] and anharmonic oscillators [108, 109], and for treating surface nonlinearity of uniform planar surfaces [98-101, 110].

A range of models of sum frequency generation has been reported, e.g. for harmonic oscillators [111] and liquid interfaces [75, 112, 113]. Nonlinear oscillator models predicting enhanced nonlinear response of metacrystals have been reported [114, 115] and applied to split ring resonator magnetic media.

In this thesis, my focus is on highly structured materials and my model is applicable to planar dielectric nanostructures of any shape. The results will be used to instruct the design of metamaterials.

## 1.6 Outline of the thesis

This thesis is focus on studying structuring induced nonlinearity, both theoretically and experimentally. The layout of the thesis is as follows:

**Chapter 2** introduces a widely-applicable Coulomb-coupled-oscillator model for predicting optical nonlinearity in 2D nanostructures and the model is applied in **Chapters 3-5**. **Chapter 3** investigates the second-order nonlinearity of structured dielectric film consisting of a centrosymmetric dielectric material. **Chapter 4** applies the model to harmonic and sum frequency generation in 2D nanostructures. **Chapter 5** describes defect induced harmonic generation in 2D nanoparticles. Then

## Chapter 1

I moved from the theory studies to real metamaterials. **Chapter 6** shows the design and fabrication process of a fibre-integrated all-dielectric metasurface. **Chapter 7** presents the experimental demonstration of second harmonic generation from the fibre-integrated all-dielectric metasurface. Finally, in **Chapter 8** the main conclusions of this work are derived, and the future outlook, prospect and ideas for this project are also discussed.

## Chapter 2 Microscopic Coulomb-coupled-oscillator model of optical nonlinearity

### 2.1 Introduction

Optical nonlinearities of matter are often associated with the charge oscillation of individual atoms. Indeed, whilst some electromagnetic media support material-specific even-order nonlinearity, charges in all materials, to a good approximation, interact via the Coulomb force. In this chapter, I develop a Coulomb-coupled-oscillator model of optical nonlinearity and demonstrate that in the confined geometry of a two-dimensional nanoparticle the collective nonlinear response of the atomic array can arise from the Coulomb interactions of the optical electrons, even if the individual atoms exhibit no nonlinearity.

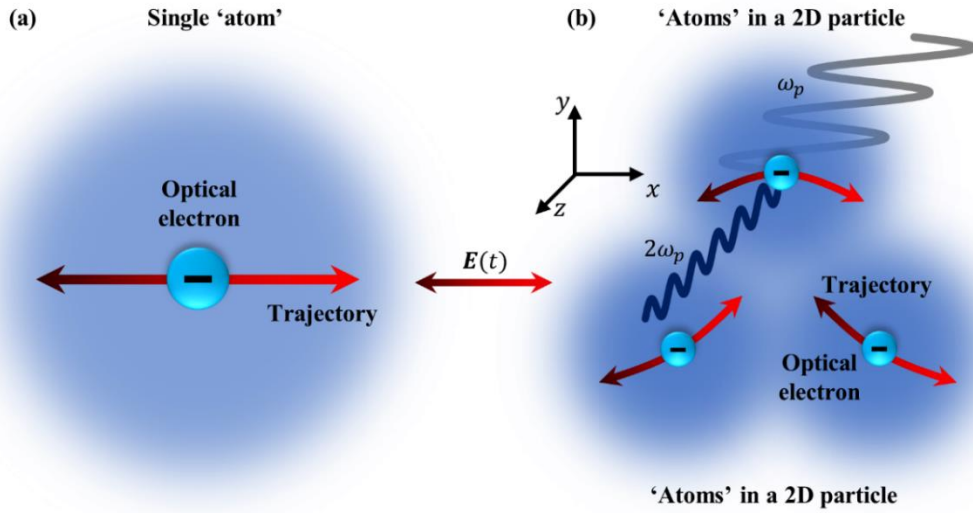
Second harmonic generation (SHG) due to Coulomb interactions has been observed experimentally in dimers of metallic nanoparticles of deeply sub-wavelength size [116] and a similar nonlinearity arising from electrostatic interactions has been considered in the context of nonlinear plasmonic metamaterials [117]. Similar approaches have been previously employed to study linear [105] and nonlinear properties of dielectrics [106], harmonic generation by metallic structures [107] and anharmonic oscillators [108, 109], and for treating surface nonlinearity of uniform planar surfaces [98-101, 110]. A range of models of sum frequency generation has been reported, e.g. for harmonic oscillators [111] and liquid interfaces [75, 112, 113]. Here our focus is on highly structured materials and our model is applicable to planar dielectric nanostructures of any shape. Therefore, it complements existing models that describe harmonic or sum frequency generation in specific materials and/or shapes [22, 34, 81, 86, 94, 118], and symmetry-based selection rules [84, 102]. Such models tend to identify cases where second-order non-linear processes are forbidden. Here I will show approach that enables one to go beyond the allowed/forbidden dichotomy.

The detailed description of the model is discussed in **Section 2.2** and then two methods of getting charges' displacements from the model - Taylor expansion in **Section 2.3** and Fourier transformation in **Section 2.4** - are introduced. Finally, the parameters used in the model are given in **Section 2.5**.

### 2.2 Microscopic Coulomb-coupled-oscillator model

In order to predict the nonlinearity of a structured dielectric film, such as a metamaterial or a two-dimensional (2D) nanoparticle, we consider  $N$  atoms that are confined to the  $xy$ -plane and

excitation by a plane wave propagating along  $z$  (see **Figure 2.1a**). Each atom is described as a classical Lorentz oscillator [119] with a negatively charged optical electron bound to a positively charged stationary nucleus with coordinate  $R_k$ . As is standard Lorentz model approximation, the electron and the nucleus are elastically bound which gives rise to a linear restoring force and the electromagnetic response of the single atom is strictly linear (This will be discussed in more detail in **Section 4.5**).



**Figure 2.1 Model for the optical response of interacting atoms in a dielectric nanoparticle**

(a) The atoms are modelled as damped harmonic oscillators consisting of an optical electron constrained to move in the  $xy$ -plane and a positively charged stationary nucleus at the atom's centre. (b) The nonlinear optical response of a nanoparticle originates from the Coulomb interactions between optical electrons and other atoms. These interactions cause sum/harmonic frequency generation by perturbing the harmonic electron oscillation driven by incident light field  $E(t)$ . In particular, Coulomb forces at boundaries become direction-dependent and electron trajectories become curved.

The interaction of the electron with its own core is modelled as lossy harmonic oscillator:

$$\ddot{r} + \gamma \dot{r} + \omega_0^2 r = \frac{q}{m} E \quad (2.1)$$

Here  $r$  is the displacement of the electron. With two degrees of freedom (along the in-plane  $x$ - and  $y$ -axis), the equation of motion can be written as:

$$\begin{pmatrix} \ddot{x} \\ \ddot{y} \end{pmatrix} + \gamma \begin{pmatrix} \dot{x} \\ \dot{y} \end{pmatrix} + \omega_0^2 \begin{pmatrix} x \\ y \end{pmatrix} = \frac{q}{m} \begin{pmatrix} E^x(t) \\ E^y(t) \end{pmatrix} \quad (2.2)$$

Here,  $\omega_0$  is the resonance angular frequency of an isolated atom and  $\gamma$  is the damping frequency.  $q$  is the charge of the electron and  $m$  is the mass of the electron.  $x$  and  $y$  are the corresponding displacements of the electron relative to its own core. In the equilibrium without driving field,  $x$  and



y equal to 0, irrespective of core position. This approach captures sufficient dynamics of conventional atoms and the finite loss allows to account for phenomena such as radiation resistance of the electrons [52]. From **Equation 2.1**, it is clear the electromagnetic response of a single atom is strictly linear, only oscillating along the driving field's polarization direction.

However, when there is more than one atom, Coulomb interactions between electrons as well as electrons and nuclei occur. The nonlinear response arises exclusively due to inter-atomic Coulomb interactions. The  $\propto 1/R^2$  dependence of the Coulomb force, where R is the inter-charge separation, gives rise a nonlinear response of optical electrons in collections of coupled atoms, which is illustrated by curved optical electron trajectories in **Figure 2.1(b)**.

For a system that contains  $N$  electrons, the Coulomb interaction  $F_k^{(x,y)}$  in the  $N$  electron system is the sum of the Coulomb interactions between the  $k^{th}$  electron and the other  $(N-1)$  electrons or nuclei. Therefore,  $x_k$ , the displacement of the  $k^{th}$  electron along the  $x$ -axis, will be given by:

$$m\ddot{x}_k + m\gamma\dot{x}_k + m\omega_0^2 x_k = qE^x(t) + F_k^{(x)} \quad (2.3)$$

and the Coulomb interaction  $F_k^{(x)}$  for the  $k^{th}$  electron along the  $x$ -axis is

$$F_k^{(x)} = \frac{q^2}{4\pi\epsilon_0} \sum_{i \neq k}^N \frac{(R_{xk} + x_k) - (R_{xi} + x_i)}{[(R_{xk} + x_k) - (R_{xi} + x_i)]^2 + [(R_{yk} + y_k) - (R_{yi} + y_i)]^2]^{\frac{3}{2}}} - \frac{(R_{xk} + x_k) - R_{xi}}{[(R_{xk} + x_k) - R_{xi}]^2 + [(R_{yk} + y_k) - R_{yi}]^2]^{\frac{3}{2}}} \quad (2.4)$$

Here,  $R_x, R_y$  are the coordinates of the nuclei and  $x, y$  are the electron's displacement relative to its nucleus, meaning  $k^{th}$  electron's coordinates are  $[R_x + x_k, R_y + y_k]$ .

By solving the coupled differential equations, we can get the displacement of each electron in the system. Since the electric dipole moment  $\mathbf{d}$  is proportional to the displacements of the electrons, the electric dipole moment distribution in the structure is acquired. For a structure containing  $N$  electrons and with a size small compared to the operating wavelength, the  $N$  electrons will behave as one big atom with a 'giant' dipole moment [105], which will be referred to as the total dipole moment of the particle  $\mathbf{P} = \sum_k \mathbf{d}_k$ . Other multipoles and their radiation can also be calculated, which will be discussed in **Chapter 4**.

### 2.3 Taylor expansion

There are two ways of solving the coupled equations of motion in my work. Now I will introduce the first one – Taylor expansion.

Solving coupled differential equations is nontrivial when there is a large number of atoms involved, which takes a long time and may induce numerical errors. To simplify the process and increase the speed and stability of numerical modelling, we did a Taylor expansion up to the second order for the Coulomb interaction and use the resulting perturbation equation of motion to calculate the displacement of each electron. In the first stage, the linear response of N coupled atoms is found. This linear response is then used, in the second stage, as a source for determining the nonlinear response.

The x-direction displacement of the k<sup>th</sup> electron  $x_k$  is expanded to the second order, where  $x_{kDC}$ ,  $x_{k1}$ , and  $x_{k2}$  indicate the zero, first and second order terms of the expansion of  $x_k$ , respectively:

$$x_k = x_{k1} + x_{k2} + x_{kDC} \quad (2.5)$$

$$x_{k1} = 2 \operatorname{Re}(\hat{x}_{k1} e^{i1\omega t}) = \hat{x}_{k1} e^{i1\omega t} + \text{c. c.} \quad (2.6)$$

$$x_{k2} = 2 \operatorname{Re}(\hat{x}_{k2} e^{i2\omega t}) = \hat{x}_{k2} e^{i2\omega t} + \text{c. c.} \quad (2.7)$$

The Taylor expansion for the Coulomb interaction  $F_k^{(x)}$  to the second order is:

$$\begin{aligned} F_k^{(x)} = & \sum_{i \neq k} x_i \partial_{x_i} F_k^{(x)} + \sum_{i \neq k} y_i \partial_{y_i} F_k^{(x)} + \frac{1}{2} \sum_{i \neq k} x_i^2 \partial_{x_i x_i} F_k^{(x)} + \frac{1}{2} \sum_{i \neq k} y_i^2 \partial_{y_i y_i} F_k^{(x)} \\ & + \sum_{i \neq k} x_k y_i \partial_{x_k y_i} F_k^{(x)} \\ & + \sum_{i \neq k} x_i y_k \partial_{x_i y_k} F_k^{(x)} + \sum_{i \neq k} x_k x_i \partial_{x_k x_i} F_k^{(x)} + \sum_{i \neq k} y_k y_i \partial_{y_k y_i} F_k^{(x)} \\ & + \sum_{i \neq k} x_i y_i \partial_{x_i y_i} F_k^{(x)} \end{aligned} \quad (2.8)$$

$F_k^{(y)}$  and  $y_k$  can be expanded in the same way. Then we put **Equation (2.5)** and **(2.8)** into **(2.3)**:

$$\begin{aligned} m(\ddot{x}_{k1} + \ddot{x}_{k2} + \ddot{x}_{kDC}) + m\gamma(\dot{x}_{k1} + \dot{x}_{k2} + \dot{x}_{kDC}) + m\omega_0^2(x_{k1} + x_{k2} + x_{kDC}) \\ = qE^x(t) + \sum_{i \neq k} (x_{i1} + x_{i2} + x_{iDC}) \partial_{x_i} F_k^{(x)} \\ + \sum_{i \neq k} (y_{i1} + y_{i2} + y_{iDC}) \partial_{y_i} F_k^{(x)} + \frac{1}{2} \sum_{i \neq k} (x_{i1} + x_{i2} + x_{iDC})^2 \partial_{x_i x_i} F_k^{(x)} \\ + \frac{1}{2} \sum_{i \neq k} (y_{i1} + y_{i2} + y_{iDC})^2 \partial_{y_i y_i} F_k^{(x)} \\ + \sum_{i \neq k} (x_{k1} + x_{k2} + x_{kDC})(y_{i1} + y_{i2} + y_{iDC}) \partial_{x_k y_i} F_k^{(x)} \\ + \sum_{i \neq k} (x_{i1} + x_{i2} + x_{iDC})(y_{k1} + y_{k2} + y_{kDC}) \partial_{x_i y_k} F_k^{(x)} \\ + \sum_{i \neq k} (x_{k1} + x_{k2} + x_{kDC})(x_{i1} + x_{i2} + x_{iDC}) \partial_{x_k x_i} F_k^{(x)} \\ + \sum_{i \neq k} (y_{k1} + y_{k2} + y_{kDC})(y_{i1} + y_{i2} + y_{iDC}) \partial_{y_k y_i} F_k^{(x)} \\ + \sum_{i \neq k} (x_{i1} + x_{i2} + x_{iDC})(y_{i1} + y_{i2} + y_{iDC}) \partial_{x_i y_i} F_k^{(x)} \end{aligned} \quad (2.9)$$

We determine the 1<sup>st</sup> and 2<sup>nd</sup> order equations of motion by inserting **Equation (2.6)** and **(2.7)** into **(2.9)**. Considering 1<sup>st</sup> order terms that oscillate at frequency  $\omega$ , the 1<sup>st</sup> order equation of motion is

$$\begin{aligned} & (-\omega^2 + i\gamma\omega + \omega_0^2)m\hat{x}_{k1}e^{i\omega t} + \text{c. c.} \\ & = \left[ q\hat{E}_x + \sum_{i \neq k} \hat{x}_{i1} \partial_{x_i} F_k^{(x)} + \sum_{i \neq k} \hat{y}_{i1} \partial_{y_i} F_k^{(x)} \right] e^{i\omega t} + \text{c. c.} \end{aligned} \quad (2.10)$$

which simplifies to

$$(-\omega^2 + i\gamma\omega + \omega_0^2)m\hat{x}_{k1} = q\hat{E}_x + \sum_{i \neq k} \hat{x}_{i1} \partial_{x_i} F_k^{(x)} + \sum_{i \neq k} \hat{y}_{i1} \partial_{y_i} F_k^{(x)} \quad (2.11)$$

Electron motion at frequency  $2\omega$  is a small perturbation of electron motion at frequency  $\omega$ . Considering leading terms that oscillate at frequency  $2\omega$ , the 2<sup>nd</sup> order perturbation motion equation is

$$\begin{aligned} & (-4\omega^2 + i2\gamma\omega + \omega_0^2)m\hat{x}_{k2}e^{i2\omega t} + \text{c. c.} \\ & = \left[ \sum_{i \neq k} \hat{x}_{i2} \partial_{x_i} F_k^{(x)} + \sum_{i \neq k} \hat{y}_{i2} \partial_{y_i} F_k^{(x)} + \frac{1}{2} \sum_{i \neq k} (\hat{x}_{i1})^2 \partial_{x_i x_i} F_k^{(x)} \right. \\ & + \frac{1}{2} \sum_{i \neq k} (\hat{y}_{i1})^2 \partial_{y_i y_i} F_k^{(x)} + \sum_{i \neq k} \hat{x}_{k1} \hat{y}_{i1} \partial_{x_k y_i} F_k^{(x)} \\ & + \sum_{i \neq k} \hat{x}_{i1} \hat{y}_{k1} \partial_{x_i y_k} F_k^{(x)} + \sum_{i \neq k} \hat{x}_{k1} \hat{x}_{i1} \partial_{x_k x_i} F_k^{(x)} + \sum_{i \neq k} \hat{y}_{k1} \hat{y}_{i1} \partial_{y_k y_i} F_k^{(x)} \\ & \left. + \sum_{i \neq k} \hat{x}_{i1} \hat{y}_{i1} \partial_{x_i y_i} F_k^{(x)} \right] e^{i2\omega t} + \text{c. c.} \end{aligned} \quad (2.12)$$

which simplifies to

$$\begin{aligned} & (-4\omega^2 + i2\gamma\omega + \omega_0^2)m\hat{x}_{k2} \\ & = \sum_{i \neq k} \hat{x}_{i2} \partial_{x_i} F_k^{(x)} + \sum_{i \neq k} \hat{y}_{i2} \partial_{y_i} F_k^{(x)} + \frac{1}{2} \sum_{i \neq k} (\hat{x}_{i1})^2 \partial_{x_i x_i} F_k^{(x)} \\ & + \frac{1}{2} \sum_{i \neq k} (\hat{y}_{i1})^2 \partial_{y_i y_i} F_k^{(x)} + \sum_{i \neq k} \hat{x}_{k1} \hat{y}_{i1} \partial_{x_k y_i} F_k^{(x)} \\ & + \sum_{i \neq k} \hat{x}_{i1} \hat{y}_{k1} \partial_{x_i y_k} F_k^{(x)} + \sum_{i \neq k} \hat{x}_{k1} \hat{x}_{i1} \partial_{x_k x_i} F_k^{(x)} + \sum_{i \neq k} \hat{y}_{k1} \hat{y}_{i1} \partial_{y_k y_i} F_k^{(x)} \\ & + \sum_{i \neq k} \hat{x}_{i1} \hat{y}_{i1} \partial_{x_i y_i} F_k^{(x)} \end{aligned} \quad (2.13)$$

The y-component can be treated in the same way.

The linear electric dipole of the k<sup>th</sup> electron will be:

$$\mathbf{d}_k^{(1)} = q \begin{pmatrix} x_{k1} \\ y_{k1} \end{pmatrix} \quad (2.14)$$

Its second-order nonlinear electric dipole will be:

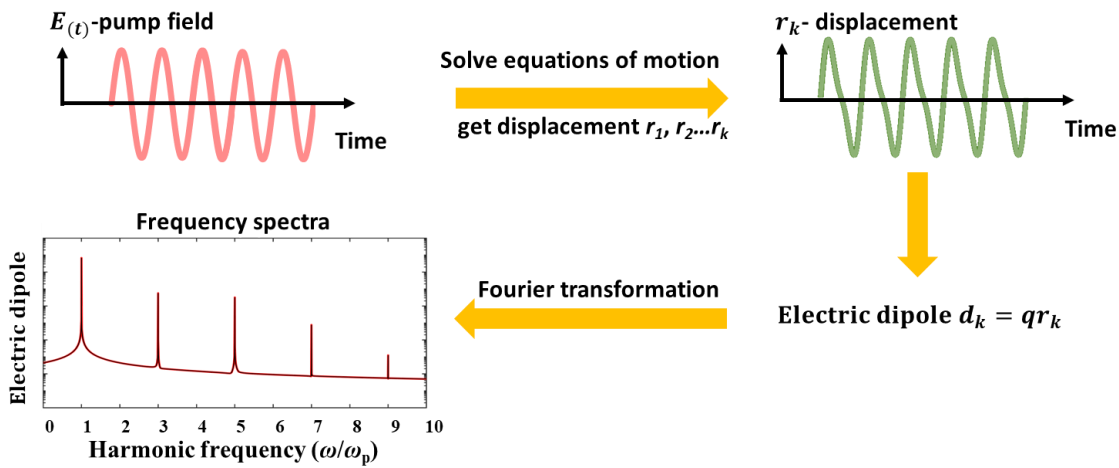
$$\mathbf{d}_k^{(2)} = q \begin{pmatrix} x_{k2} \\ y_{k2} \end{pmatrix} \quad (2.15)$$

Then, the dipole moment of every atom in a structure can be calculated, as a result, the effect of the structures' shape can be known directly. By adding up the dipoles of each electron, the total

linear dipole ( $\mathbf{P}^{(1)}$ ) and total SH dipole ( $\mathbf{P}^{(2)}$ ) of the whole structure can be calculated. The results of **Chapter 3** are calculated through this method.

### 2.4 Fourier transformation

Although Taylor expansion can increase the speed and stability of numerical modelling, it is not practical to simulate sum frequency generation, which involves excitation fields at several frequencies. Also, for modelling harmonic generation higher than second order, the Taylor expansion of the  $F_k$  will become rather complicated. Therefore, Fourier transformation - another method of solving the Coulomb-coupled-oscillator model for 2D particles - can be used, when modelling higher harmonic and sum frequency generation.



**Figure 2.2 Schematic of calculating electric dipole via Fourier transformation**

An electric field  $E(t)$  is incident and excites charge displacement of the  $k^{\text{th}}$  electron  $r_k$ . Then the electric dipole moment  $d_k$  in time domain is calculated and transferred into the frequency domain via Fourier transformation. Finally, all the frequency components are displayed in the frequency spectra of the electric dipole.

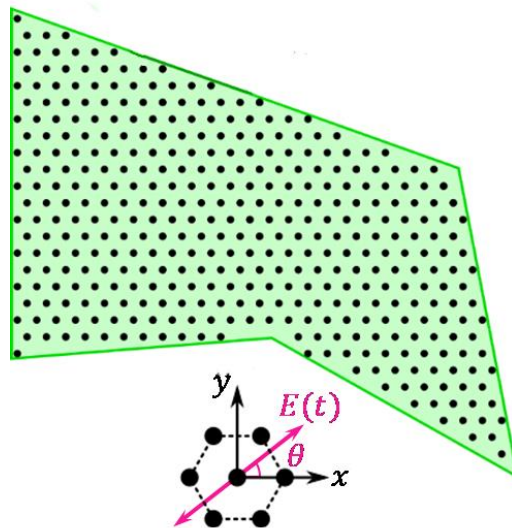
The process of getting electric dipole’s frequency spectra is shown in **Figure 2.2**. At the first stage, by solving the coupled equations of motion (**Equation 2.3**) of all optical electrons within 2D nanoparticles numerically, we calculate the displacement of each optical electron in the time domain. We solve the coupled system of differential equations starting without optical electron displacement and allowing transitional effects to pass before analysing the oscillation of all electrons over 1000 periods of the driving field.

Then, the electric dipole is calculated. The electric dipole moment is proportional to the displacement of electrons. Therefore, a displacement of the  $k^{\text{th}}$  electron relative to its nucleus,  $r_k$ , results in an electric dipole due to the  $k^{\text{th}}$  atom of  $\mathbf{d}_k = q\mathbf{r}_k$ , and the total electric dipole of the particle

is the sum over all atoms,  $\mathbf{P} = \sum_k \mathbf{d}_k$ . This gives the electric dipole moment  $\mathbf{d}(t)$  of each atom and the total electric dipole moment  $\mathbf{P}(t)$  of the nanostructure in the time domain. The total electric dipole moment is separated into linear and nonlinear components,  $\mathbf{P}^{(1)}$ ,  $\mathbf{P}^{(2)}$ ,  $\mathbf{P}^{(3)}$  ... , oscillating at the driving frequency  $\omega_p$  and its harmonics  $2\omega_p$ ,  $3\omega_p$  ... , by Fourier transformation. In the presented Fourier series, the peak values are the dipole amplitudes in Coulomb meters at harmonic and sum frequencies. For pumping of a 2D particle at normal incidence, as considered here, radiation emitted normal to the plane of the particle is determined by its total electric dipole moment alone.

## 2.5 Parameters

The two-dimensional particles we will study are collective atoms cut out of either a hexagonal lattice (see **Figure 2.3**) or a square lattice. The atomic spacing is chosen to be 0.5 nm in all cases.



**Figure 2.3** A particle cut from two-dimensional material of hexagonal lattice

Dots indicate atom positions. The fundamental incident wave  $E(t)$  is linearly polarized at angle  $\theta$  to the x-axis and enters the particle at normal incidence.

The resonance frequency of an isolated atom is  $\omega_0 = 9.4 \times 10^{15}$  rad/s, corresponding to a UV resonance at 200 nm wavelength, and the damping frequency is  $\gamma = 0.01 \omega_0$  to approximate a typical atomic response in dielectrics such as ITO, TiOx and SiN. The pump wavelength is chosen to be 1064 nm, a common choice for nonlinear optics that is far from the atomic resonance (angular pump frequency  $\omega_p = 0.19 \omega_0$ ). In modelling of sum frequency generation, we pump the particle at two frequencies,  $\omega_p$  and  $0.1\omega_p$ , simultaneously.

To excite second harmonic generation in **Chapter 3**, the amplitude of the driving electric field ( $E$ ) is chosen to be  $8.68 \times 10^7$  V/m, which corresponds to pump light of  $1 \text{ GW/cm}^2$  intensity.

## Chapter 2

In order to access a highly nonlinear regime in **Chapter 4**, the amplitude of the pumping electric field ( $E_0$ ) is set to  $8.68 \times 10^{10}$  V/m, corresponding to  $10^{15}$  W/cm<sup>2</sup> pump intensity. While this extreme level of intensity may not be feasible experimentally, it allows us to explore physical trends and higher-order optical nonlinearities in a regime where they are of sufficient magnitude to make numerical errors of differential equation solvers irrelevant. Basically, solving the equations of motion involves taking differences between very similar numbers. The Taylor expansion gets around this analytically, but is limited to SHG. The Fourier method has to live with it, i.e. it requires very high precision numbers or a regime where the effects are large. This regime of large nonlinear effects also provides numerical stability when solving the Coulomb-coupled-oscillator model using the Fourier method.

### 2.6 Summary

In this chapter, I developed a Coulomb-coupled-oscillator model of optical nonlinearity and demonstrated that in the confined geometry of a two-dimensional nanoparticle the collective nonlinear response of the atomic array can arise from the Coulomb interactions of the optical electrons, even if the individual atoms exhibit no nonlinearity.

Two methods of getting a structure's electric dipole moments from the model are introduced, one is Taylor expansion, and the other is Fourier transformation. When using the Taylor expansion method to solve the coupled equations of motion, the calculation time for a triangle particle containing 3691 atoms is only 32 seconds using **MATLAB R2018b** on a **Windows 10** computer with **Intel Core i5-6600 3.3 GHz CPU** and **32 GB RAM**, however, such results are limited to the second harmonic. In contrast, when using the Fourier transformation method, it takes at least 45 minutes to get the electron displacements of a triangle particle of 25 atoms, but in this case higher harmonics and sum frequencies are also calculated.

## Chapter 3 Model of second harmonic generation due to structuring of centrosymmetric films

### 3.1 Introduction

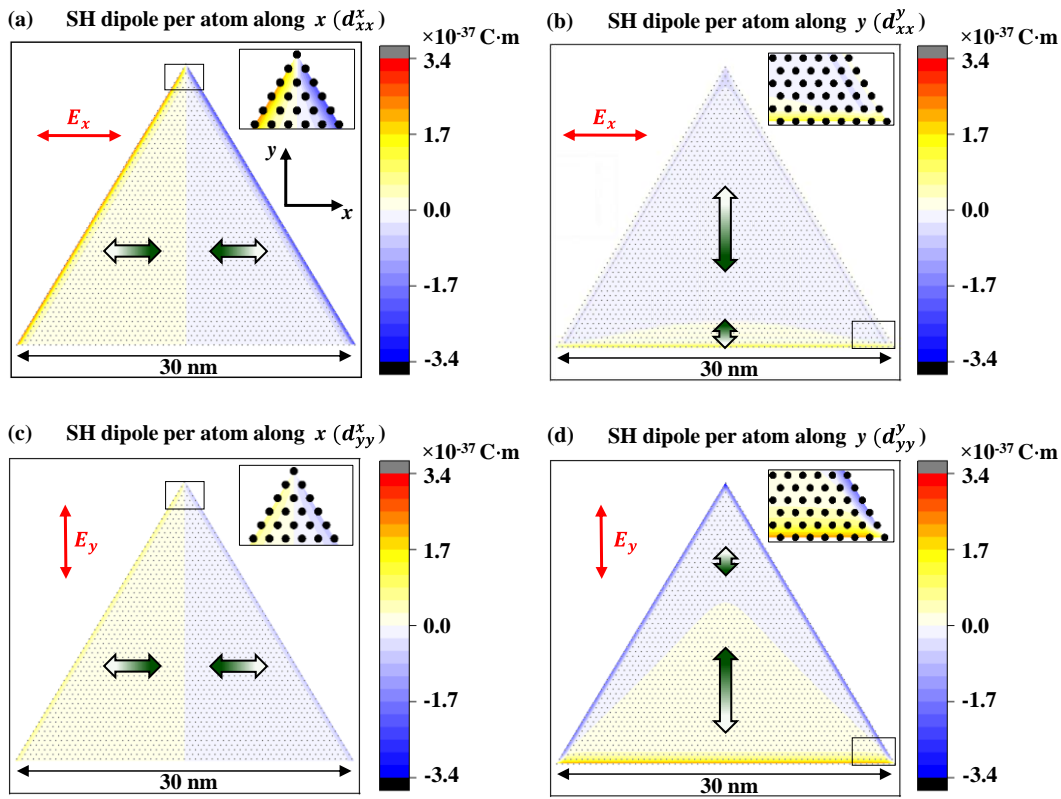
Optical second harmonic generation, which is important for optical signal processing, bio-imaging and spectroscopy, is usually suppressed in materials with inversion symmetry. Structuring of materials on the mesoscopic length scale has opened up an opportunity to engineer the nonlinear optical properties of any material. However, lack of efficient methods of predicting the nonlinear response of a broad range of mesoscopic structures has meant that progress largely depended on intuition.

In this Chapter, second-order nonlinearity of structured dielectric film consisting of a centrosymmetric dielectric material is studied, using the model built in **Chapter 2**. Here the nanostructure is considered as a collection of atoms formed by a hexagonal lattice. In order to increase the speed and stability of numerical modelling, the perturbative scheme described in **Section 2.3** is used. In the first stage, the linear response of  $N$  coupled atoms is found. This linear response is then used, in the second stage, as a source for determining the nonlinear response. The amplitude of the driving electric field ( $E$ ) is chosen to be  $8.68 \times 10^7$  V/m, which corresponds to pump light of  $1 \text{ GW/cm}^2$  intensity.

First, the second order electric dipole in triangle particles of  $D_3$  symmetry is studied in **Section 3.2** and then how the particle's symmetry affects its nonlinearity is discussed in **Section 3.3**. For a specific structure, how its nonlinearity depends on its size is learned in **Section 3.4**. Finally, a way of optimizing the structure's nonlinearity is presented in **Section 3.5**.

### 3.2 Second order nonlinear response in nanostructures of $D_3$ symmetry

Irrespective of the origin of nonlinear response, a total second-order nonlinear electric dipole of a 2D (two-dimensional) particle driven by in-plane optical fields is only allowed for structures with three-fold rotational symmetry, or no rotational symmetry [84, 102] (as shown in **Section 1.3**). Therefore, this section will focus on two-dimensional particles with three-fold overall rotational symmetry, the simplest case that permits second-order nonlinearity, represented by equilateral triangular arrangements of atoms cut out of a hexagonal lattice (see inserts in **Figure 3.1**).



**Figure 3.1. Second order nonlinear response in a triangular nanoparticle**

Colour maps show the  $\alpha$ -component of the atomic dipoles  $d_{\beta\beta}^\alpha$  at frequency  $2\omega$  when the particle is driven by light field  $E_\beta$  at frequency  $\omega$  polarized along the  $\beta$  direction, where  $\alpha, \beta = \{x, y\}$ . The inserts are magnified images of the sections framed by rectangles. Note the strong second order response at the edges.

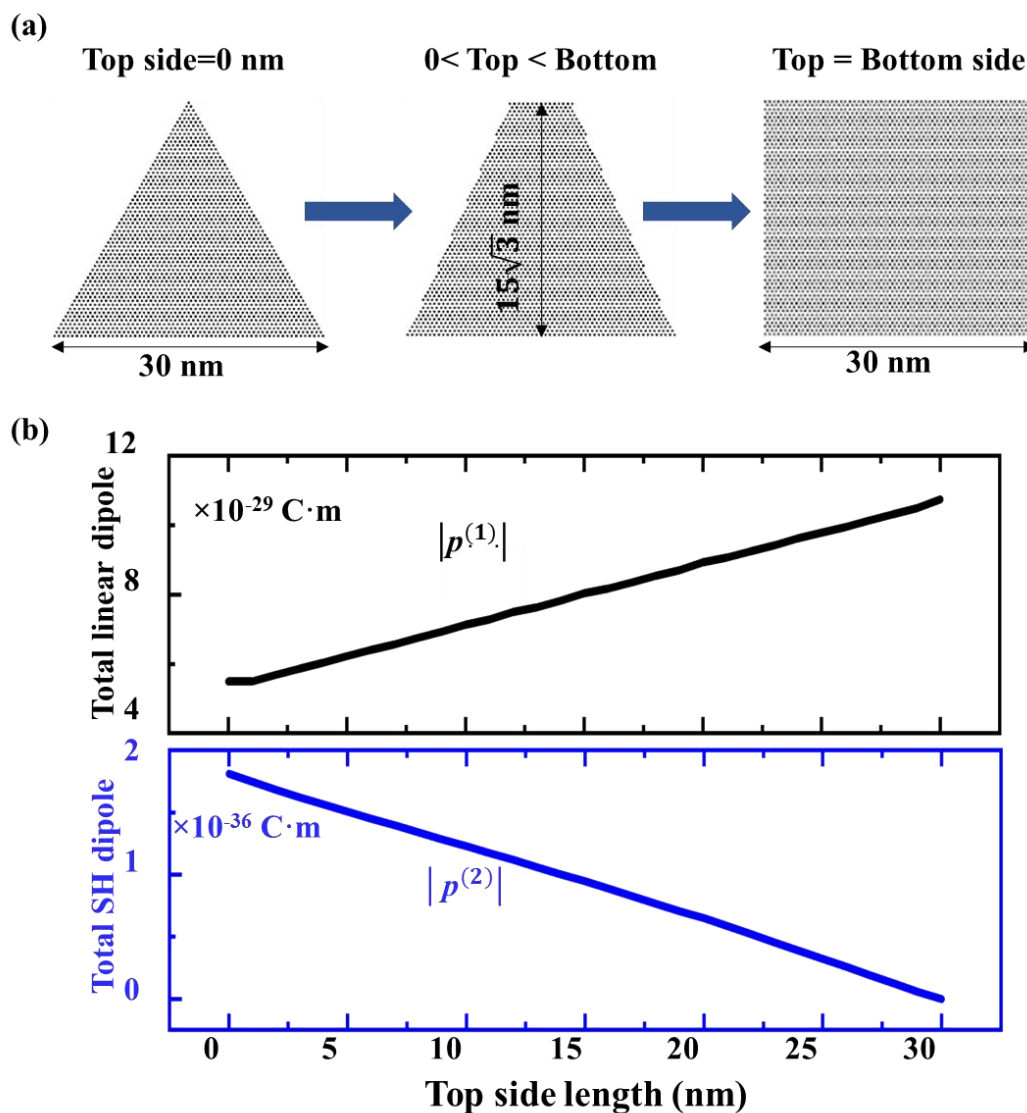
The notation  $d_{xx}^y$  is used to denote per-atom second-order nonlinear electric dipole along the  $y$ -axis induced due to driving field polarized along the  $x$ -axis. The other three components  $d_{xx}^x$ ,  $d_{yy}^y$  and  $d_{yy}^x$  follow in the same way. **Figure 3.1** shows the second-order nonlinear electric dipole induced in each atom of a triangular 2D particle, cut out of a hexagonal lattice of atoms.

Several important phenomena are readily observable: (1) the second order electric dipole is always weakest in the central region of the triangle – as one would expect for a centrosymmetric arrangement of atoms; (2) a second order nonlinear response at the edge seems to be induced in all cases with similar amplitude, but different phases of second harmonic response at different edges can yield vanishing (components of) total second harmonic response for a whole particle.  $x$ -polarized field (**Figure 3.1a**) as well as  $y$ -polarized field (**Figure 3.1c**) create a second-order nonlinear response in the  $x$ -direction along the edges of the triangle, but the nonlinear response of opposite edges cancels out, thus the  $x$ -component of the total nonlinear electric dipole is zero, as it should be for a particle with mirror symmetry,  $x \leftrightarrow -x$ . In contrast, the  $y$ -polarized second-order nonlinear



response resulting from x-polarized (Figure 3.1b) and y-polarized (Figure 3.1d) illumination does not cancel.

### 3.3 Effect of particle symmetry on its nonlinearity



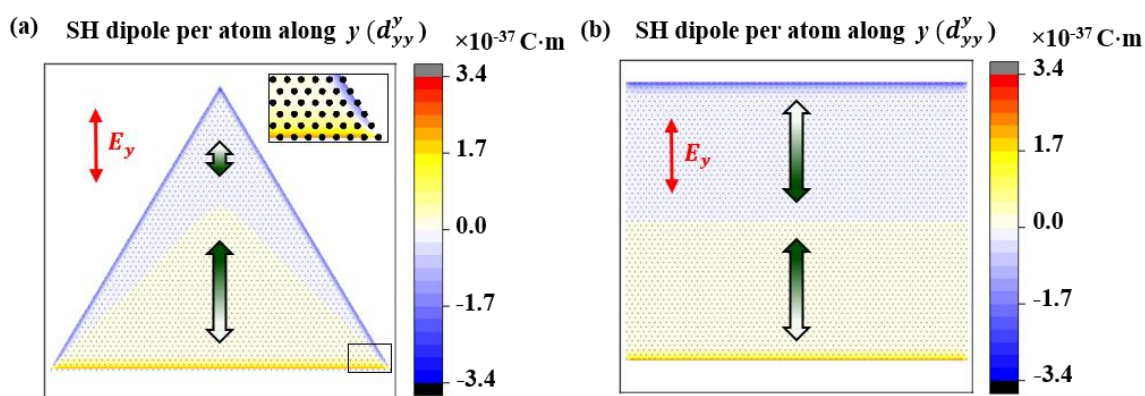
**Figure 3.2 Symmetry dependence of total linear and second order electric dipole**

(a) The schematic shows a transition from a triangular to a rectangular nanoparticle - Removal of second order nonlinear response by introduction of inversion symmetry of the nanoparticle. (b) The magnitudes of the total dipole moments  $\mathbf{P}^{(1)}$  and  $\mathbf{P}^{(2)}$  along the y-direction at the fundamental and second harmonic frequencies induced by a y-polarized fundamental wave in a particle evolving from lack of inversion symmetry to inversion symmetry.

Basic symmetry considerations [102] show that total second harmonic response is forbidden for 2-fold (rotationally) symmetric shapes such as a rectangle, but is allowed for 1-fold symmetric shapes

such as isosceles triangle. An interesting question to ask is how this selection rule appears when a triangle is gradually converted via a trapezoid into a rectangle. How does the total nonlinear electric dipole vanish? How does it depend on changes in geometry (for a given driving field)? What effect does the finite lattice size have on the changes in the induced nonlinear electric dipole? To address this, a series of calculations has been carried out for symmetric triangular, trapezoidal and rectangular particles driven by the same electric field along the symmetry axis ( $y$ -axis).

The results are shown in **Figure 3.2**. We fix the height and bottom side length of an isosceles trapezoid and increase the slope of its left and right sides by extending its top side from 0 nm to 30 nm, see **Figure 3.2(a)**. The effect of such changes in particle symmetry, from three-fold rotational symmetry via absence of rotational symmetry to two-fold rotational symmetry, on the magnitude of the total linear electric dipole  $\mathbf{P}^{(1)}$  and the total second-order electric dipole  $\mathbf{P}^{(2)}$  is shown in **Figure 3.2(b)**. The magnitude of the total linear dipole  $\mathbf{P}^{(1)}$  grows linearly as the triangle evolves into a rectangle. This is consistent with the linear polarizability of each atom being roughly independent of its neighbourhood – so more atoms translate into correspondingly higher total linear electric dipole since  $\mathbf{P}^{(1)} = \sum_k \mathbf{d}_k$ . Indeed, we should notice that the linear dipole per atom remains constant. Clearly, such a simple response is a consequence of operating in the off-resonance regime (the driving frequency to atomic resonant frequency ratio is  $\omega/\omega_0 \approx 0.19$ ). In contrast, the magnitude of the total quadratic electric dipole  $\mathbf{P}^{(2)}$  decreases linearly with the increase in the top side length. This can be explained by considering the plots of the per-atom quadratic electric dipole  $d_{yy}^y$  for the rectangle and the triangle shown in **Figure 3.3**. In the rectangle, the second-order electric dipole at the top and bottom sides is of equal magnitude but opposite phase, giving zero total effect. In case of the triangle, this cancellation does not occur. The gradual drop in the magnitude of the total second-order dipole with increasing top side length, shown in **Figure 3.2(b)**, is consistent with the cancellation of second-order dipole contributions from atoms in corresponding sections of the top and bottom sides, which leads to complete cancellation of the particle's second-order nonlinear response as it becomes rectangular. Thus, while local edge nonlinearity is also present for particle shapes with inversion symmetry, anti-phase nonlinear response of opposite edges causes cancellation of the overall second-order nonlinear response of inversion-symmetric particles.



**Figure 3.3. Second order nonlinear electric dipole distribution in a triangle and a rectangle**

Colour maps show the y-component of the atomic electric dipole at frequency  $2\omega$  for (a) the initial and (b) final particle shapes in Figure 3.2a.

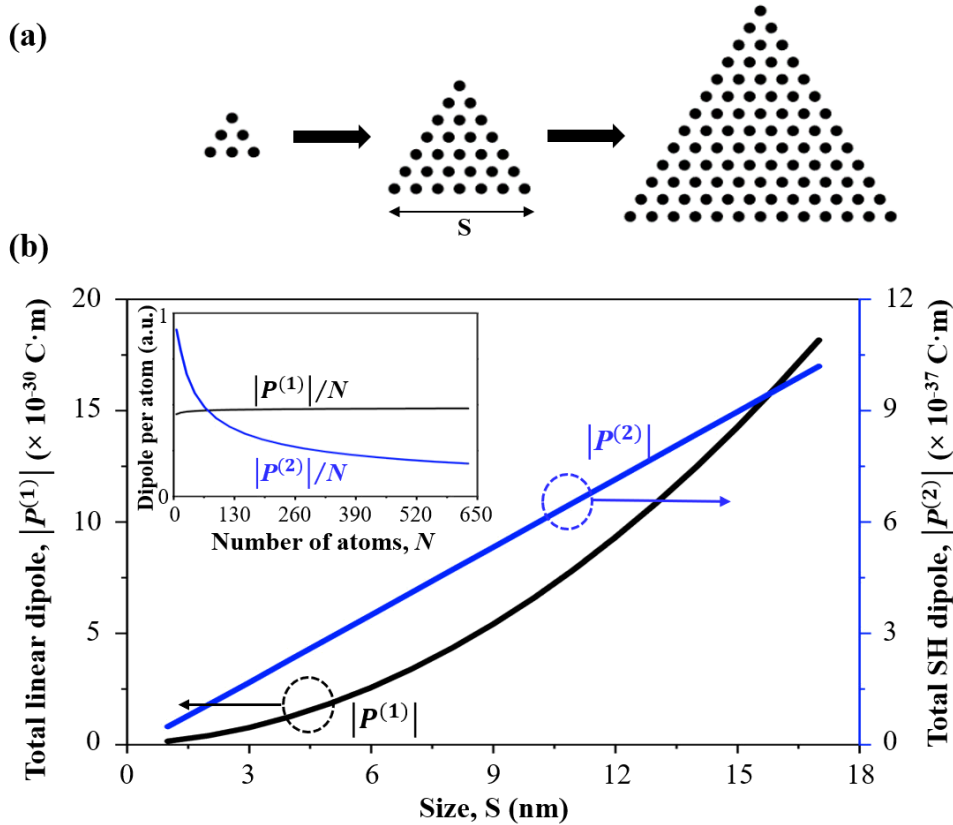
The results indicate second-order nonlinear responses with same magnitude and opposite phase for opposite edges (one rotated  $180^\circ$  relative to the other). This has an interesting implication for inverse structures (a particle and the corresponding particle-shaped hole). An inverse structure results from interchanging which side of the edge the material is on, which is equivalent to a  $180^\circ$  rotation of each segment of particle edge. Therefore, inverse structures must have second-order dipoles of same magnitude and opposite sign.

### 3.4 Effect of particle size on its nonlinearity

The electric dipoles in **Figure 3.2** show remarkably smooth dependencies on particle geometry, despite the fact that the length of the longest side of the rectangle is just 30 nm (corresponding to 61 atoms at the edge). One can therefore conjecture that whilst the nonlinear response at each point on the edge may be strongly influenced by the local orientation of the edge-cut relative to the driving field and atomic lattice, the total second-order nonlinear response can be approximated by treating edges as ‘smooth’ even in the presence of a coarse lattice. This conjecture can be tested by choosing a particle of some shape, changing its overall size (whilst keeping the lattice size fixed), driving the particle with electric field of fixed magnitude and orientation, and calculating the total induced electric dipole, just as shown in **Figure 3.4(a)**. The results of this test, for the case of triangular particles, are shown in **Figure 3.4(b)**.

The linear and second-order nonlinear electric dipoles have been calculated for triangles with side lengths from 1 nm (6 atoms in total) to 17 nm (630 atoms). Despite the coarse lattice (lattice constant of 0.5 nm), the total linear electric dipole of triangular particles  $\mathbf{P}^{(1)}$  is proportional to the number of atoms  $N$ , i.e. the linear electric dipole per atom  $\mathbf{P}^{(1)}/N$  does not change much, see inset in **Figure 3.4(b)**.

In contrast, the total second-order nonlinear electric dipole  $\mathbf{P}^{(2)}$  is proportional to the size  $S$  of the triangle's edges, i.e. to the particle's perimeter. Thus, the overall quadratic nonlinear electric dipole in mesoscopic two-dimensional particles, with centrosymmetric structure of the bulk, is proportional to the perimeter of the particle. In fact, size effects of (surface) second-order nonlinear response of metallic particles have been investigated experimentally in the past, where an increase in second-order nonlinear response with particle size has been observed for very small particles [80]. The noteworthy effect detected here is that such behaviour persists to levels of just few atoms in dielectric particles.



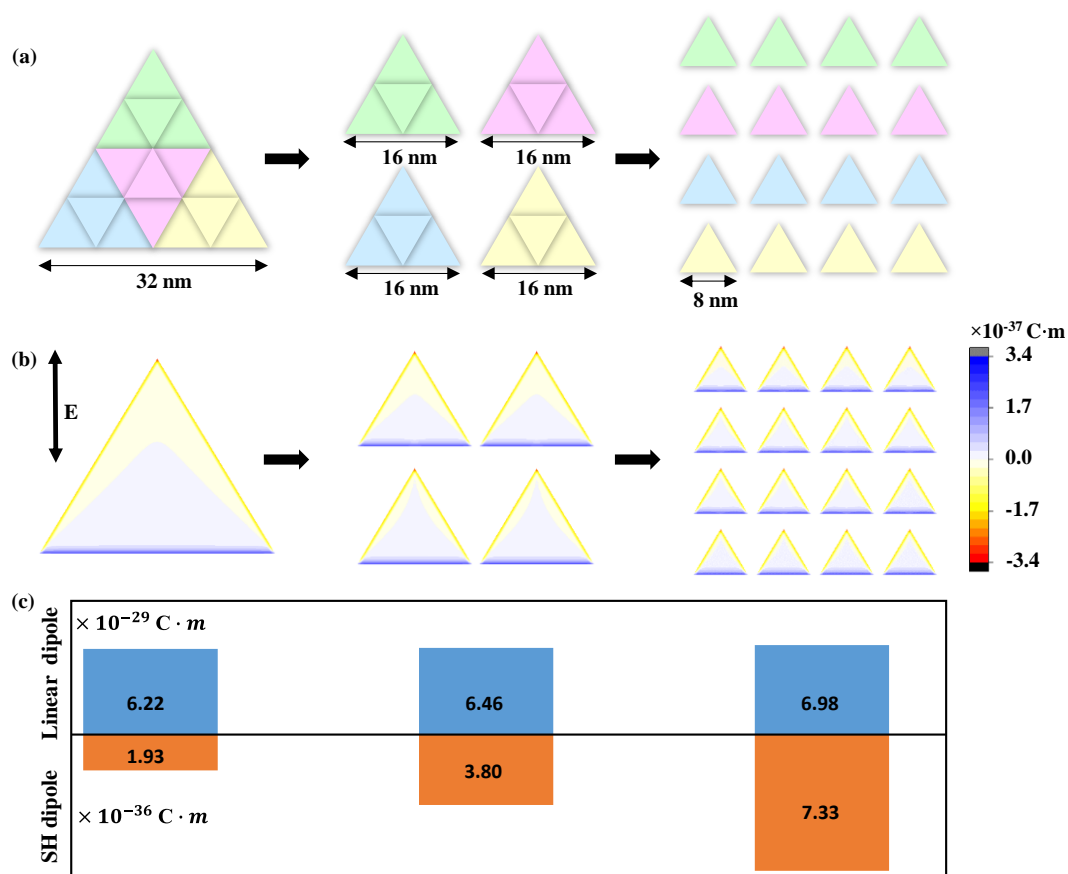
**Figure 3.4. Effect of a nanostructure's size on its linear and nonlinear response**

(a) The schematic shows how the triangular particle's size increased. (b) The magnitudes of the total dipole moments  $\mathbf{P}^{(1)}$  (black line) and  $\mathbf{P}^{(2)}$  (blue line) at the fundamental and second harmonic frequencies induced by a y-polarized fundamental wave for triangular particles of increasing size,  $S$  (from 6 to 630 atoms total). The insert shows linear and second order electric dipole per atom as functions of the total number of atoms  $N$  in the triangle.

### 3.5 Optimization strategy

The proportionality of the total second-order nonlinear electric dipole to the perimeter of the particle ( $\mathbf{P}^{(2)} \propto S$ ) suggests a simple strategy of optimizing the non-linear response of mesoscopic

structures. As illustrated by **Figure 3.5**, given a 2D particle, such as an equilateral triangle, an increased second-order nonlinear response can be achieved by substituting the particle (triangle) with smaller particles of the same shape (triangles), which have a larger combined perimeter and the same combined area. **Figure 3.5(b)** indicates how the increased number of triangles (or the increased perimeter) optimizes the second order electric dipole- the more triangles, the more edges of strong nonlinear response. As shown in **Figure 3.5(c)**, this process will increase the total length of edges, thus increasing the second-order nonlinear response, but will leave the overall number of atoms (approximately) unchanged, thus preserving the linear response.



**Figure 3.5 Optimization of the second harmonic dipole response via nanostructuring**

(a) Schematic of a large equilateral triangle structure (cut out of a hexagonal lattice of atoms) being divided into 4 and then 16 equilateral triangles. The overall area occupied by the triangles remains the same, but the length of the perimeter doubles with every step. (b) The distribution of the second harmonic (SH) dipole per atom along the y-direction, excited by y-polarized driving field. (c) The magnitude of total linear dipole and total second harmonic dipole for the cases considered in (b). The total linear dipole is almost the same in all cases, since the number of atoms in the three arrangements is almost the same. The total SH dipole is proportional to the total edge length, i.e. it doubles with every step.

## 3.6 Summary

In summary, this chapter shows how structuring of matter can lead to second order optical nonlinearity. The results in this chapter indicate that:

- (1) Coulomb interactions involving bound optical electrons cause a nonlinear optical response at the boundaries/edges of nanostructures.
- (2) 2D particles of any shape can generate second order electric dipoles locally, but only those shapes without inversion symmetry can end up a non-zero total electric dipole for normal illumination.
- (3) In a planar structure cut from a centrosymmetric lattice of harmonic oscillators, its linear electric dipole is proportional to structure's atom number, while its second order nonlinear electric dipole is proportional to the perimeter of the structure.

The proportionality and our model can instruct the design of artificial nonlinear particles, surfaces and metamaterials for optical second harmonic generation.

## Chapter 4 Model of harmonic and sum frequency generation by 2D nanostructures

### 4.1 Introduction

In nonlinear media, electromagnetic waves can interact, generating new waves at combinatorial frequencies. Depending on the generated frequency, the nonlinear phenomena can be classified as harmonic generation, sum or difference frequency generation..., which are important for optical signal processing and frequency conversion. However, a material's symmetry limits its optical nonlinearity and usually has a different influence on even and odd order nonlinearity. Therefore, a model that can study a structure's even and odd order nonlinearity simultaneously is needed for designing multifunctional nonlinear devices. In this chapter, a model of harmonic and sum frequency generation in 2D nanostructures is presented.

In order to predict the nonlinear response of a structured dielectric film, such as a nanoparticle or metamaterial unit cell, here we consider plane wave illumination (along  $z$ ) of a 2D (two-dimensional) lattice of 'atoms' consisting of charges that are confined to the  $xy$ -plane. The electromagnetic response of the single atom is strictly linear and arises from a harmonic potential [120]. The nonlinear response arises exclusively due to inter-atomic Coulomb interactions. The  $\propto 1/R^2$  dependence of the Coulomb force, where  $R$  is the inter-charge separation, gives rise a nonlinear response of optical electrons in collections of coupled atoms, as introduced in **Chapter 2**.

This basic principle of one-to-one coupling via the Coulomb force is applied to modelling of the response of collections of atoms that form particles with a square or hexagonal lattice. In order to access a highly nonlinear regime, the amplitude of the pumping electric field ( $E_0$ ) is set to  $8.68 \times 10^{10}$  V/m, corresponding to  $10^{15}$  W/cm<sup>2</sup> pump intensity. While this extreme level of intensity may not be feasible experimentally, it allows us to explore physical trends and higher-order optical nonlinearities in a regime where they are of sufficient magnitude to make numerical errors of differential equation solvers irrelevant. The pump wavelength is chosen to be 1064 nm, corresponding to an angular pump frequency  $\omega_p = 1.79 \times 10^{15}$  rad/s. In modelling of sum frequency generation, we pump the particle at two frequencies,  $\omega_p$  and  $0.1 \omega_p$ , simultaneously. The ratio of 10 of the two pump frequencies is chosen to make the sum frequency order easily recognizable.

By solving the coupled equations of motion of all optical electrons within 2D nanoparticles numerically, we calculate the displacement of each optical electron in the time domain. We solve the coupled system of differential equations starting without optical electron displacement and

allowing transitional effects to pass before analysing the oscillation of all electrons over 1000 periods of the driving field (see **Section 2.4** for more details). Finally, through Fourier transformation, we got the response of the particle in frequency domain.

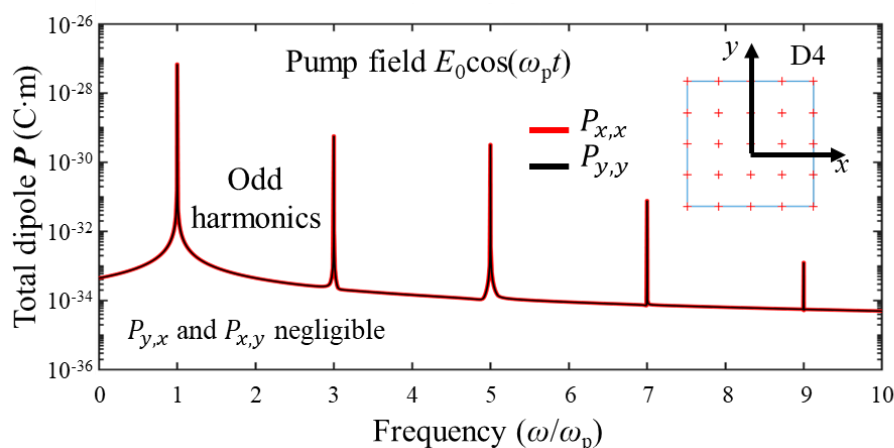
According to symmetry analysis, a structure in the  $xy$ -plane can radiate even order harmonics along  $z$  when it is of no rotational symmetry or 3-fold rotational symmetry [84, 102] as discussed in **Section 1.3**. In order to reveal how nonlinear frequency generation appears/vanishes in cases where it is allowed/forbidden, harmonic and sum frequency generation are studied in simple 2D particles of either square shape (D4 symmetry, with square lattice) in **Section 4.2** and triangular shape (D3 symmetry, with hexagonal lattice) in **Section 4.3**. Pump field induced multipoles other than the electric dipole in nanostructures can also radiate harmonics but not along the  $z$  direction and this is studied in **Section 4.4**.

## 4.2 Harmonic and sum-frequency generation in nanostructures of D4 symmetry

### 4.2.1 Harmonic and sum-frequency generation in a square particle

First, the harmonic generation in a square particle of 25 atoms is studied, see **Figure 4.1**. The frequency-dependence of the total electric dipole moment  $\mathbf{P}$  generated by electric pump field  $E_0 \cos(\omega_p t)$  is calculated through the method discussed in **Section 2.4**.  $P_{i,j}$  is used to refer to the  $i$ -component of the dipole moment caused by a  $j$ -polarized pump field, where  $i,j$  is  $x$  or  $y$ . As required by symmetry,  $x$ -polarized excitation generates a dipole only along  $x$ , while  $y$ -polarized excitation generates a dipole only along  $y$  with the same magnitude. i.e.  $P_{x,x}=P_{y,y}$  are observed, while  $P_{x,y}$  and  $P_{y,x}$  are forbidden. As expected for a particle with even-fold rotational symmetry [84, 102], only odd harmonics  $\mathbf{P}^{(1)}$ ,  $\mathbf{P}^{(3)}$ ,  $\mathbf{P}^{(5)}$ ,  $\mathbf{P}^{(7)}$  and  $\mathbf{P}^{(9)}$  are observed— which appear as peaks in **Figure 4.1**.

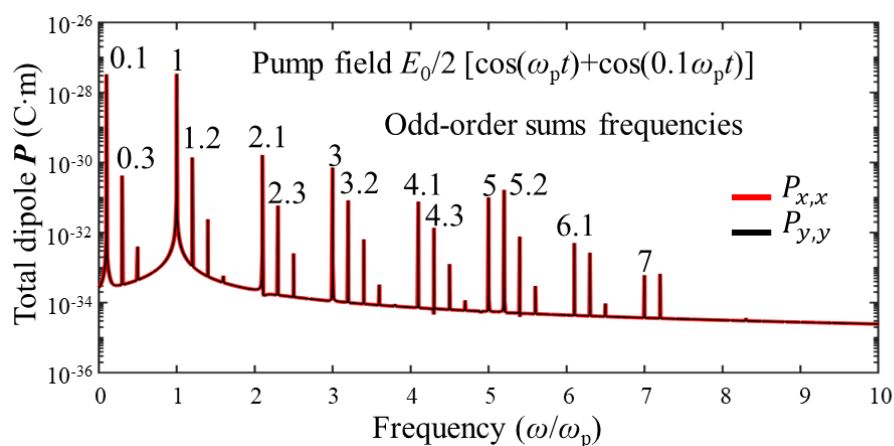




**Figure 4.1 Harmonic generation in a nanoparticle of D4 symmetry**

Frequency dependence of the electric dipole moment of a square particle (blue outline) consisting of 25 atoms (red crosses) in response to optical pumping at a single frequency  $\omega_p$ .  $P_{y,x}$  indicates the y-component of the particle's electric dipole moment caused by x-polarized pumping.

Harmonic generation is a special case of sum frequency generation. The latter becomes apparent when pumping the square particle with a combination of two frequencies,  $\omega_p$  and  $0.1\omega_p$ . This is illustrated by **Figure 4.2**, which considers a pump field  $E_0/2[\cos(\omega_p t) + \cos(0.1\omega_p t)]$ .

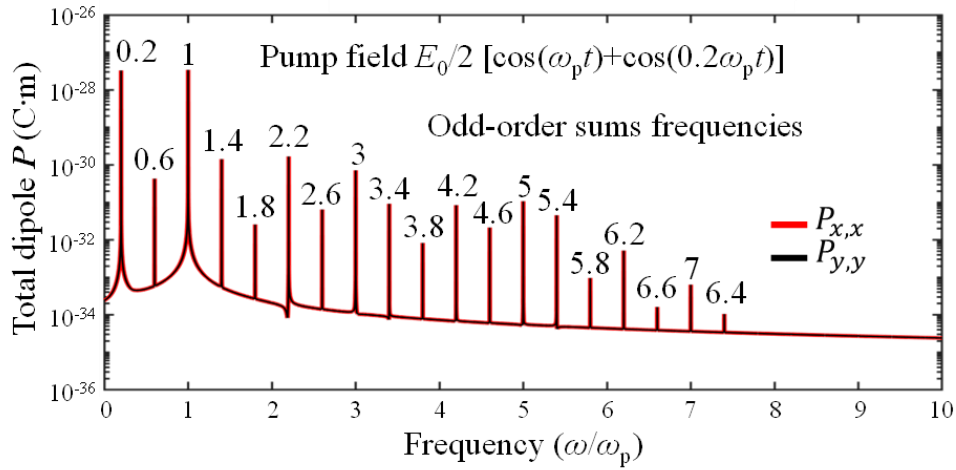


**Figure 4.2 Sum frequency generation in a nanoparticle of D4 symmetry**

Frequency dependence of the electric dipole moment of a square particle consisting of 25 atoms in response to optical pumping at a combination of two frequencies,  $\omega_p$  and  $0.1\omega_p$ .

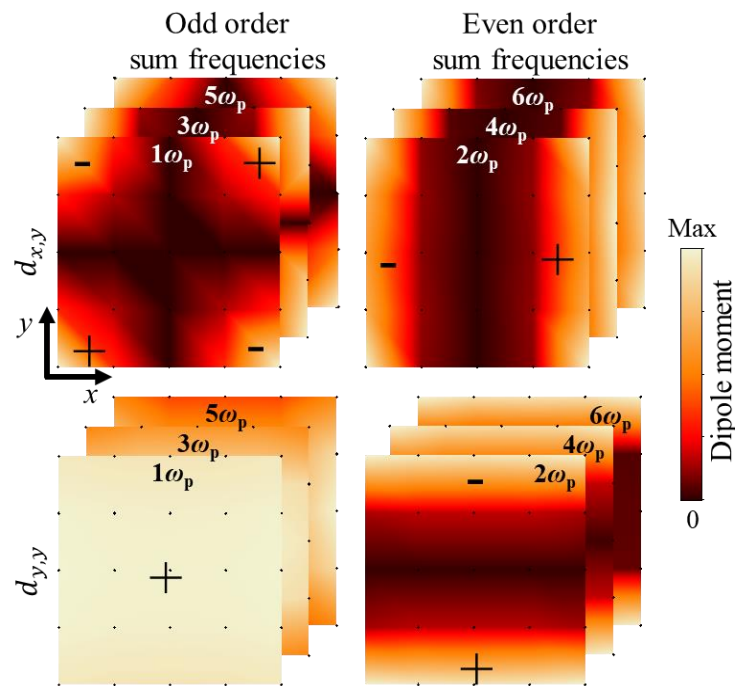
As for harmonic generation, also mixed frequency pumping results in an electric dipole moment of the particle that is parallel to the pump polarization,  $P_{x,x}$  and  $P_{y,y}$ . Only odd order sum frequencies are observed, i.e. odd harmonics of the higher and lower pump frequencies ( $\omega_p, 3\omega_p, 5\omega_p, \dots$  and  $0.1\omega_p, 0.3\omega_p, \dots$ ) and sums of odd combinations of both pump frequencies ( $1.2\omega_p, 2.1\omega_p, 2.3\omega_p, \dots$ ), indicating that the model can predict wave mixing in 2D particles.

We observe that different dipole moments of the same order tend to be of similar magnitude, but resonant enhancement near the atomic resonance at  $5.26 \omega_p$  and the background level also influence the magnitude of the calculated dipole moments. Similar results are obtained for different choices of pump frequency. For example, **Figure 4.3** shows sum frequency generation of the square particle pumped by a combination of two frequencies,  $\omega_p$  and  $0.2\omega_p$ .



**Figure 4.3 Sum frequency generation in a nanoparticle of D4 symmetry**  
 Frequency dependence of the electric dipole moment of a square particle consisting of 25 atoms in response to optical pumping at a combination of two frequencies,  $\omega_p$  and  $0.2\omega_p$ .

### 4.2.2 Electric dipole moment distribution in a square particle



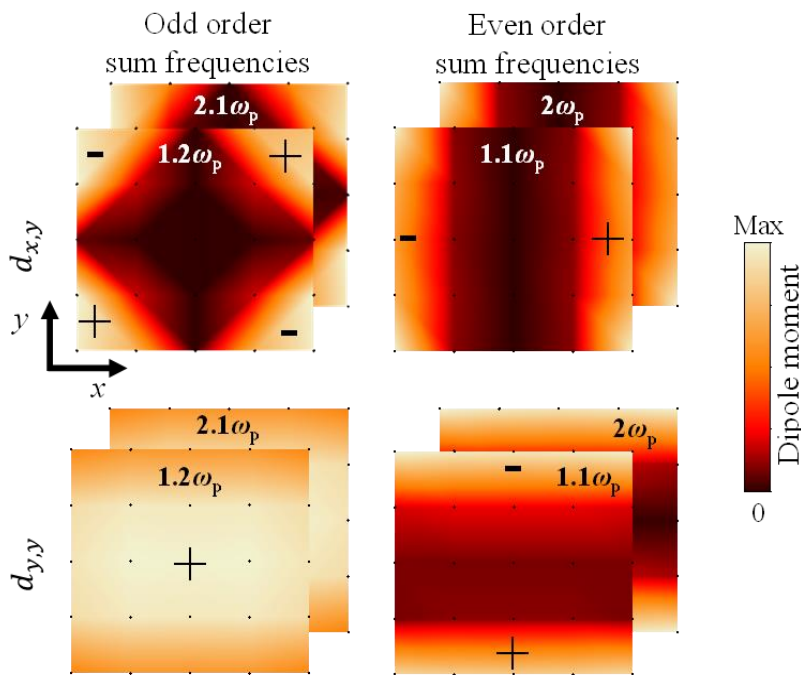
**Figure 4.4** Electric dipole moment distribution at harmonic frequencies in a square particle

Magnitude (colours) and sign (“+” and “-”) of the dipole moment per atom,  $\mathbf{d}$ , generated at harmonic frequencies (multiples of  $\omega_p$ ) in response to pumping at frequency  $\omega_p$ .  $\mathbf{d}_{y,x}$  indicates the y-component of the electric dipole per atom caused by x-polarized pumping. The top (bottom) row shows the dipole component orthogonal (parallel) to the pump polarization. Stacked images for different – either even or odd – harmonics show the same qualitative behaviour.

The origin of harmonic and sum frequency generation is revealed by the distribution of atomic dipole moments at the relevant frequencies. **Figure 4.4** illustrates this for the square particle pumped at frequency  $\omega_p$ . The top row shows the distributions of dipole components oriented normal to the pump polarization at odd (left) and even (right) harmonic frequencies. Notably, all harmonics are generated locally, but the symmetry of the particle implies that the atomic electric dipole component normal to the pump field has the same magnitude and a  $\pi$  phase difference on opposite sides of the structure, resulting in overall cancellation. Therefore, the structure of D4 symmetry has no total electric dipole moment in the direction normal to the pump polarization, which is consistent with what shown in **Figure 4.1-4.3**, where  $P_{x,y}=P_{y,x}=0$ . The total electric dipole component parallel to the pump polarization also cancels for even harmonics (bottom row, right). In contrast, the dipole component parallel to the pump polarization does not vanish for odd harmonics (bottom row, left). In-phase oscillation of all atoms causes the atomic dipoles to add up to a total electric dipole moment of the particle at odd harmonic frequencies.

Indeed, the symmetry of the experimental arrangement, including structure and pump beam, means that no light can be emitted at even harmonics along  $z$  and therefore the total electric dipole moment must vanish. In these cases, the fields “radiated” from different parts of the particle cancel by destructive interference in the normal direction. Radiation in other directions may not vanish, can be described in terms of other multipoles, and will be discussed in **Section 4.4**. Here, we describe radiation emitted normal to the plane of the particle.

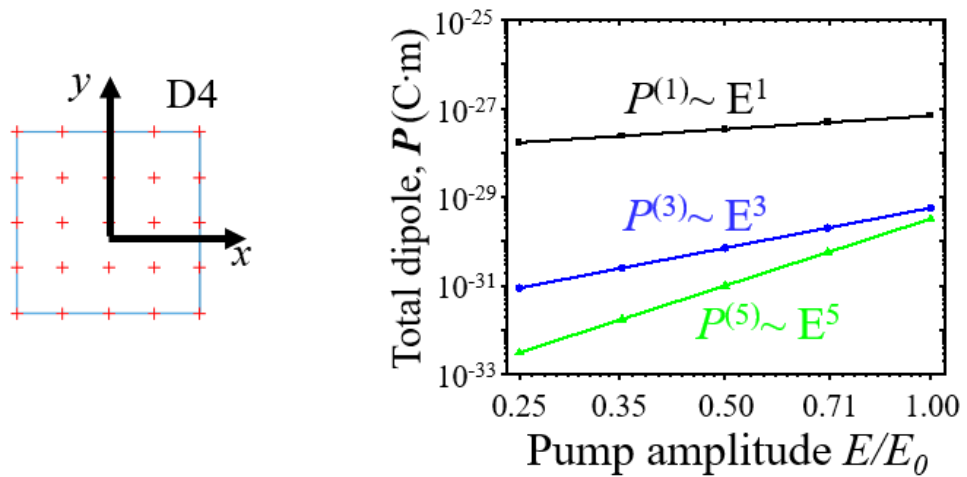
While the allowed component of odd harmonic generation originates from the entire particle, one can notice that the even harmonics – which do not add up to any total electric dipole moment – are associated with edges of the particle, as already seen in **Chapter 3**.



**Figure 4.5 Electric dipole moment distribution at sum frequencies in a square particle**  
 Magnitude (colours) and sign (“+” and “-”) of the dipole moment per atom,  $\mathbf{d}$ , generated at lowest-order sum frequencies in response to pumping at frequencies  $\omega_p$  and  $0.1\omega_p$ . The top (bottom) row shows the dipole component orthogonal (parallel) to the pump polarization. Stacked images for different – either even or odd – sum frequencies show the same qualitative behaviour.

Dipole distributions for sum frequency generation with different pump frequencies (see **Figure 4.5**) have the same characteristics as those for harmonic generation of the same order.

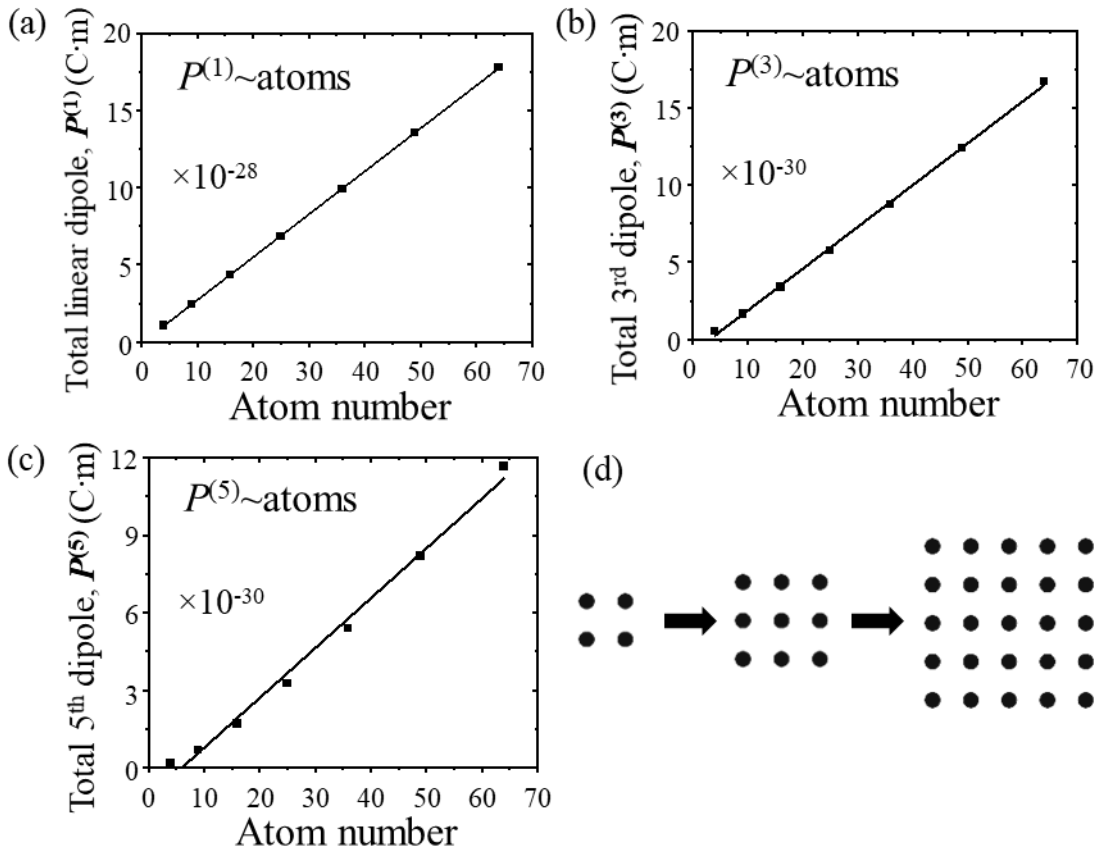
### 4.2.3 Pump power and size dependence of a square particle's electric dipole



**Figure 4.6 Pump power dependence of a square particle's electric dipole moment**

Scaling of harmonic generation with the pump field amplitude for a square particle of 25 atoms. Here the pump field and the generated dipole are polarized along the same direction.

The pump power dependence of the generated harmonics is illustrated by **Figure 4.6**, which shows the electric dipole moment generated in the square particle for different pump field amplitudes at different harmonic frequencies. The magnitude of the electric dipole moments at the first, third and fifth harmonic frequencies –  $P^{(1)}$ ,  $P^{(3)}$ ,  $P^{(5)}$  – is proportional to the first, third and fifth power of the pump amplitude, as expected for first, third and fifth order (non)linear optical processes.



**Figure 4.7** Size dependence of a square particle’s electric dipole moment

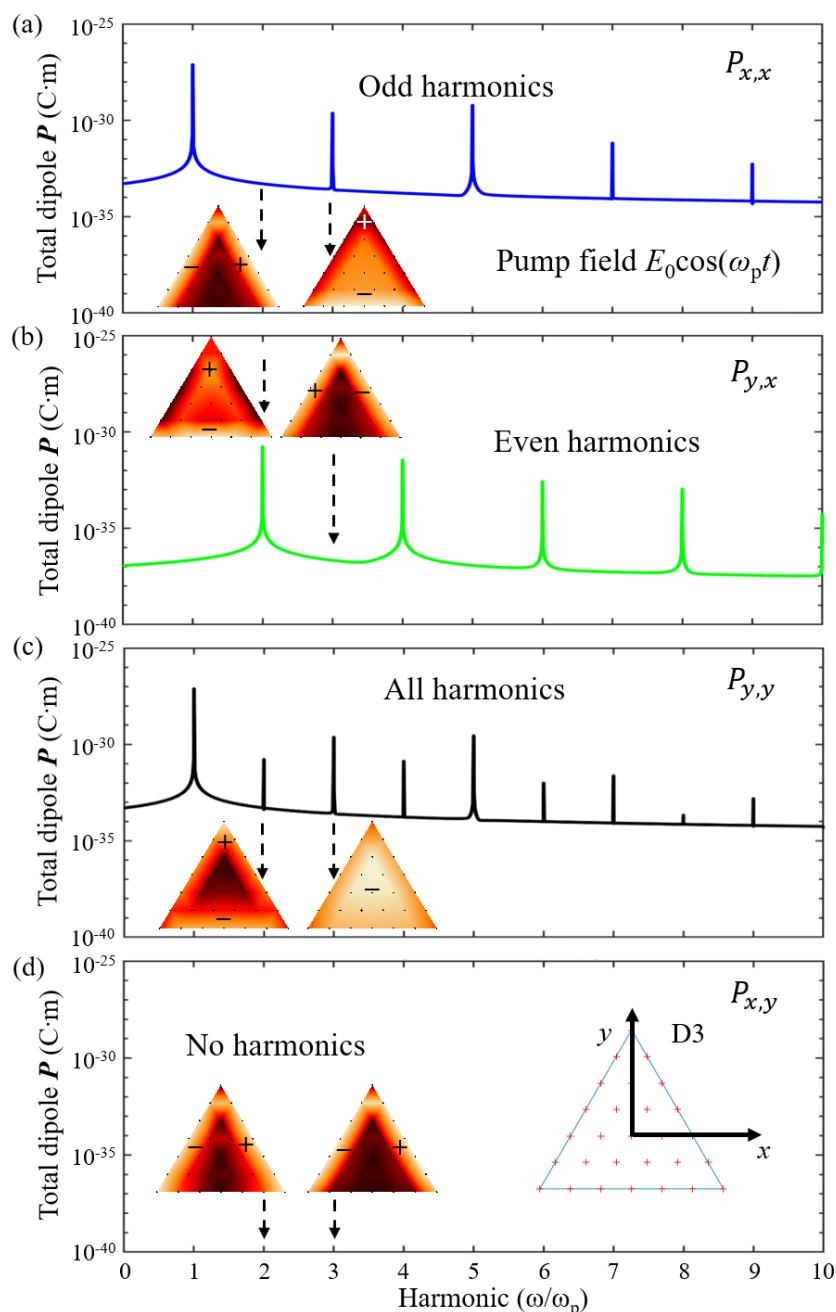
Scaling of the particle’s electric dipole moment with its size at the first three odd harmonic frequencies (a)  $P^{(1)}$ , (b)  $P^{(3)}$ , (c)  $P^{(5)}$ , corresponding to peaks in **Figure 4.1**. These odd order dipole moments scale with its number of atoms (area). (d) The schematic showing how the square particle’s size increased.

The dependence of the nanoparticle’s odd harmonic response on its size is shown by **Figure 4.7**. The total nonlinear electric dipole at the generated odd harmonics - such as the first, third and fifth harmonics  $P^{(1)}$ ,  $P^{(3)}$ ,  $P^{(5)}$  - is proportional to the total number of atoms (2D particle area).

### 4.3 Harmonic and sum-frequency generation in nanostructures of D3 symmetry

#### 4.3.1 Harmonic generation in a triangle particle

While the even-fold rotational symmetry discussed above only permits odd order nonlinear electric dipole moments, three-fold rotational symmetry allows a more complex nonlinear response. Now we will discuss harmonic generation in a particle of D3 symmetry, a triangular particle consisting of 28 atoms arranged in a hexagonal lattice as shown by the insert in **Figure 4.8d**.



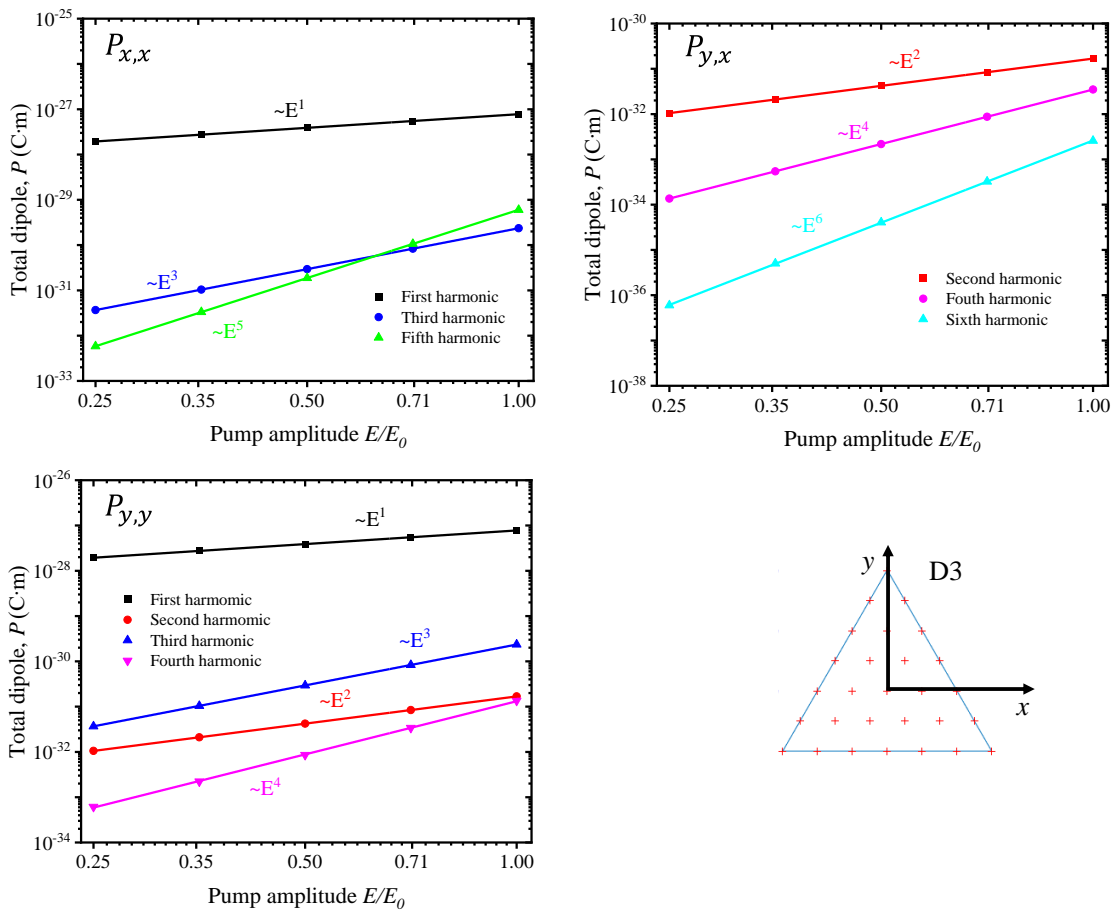
**Figure 4.8 Harmonic generation in a nanoparticle of D3 symmetry**

(a)-(d) Frequency-dependence of the electric dipole moment of a triangular particle pumped at frequency  $\omega_p$ . Components of the dipole moment (a, c) parallel and (b, d) orthogonal to the (a, b)  $x$ -polarized and (c, d)  $y$ -polarized pump field. Absence of curves in case (d) indicates cancellation of the electric dipole component at all frequencies. The inset shows the outline (blue line) and the 28 atoms (red crosses) of the triangular particle. Colourmaps show the distribution of the atomic dipole moments at the 2<sup>nd</sup> and 3<sup>rd</sup> harmonic frequencies, which are representative of even and odd harmonics. Colour represents the dipole magnitude and regions oscillating in anti-phase are indicated by opposite signs as in **Figure 4.4**.

The spectral dependence of the triangular particle’s electric dipole moment in response to pumping at frequency  $\omega_p$  is shown by **Figure 4.8**. An x-polarized pump field generates an electric dipole moment of the particle along x at odd harmonic frequencies (**Figure 4.8a**) and along y at even harmonic frequencies (**Figure 4.8b**). A y-polarized pump field generates a dipole moment along y only at all harmonic frequencies (**Figure 4.8c**), while no harmonics are allowed along x (**Figure 4.8d**).

The distribution of the atomic dipole moments within the nanoparticle is shown for the second and third harmonic frequencies (insets in **Figure 4.8a-d**), which are representative of the even and odd harmonic cases. While the particle exhibits local atomic oscillation along x and y at all harmonics, overall cancellation of components of the particle’s electric dipole moment at even (**Figure 4.8a**), odd (**Figure 4.8b**) or all (**Figure 4.8d**) harmonics results from charge oscillations with equal amplitude and opposite phase at opposite edges of the triangle.

**4.3.2 Pump power and size dependence of a triangle particle’s electric dipole**

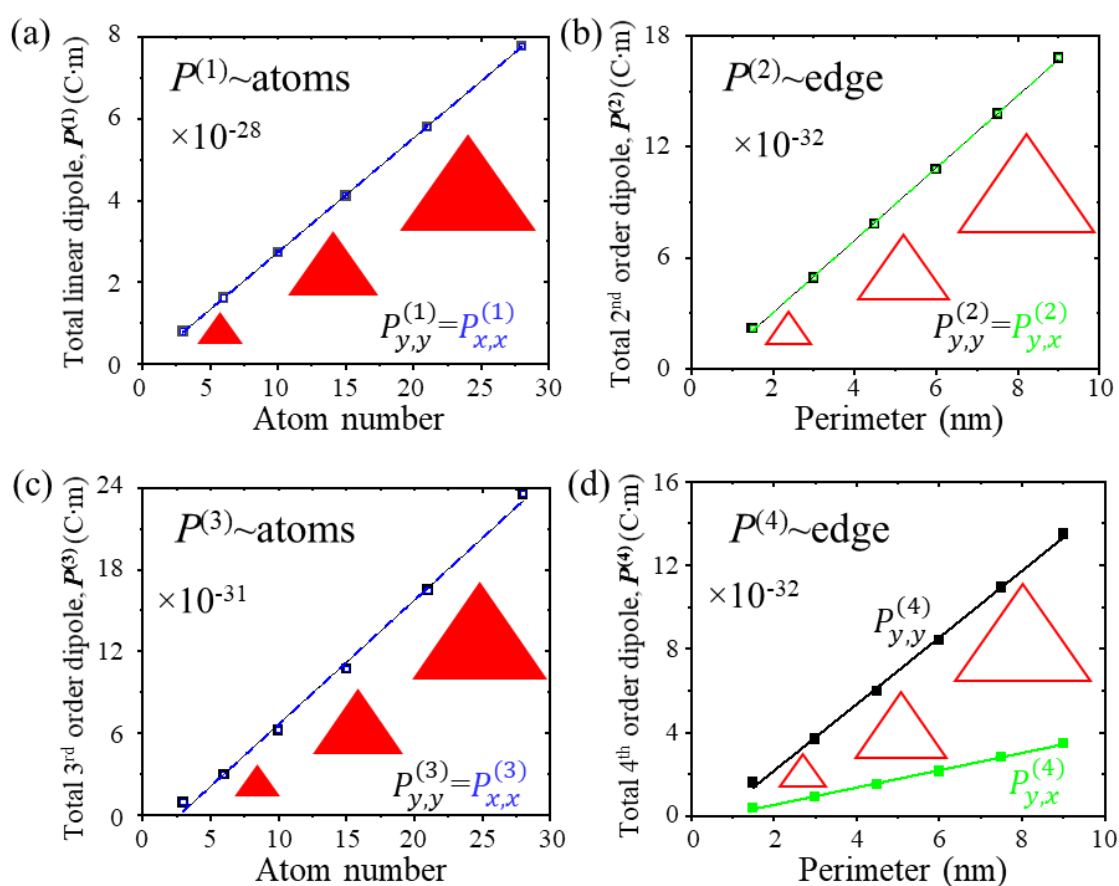


**Figure 4.9 Pump power dependence of a triangle particle’s electric dipole moment**  
 Scaling of harmonic generation with the pump field amplitude for a triangle particle of 28 atoms.



The electric dipole moment of a triangle particle as a function of pump electric field amplitude is shown in **Figure 4.9**. The electric dipole moment at the  $k^{\text{th}}$  harmonic is proportional to the  $k^{\text{th}}$  power of the pump field amplitude, causing higher harmonics to vanish quickly with reducing pump amplitude, as it should be.

It has been reported that the total linear and second-order nonlinear responses of a particle scale differently with its size. For a 3D particle made from centrosymmetric material, the total linear electric dipole moment is proportional to its volume (number of atoms), while the second-order dipole is proportional to its surface area [80]. For a 2D particle, as considered here, the linear electric dipole moment is proportional to its area (number of atoms), while the second-order electric dipole is proportional to its perimeter [120] as discussed in **Chapter 3**. However, how does particle size affect higher order harmonics?



**Figure 4.10** Size dependence of a triangle particle's electric dipole moment

Scaling of the particle's electric dipole moment with its size at the first four harmonic frequencies (a)  $P^{(1)}$ , (b)  $P^{(2)}$ , (c)  $P^{(3)}$  and (d)  $P^{(4)}$ , corresponding to peaks in **Figure 4.8**. Inserts in (a)-(d) are schematics showing how the square particle's area/perimeter increases.

**Figure 4.10** shows how the electric dipole moment of a triangular 2D particle changes with particle size. The magnitudes of the total dipole moments,  $P^{(1)}$ ,  $P^{(2)}$ ,  $P^{(3)}$ ,  $P^{(4)}$ , at the first four harmonic frequencies are shown for triangular particles with perimeter from 1.5 nm (3 atoms in total) to 9 nm (28 atoms). We find that the total nonlinear electric dipole at odd harmonics is proportional to the total number of atoms (2D particle area), while the dipole at even harmonics is proportional to the particle's perimeter. At the first three harmonic frequencies, x-polarized and y-polarized pump light induce dipole moments of the same magnitude, while at the fourth harmonic  $P_{y,y}^{(4)} = 4P_{y,x}^{(4)}$ .

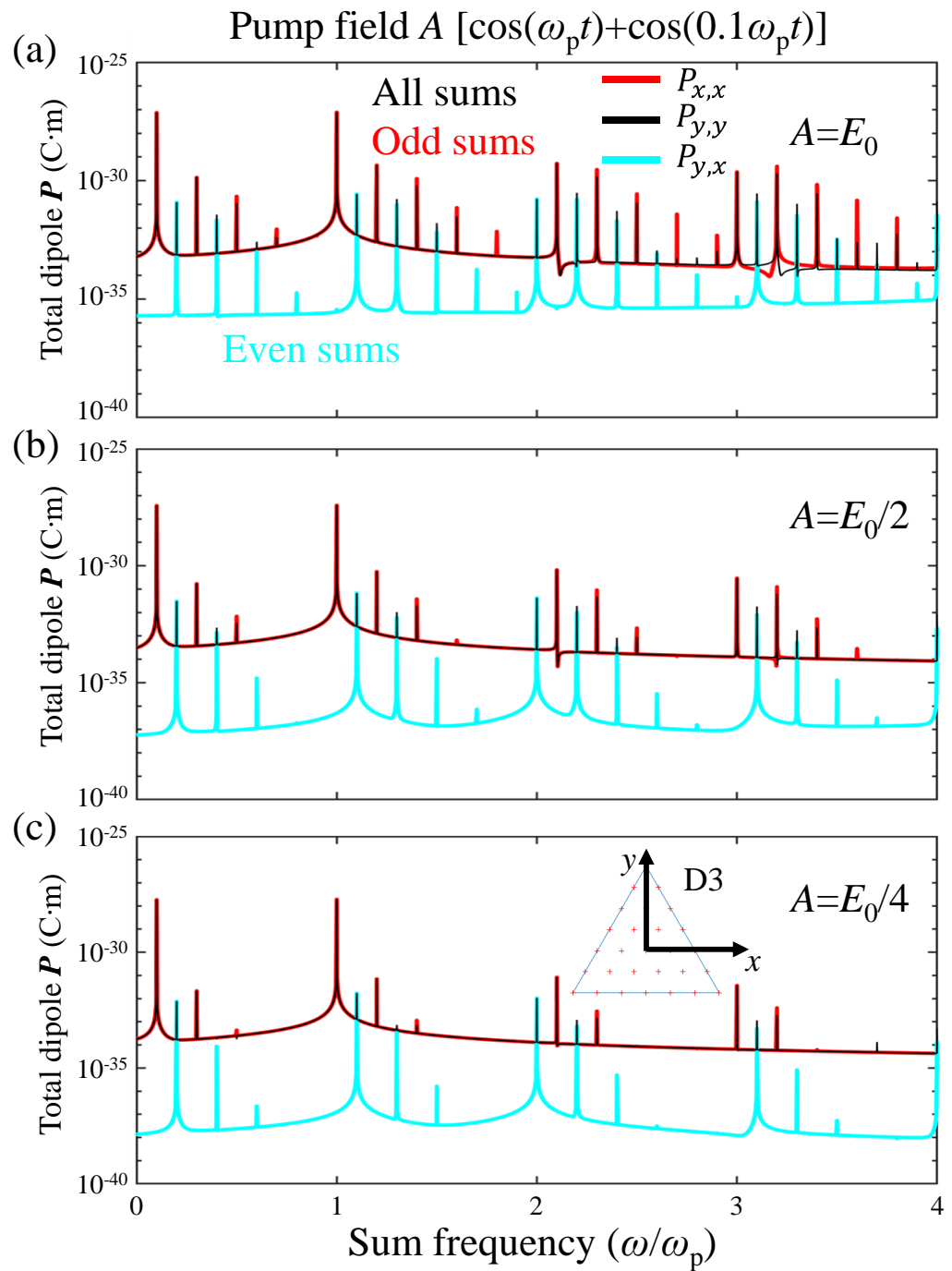
### 4.3.3 Sum frequency generation in a triangle particle

From the above discussion, we know that only odd order sum frequency generation is allowed in square particles. However, the triangle particles support a more complex sum frequency generation.

The sum frequency generation in a triangle with co-polarized pumping field  $A[\cos(\omega_p t) + \cos(0.1\omega_p t)]$  is shown in **Figure 4.11**, where  $A = E_0, E_0/2, E_0/4$ . When the pump electric fields at frequency  $\omega_p$  and  $0.1\omega_p$  are polarized along the x direction, odd order sum frequencies are generated along x ( $0.1\omega_p, \omega_p, 1.2\omega_p, 1.4\omega_p, 1.6\omega_p, 2.1\omega_p \dots$ ) and even order sum frequencies are generated along y ( $0.2\omega_p, 0.4\omega_p, 1.1\omega_p, 1.3\omega_p, 2\omega_p, 3.1\omega_p \dots$ ). When the pump fields are polarized along the x direction, all sum frequencies are allowed in the y direction while no dipoles can be generated along the x direction. This behaviour consistent with our earlier observations for harmonic generation.

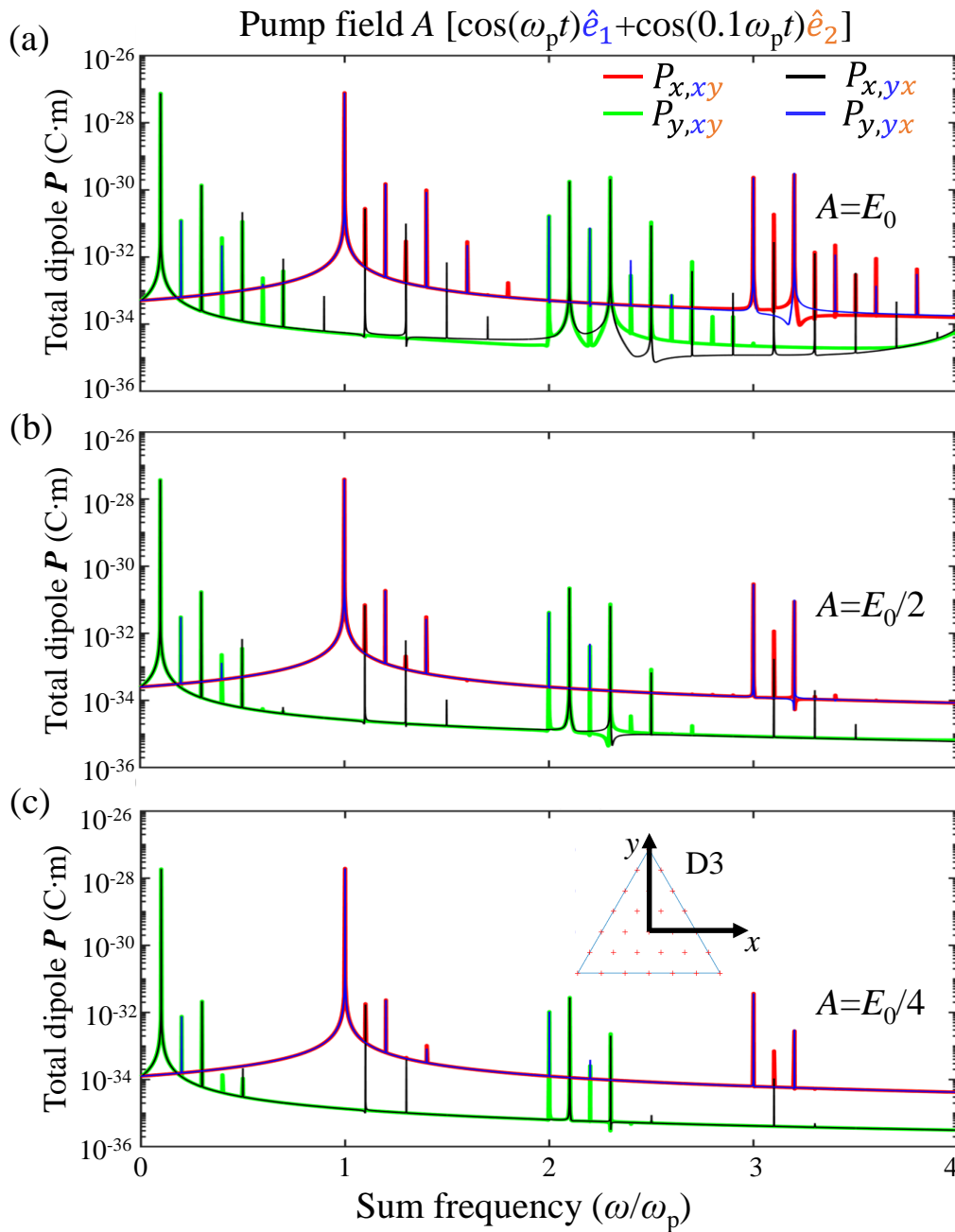
Sum frequency generation in case of cross-polarized pump fields is shown in **Figure 4.12**. When electric field at  $\omega_p$  is polarized along x and electric field at  $0.1\omega_p$  is polarized along y, sum frequencies along x at  $\omega_p, 1.1\omega_p, 1.2\omega_p, 1.3\omega_p, 1.4\omega_p \dots 3\omega_p, 3.1\omega_p, 3.2\omega_p, 3.3\omega_p, 3.4\omega_p \dots$  (odd number of  $E_x$ ) are generated; sum frequencies along y at  $0.1\omega_p, 0.2\omega_p, 0.3\omega_p, 0.4\omega_p, \dots 2\omega_p, 2.1\omega_p, 2.2\omega_p, 2.3\omega_p, 2.4\omega_p \dots$  (even number of  $E_x$ ) are generated. When electric field at  $\omega_p$  is polarized along y and electric field at  $0.1\omega_p$  is polarized along x, sum frequencies along x at  $0.1\omega_p, 0.3\omega_p, 0.5\omega_p, \dots 1.1\omega_p, 1.3\omega_p, 1.5\omega_p \dots 2.1\omega_p, 2.3\omega_p, 2.5\omega_p \dots$  (odd number of  $E_x$ ) are generated; sum frequencies along y at  $0.2\omega_p, 0.4\omega_p, \dots \omega_p, 1.2\omega_p, 1.4\omega_p, \dots 2\omega_p, 2.2\omega_p, \dots 3\omega_p \dots$  (even number of  $E_x$ ) are generated. In summary, x-polarized electric dipole moments are generated at sum frequencies containing an odd multiple (1, 3, ...) of the x-polarized pump frequency and generated y-polarized sum frequencies contain an even multiple (0, 2, ...) of the x-polarized pump frequency.

The sum frequency generation also depends on the pump electric field's strength. When the pump field magnitude increases from  $E_0/4$  to  $E_0$ , more and more sum frequency components emerge, see **Figure 4.11** and **Figure 4.12**.



**Figure 4.11 Sum frequency generation in a D3 structure with co-polarized pumping**

(a)-(c) Frequency dependence of the electric dipole moment of the triangular particle of 28 atoms (inset) in response to pumping at a combination of two frequencies,  $\omega_p$  and  $0.1\omega_p$  for different pump electric field amplitudes of (a)  $E_0$ , (b)  $E_0/2$ , (c)  $E_0/4$ .



**Figure 4.12 Sum frequency generation in a D3 structure with cross-polarized pumping**

(a)-(c) Frequency dependence of the electric dipole moment of the triangular particle (inset) in response to pumping at two frequencies,  $\omega_p$  and  $0.1\omega_p$ , where the pump fields at different frequencies have orthogonal polarizations.  $P_{i,jk}$  refers to the  $i$ -component of the dipole moment caused by  $j$ -polarized pump field at  $\omega_p$  and  $k$ -polarized pump field at  $0.1\omega_p$ , where  $i,j,k$  is  $x$  or  $y$ . Different panels show different pump electric field amplitudes of (a)  $E_0$ , (b)  $E_0/2$ , (c)  $E_0/4$ .

#### 4.4 Multipole contributions to harmonic generation

While radiation normal to the plane of the 2D particle pumped at normal incidence is determined by its electric dipole moment, other multipoles [121] contribute to radiation in other directions.

The  $\alpha$ -component of the particle's total electric dipole moment is given by

$$P_\alpha = \int d^3\mathbf{r} \rho(\mathbf{r}) r_\alpha = -q \sum_{i=1}^N r_{i,\alpha} \quad (4.1)$$

where  $\rho(\mathbf{r})$  is the charge density as a function of position  $\mathbf{r}$ . In our 2D case, only  $P_x$  and  $P_y$  are allowed and the radiated power is given by the following expression, where  $Z_0$  is the impedance of free space,  $c$  is the speed of light and  $k = \omega/c$ .

$$\mathcal{P}^{(P)} = \frac{c^2 Z_0}{12\pi} k^4 \|\mathbf{P}\|_2^2 = \frac{c^2 Z_0}{12\pi} k^4 (|P_x|^2 + |P_y|^2) \quad (4.2)$$

The  $\alpha$ -component of the particle's magnetic dipole moment is

$$m_\alpha = \frac{1}{2c} \int d^3\mathbf{r} [\mathbf{r} \times \mathbf{J}(\mathbf{r})]_\alpha = \frac{-q}{2c} \sum_{i=1}^N [(\mathbf{R}_i + \mathbf{r}_i) \times \dot{\mathbf{r}}_i]_\alpha \quad (4.3)$$

where  $\mathbf{J}$  is the current density and  $\dot{\mathbf{r}}_i$  is the electron velocity. Here, only  $m_z$  is allowed and the radiated power is

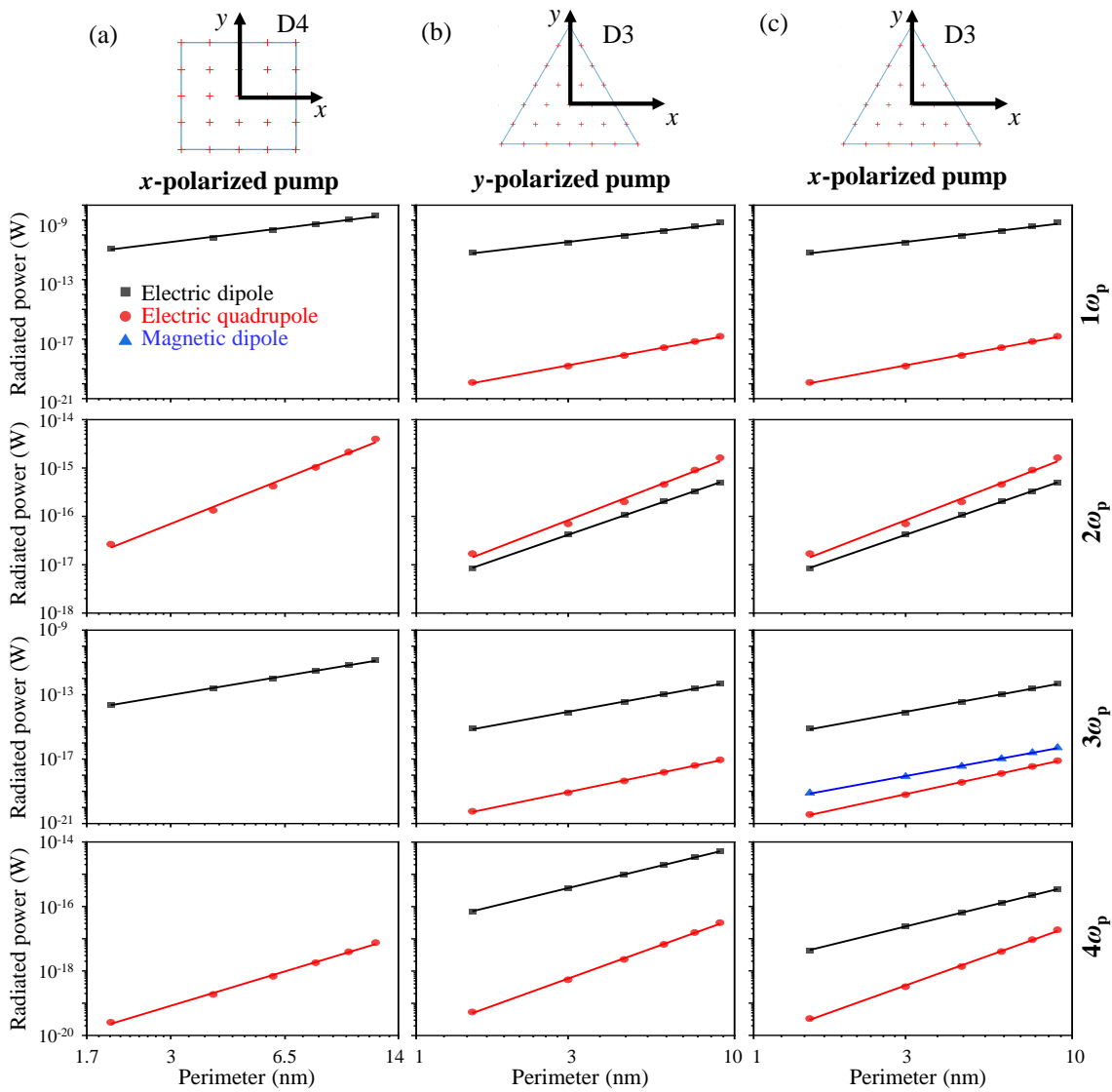
$$\mathcal{P}^{(m)} = \frac{c^2 Z_0}{12\pi} k^4 \|\mathbf{m}\|_2^2 = \frac{c^2 Z_0}{12\pi} k^4 |m_z|^2 \quad (4.4)$$

The  $\alpha, \beta$ -component of the particle's electric quadrupole is given by

$$\begin{aligned} Q_{\alpha,\beta} &= \frac{1}{2} \int d^3\mathbf{r} \rho(\mathbf{r}) \left[ r_\alpha r_\beta - \frac{1}{3} \delta_{\alpha,\beta} r^2 \right] \\ &= \frac{q}{2} \sum_{i=1}^N \left[ R_{i,\alpha} R_{i,\beta} - \frac{1}{3} \delta_{\alpha,\beta} \mathbf{R}_i^2 - (R_{i,\alpha} + r_{i,\alpha})(R_{i,\beta} + r_{i,\beta}) + \frac{1}{3} \delta_{\alpha,\beta} (\mathbf{R}_i + \mathbf{r}_i)^2 \right] \\ &= \frac{q}{2} \sum_{i=1}^N \left[ -R_{i,\alpha} r_{i,\beta} - R_{i,\beta} r_{i,\alpha} - r_{i,\alpha} r_{i,\beta} + \frac{1}{3} \delta_{\alpha,\beta} (2\mathbf{R}_i \mathbf{r}_i + r_i^2) \right] \end{aligned} \quad (4.5)$$

where  $\delta_{\alpha,\beta}$  is the Kronecker delta. In our geometry,  $Q_{x,x}$ ,  $Q_{y,y}$  and  $Q_{x,y} = Q_{y,x}$  are allowed and the radiated power is

$$\mathcal{P}^{(Q)} = \frac{c^2 Z_0}{40\pi} k^6 \sum_{\alpha,\beta} |Q_{\alpha,\beta}|^2 = \frac{c^2 Z_0}{40\pi} k^6 (2|Q_{x,y}|^2 + |Q_{x,x}|^2 + |Q_{y,y}|^2) \quad (4.6)$$



**Figure 4.13** Power radiated by different multipoles as a function of particle perimeter

Results are shown for particles of (a) D4 and (b, c) D3 symmetry located in the  $xy$ -plane as a function of particle perimeter. Only the electric dipole (black) radiates along  $z$ .

**Figure 4.13** shows the power radiated by different multipoles for the square and triangular particles, where the coordinate origin is placed at the centre of each particle. For the square particle, electric dipole radiation is emitted at odd harmonics and considerably weaker electric quadrupole radiation ( $Q_{x,x}$ ,  $Q_{y,y}$ ) is emitted at even harmonics, while magnetic dipole contributions are negligible (forbidden), see **Figure 4.13(a)**. Therefore, only odd harmonics will be radiated along  $z$ . In other directions, all harmonics will be radiated, with even harmonics being several orders of magnitude weaker than odd harmonics of similar order. For the triangular particle, electric dipole radiation dominates at odd harmonics, while electric dipole and quadrupole radiation have a comparable magnitude at the second harmonic frequency, **Figure 4.13(b-c)**.

The multipole contributions are also revealed by the polarization surface densities (electric dipole distributions) in **Figure 4.4** and **Figure 4.8**. For example, for both the square and triangular particles, the net quadrupole at even harmonics originates from electrons on opposite edges of the particle, that oscillate towards and away from each other ( $\rightarrow\leftarrow, \leftarrow\rightarrow$ ). The net magnetic dipole at the third harmonic frequency for x-polarized pumping of the triangular particle arises from anti-parallel electron oscillations ( $\uparrow\downarrow, \downarrow\uparrow$ ), see **Figure 4.8b**.

## 4.5 Discussion

The presented model describes the contribution of Coulomb interactions between different atoms to the nonlinear response of dielectric nanostructures. To focus on the universal collective nonlinear response of any dielectric, we purposefully remove all possible atom-specific nonlinearities by describing atoms with the harmonic potential of a classical Lorentz oscillator model (and pumping far away from resonance). However, real atoms can be nonlinear. Considering the inversion symmetry of atoms in the ground-state, opposite directions of electron displacement yield opposite restoring forces. Therefore, the simplest approximation of a nonlinear atom would involve a symmetric anharmonic potential. Within this approximation, an individual atom can only have odd orders of optical response, i.e. contribute to 3<sup>rd</sup>, 5<sup>th</sup>, ... order nonlinearity. With respect to the particle's electric dipole, such atomic nonlinearity would contribute to the odd-order components that are parallel to the excitation field. This atomic contribution to a particle's odd order nonlinear dipole moment will be proportional to the particle's number of atoms, just like the contribution from Coulomb interactions between atoms.

Therefore, the atomic nonlinearity will affect the magnitude of the particle's odd order nonlinear electric dipole response parallel to the pump field, but not its qualitative behaviour. It has no bearing on the particle's even order nonlinearity, which arises entirely from interactions between atoms.

## 4.6 Summary

In summary, this chapter has shown that harmonic and sum frequency generation in 2D dielectric nanostructures can be modelled in terms of harmonic oscillators (atoms) coupled by the Coulomb force. This approach allows modelling of collections of atoms and mapping of the origin of harmonic and sum frequency generation in nanostructures. The results in this chapter indicate that:

## Chapter 4

- (1) Odd order harmonic and sum frequency generation has been found to originate from the whole structure with corresponding electric dipole moments scaling with the number of atoms.
- (2) Even order harmonic and sum frequency generation has been traced to the boundaries of 2D nanostructures, with corresponding electric dipole moments scaling with the structure's perimeter.
- (3) Multipoles may support harmonics which are forbidden in electric dipole approximation, but do not contribute to radiation in the direction normal to the 2D nanostructure.

The model allows the design and optimization of nonlinear dielectric nanostructures for nanophotonics, such as structures and particles cut from 2D materials and dielectric layers that are thin compared to the pump wavelength. 3D geometries may also be considered by solving the model in three dimensions.



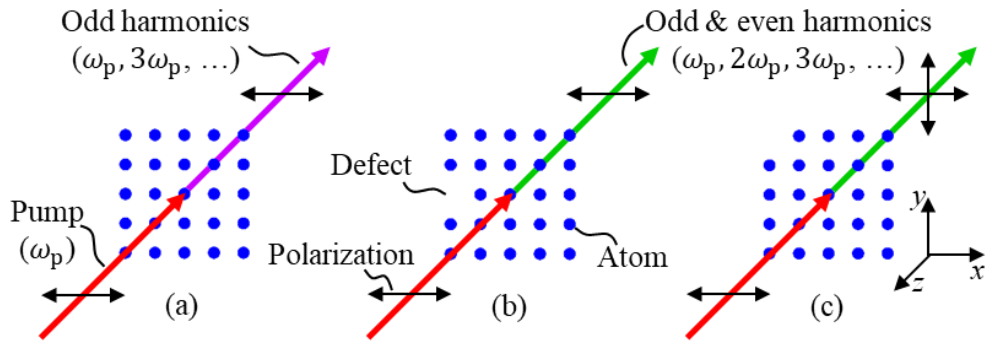
# Chapter 5 Model for defects induced nonlinearity in 2D nanostructures

## 5.1 Introduction

Previous chapters have shown how a structure's symmetry affects its nonlinearity, especially even order nonlinearity, which is forbidden in structures with even-fold rotational symmetries under normal excitation and collection. However, defects can break inversion centres and enable even order harmonic generation in structures of even-fold rotational symmetries. Harmonic generation as well as wave mixing in nonlinear photonic crystals with defects have attracted attention [122-125] and defect-enhanced second harmonic generation has been observed in various materials, including crystals [126, 127], 2D materials [128], doped fibres [129], semiconductors [130], their superlattices [131, 132] and interfaces [133, 134]. Recent progress in nanoparticle decoration [135, 136], micromachining [137, 138], lateral heterostructures [139, 140] and heterocrystals [141] has demonstrated the feasibility of defect manipulation and postprocessing techniques [142], which provides an opportunity for the development of two-dimensional (2D) materials with engineered optical nonlinearity [143]. In addition, second harmonic generation has been used for monitoring of defects engineering in transition metal dichalcogenides [142] and controlling nonlinear properties through defect engineering has been reported [144, 145]. Effects of vacancy defect concentration on high-order harmonic generation have also been investigated [146-148].

In this chapter, a model of defect induced harmonic generation in 2D nanoparticles described as a lattice of linear oscillators coupled by Coulomb interactions is presented. The model can pinpoint how each single defect influences the material's optical performance without solving full wave equations. The model shows how defects affect even and odd order optical nonlinearities. **Figure 5.1** shows an example. Along the optical axis, a square particle will only generate odd harmonics without polarization change, while the presence of defects can enable even harmonic generation without and with polarization change. The results indicate that defects at particle edges have the largest influence on optical nonlinearity. Different nonlinear optical responses of different defect distributions indicate that information could – in principle – be encoded in atomic defects and read optically, via their harmonic generation signature, which can be treated as a nonlinear QR code. The fundamental information density limit of such optical data storage would not be determined by diffraction, but rather by the spacing of atoms. We illustrate this by showing that harmonic generation is controlled by the location of defects in a square particle and by demonstrating

harmonic-based character recognition. Such information could be written by AFM-based techniques and read by scanning near-field microscopy techniques.



**Figure 5.1 Defect-induced optical nonlinearity**

(a) Along the optical axis, as shown, a square particle will only generate odd harmonics without polarization change. The presence of defects enables even harmonic generation (b) without and (c) with polarization change.

The details of the model are explained in **Section 5.2**. Then defect induced nonlinearity in a square nanoparticle (D4 symmetry) is analysed in **Section 5.3** and the effects of defect position are shown in **Section 5.4**. To cover a wider range of even fold rotational symmetry, the defect induced nonlinearity in a hexagonal nanoparticle (D6 symmetry) is discussed in **Section 5.5**. More importantly, **Section 5.6** shows how information could be encoded in atomic defects and read via their harmonic generation signature.

## 5.2 Modelling defect-induced optical nonlinearity of 2D nanoparticles

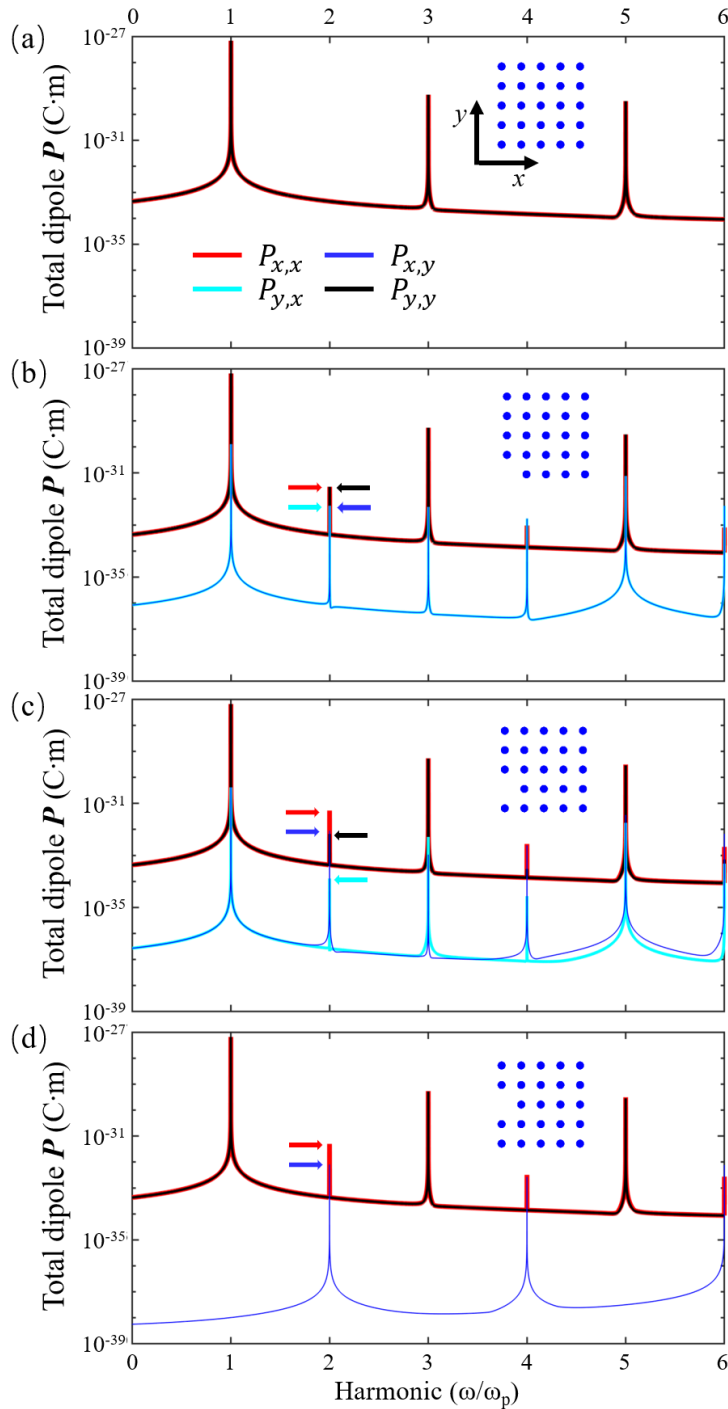
We consider the radiation generated along  $z$  by 2D structures in the  $xy$ -plane (nanoparticle plane) in response to pumping along  $z$ , to mimic the structure’s nonlinear optical response along the propagation direction for pumping at normal incidence. In this case, radiation generated by the particle is determined only by its total electric dipole moment. Higher multiples cannot contribute to the radiation along the  $z$  direction as discussed in **Chapter 4**. The displacement of each optical electron in the particle is calculated in the time domain by solving their coupled equations of motion (details in **Chapter 2**). We consider a square particle cut from a square lattice and a hexagon particle cut from a hexagonal lattice, introducing defects by removing atoms at designed positions in the lattice. The coupled system of differential equations is solved in Matlab starting without optical electron displacement and allowing transitional effects to pass before analysing the oscillation of all electrons over 1000 periods of the driving field. The electric dipole moment of each atom  $\mathbf{d}_k$  is the charge times the electron displacement. The total electric dipole of the particle is the sum of these dipoles over all atoms,  $\mathbf{P} = \sum_k \mathbf{d}_k$ . This gives the total electric dipole moment  $\mathbf{P}(t)$  of the

nanostructure in the time domain. The total electric dipole moment is separated into linear and nonlinear components,  $\mathbf{P}^{(1)}, \mathbf{P}^{(2)}, \mathbf{P}^{(3)} \dots$ , oscillating at the driving frequency  $\omega_p$  and its harmonics  $2\omega_p, 3\omega_p \dots$ , through Fourier transformation (see **Section 2.4**). In the presented Fourier series, the peak values are the dipole amplitudes in Coulomb meters at harmonic frequencies.

### 5.3 Defect induced nonlinearity in a square nanoparticle

Since radiation of even order harmonics along  $z$  is forbidden in structures with even-fold rotational symmetry [84, 102], one can easily identify the defect induced nonlinearity of such structures at even harmonics. Therefore, this section first studies a square particle with 25 atoms (D4 symmetry, with square lattice) and then introduces one vacancy defect at three different positions. As examples, we have chosen the possible types of edge defects – at a corner, middle or intermediate edge position – which result in different symmetries of the particle. **Figure 5.2a** illustrates harmonic generation in the square particle. The frequency-dependence of the total electric dipole moment  $\mathbf{P}$  generated by electric pump field  $E_0 \cos(\omega_p t)$  is shown, where  $P_{\alpha, \beta}$  refers to the  $\alpha$ -component of the dipole moment caused by a  $\beta$ -polarized pump field and  $\alpha, \beta$  is  $x$  or  $y$ . As required by symmetry,  $x$ -polarized excitation generates a dipole only along  $x$ , while  $y$ -polarized excitation generates a dipole only along  $y$  with the same magnitude. i.e.  $P_{x,x} = P_{y,y}$ , while  $P_{x,y}$  and  $P_{y,x}$  are forbidden. As expected for a particle with even-fold rotational symmetry [84, 102], we observe only odd harmonics –  $\mathbf{P}^{(1)}, \mathbf{P}^{(3)}, \mathbf{P}^{(5)}$  – which appear as peaks in **Figure 5.2a**. However, when there is a vacancy defect in the particle, even harmonics can occur, as shown by **Figure 5.2(b-d)**.

The defect position has a great impact on the particle's nonlinear response. When defect occurs at a corner (**Figure 5.2b**),  $x$  or  $y$ -polarized excitation generates dipole moments along both the  $x$  and  $y$  directions, and we observe  $P_{x,x} = P_{y,y}$  and  $P_{x,y} = P_{y,x}$ . When the defect occurs in between a corner and the middle of an edge (**Figure 5.2c**), the four components  $P_{x,x}, P_{y,y}, P_{x,y}$  and  $P_{y,x}$  are all allowed and different. For a defect in the middle of an edge (**Figure. 5.2d**), only  $P_{x,x}, P_{y,y}$  and one of  $P_{x,y}$  and  $P_{y,x}$  are allowed.

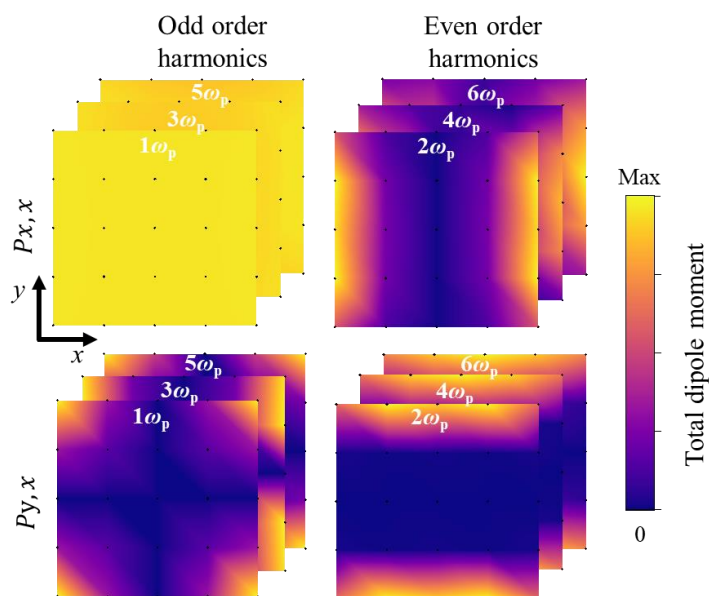


**Figure 5.2 Harmonic generation in a square nanoparticle without and with defects**

(a)-(d) Frequency dependence of the electric dipole moment of a square particle (insert) with no defect (a), and (b-d) one defect at three different locations, in response to optical pumping at frequency  $\omega_p$ .  $P_{\alpha,\beta}$  indicates the  $\alpha$ -component of the particle's electric dipole moment caused by  $\beta$ -polarized pumping. Arrows indicate the magnitudes of  $P_{x,x}$ ,  $P_{y,y}$ ,  $P_{x,y}$  and  $P_{y,x}$  at second harmonic frequency.

## 5.4 Effects of defect position

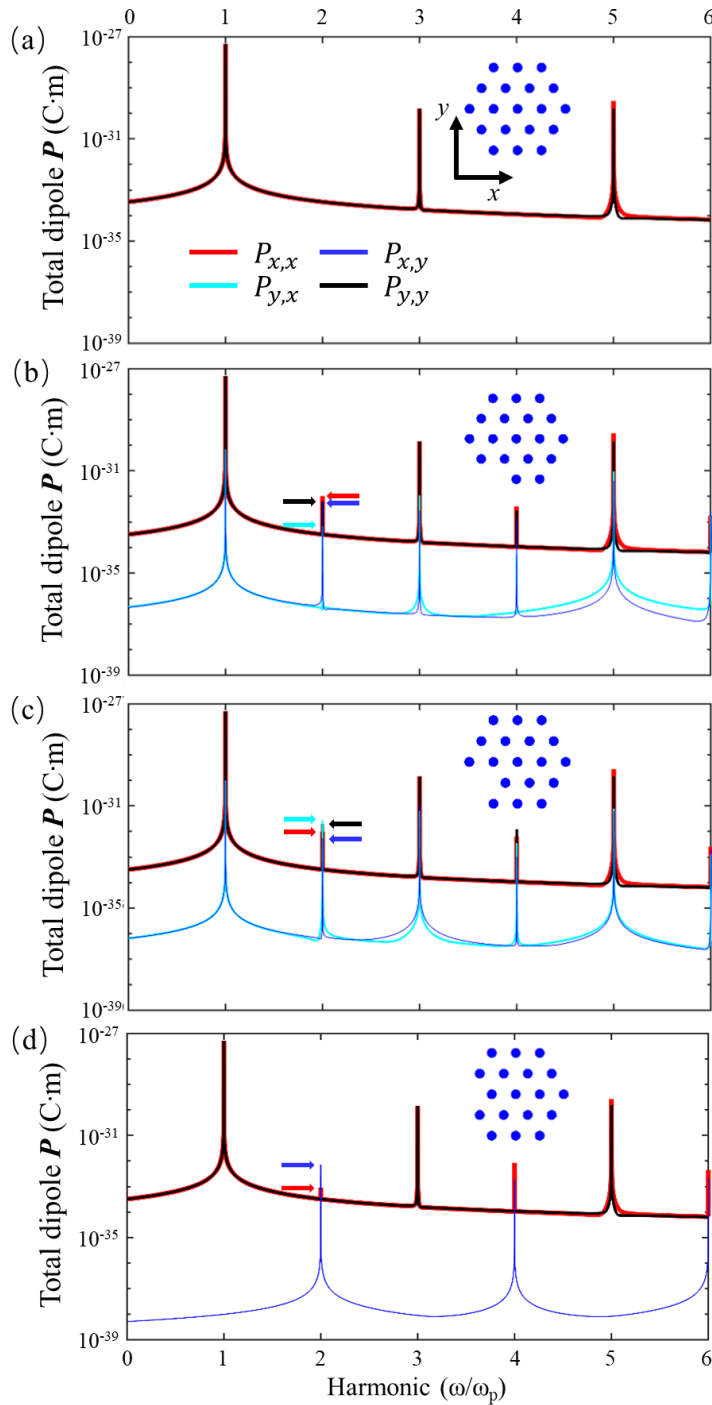
The importance of the defect position was revealed by **Figure 5.2**. Here the dependence of optical nonlinearity on the defect position is investigated systematically. **Figure 5.3** shows the calculated components of the total electric dipole moment  $\mathbf{P}$  as a function of the position of a single defect. The top row shows the total electric dipole moment along the  $x$ -direction for  $x$ -polarized pumping,  $P_{x,x}$  at odd (left) and even (right) harmonic frequencies. At odd harmonic frequencies,  $P_{x,x}$  is of almost the same magnitude for all the 25 defect positions. In contrast,  $P_{x,x}$  at even harmonic frequencies depends strongly on the defect's location, being strongest for defects on the left and right edges and vanishing only for defects that do not break the  $y$  symmetry axis of the nanoparticle. The bottom row shows the total dipole moment along the  $y$ -direction for  $x$ -polarized pumping,  $P_{y,x}$  at odd (left) and even (right) harmonic frequencies. At odd harmonics, defects at corners induce the strongest dipole moment  $P_{y,x}$ , while this component does not arise from defects that maintain the horizontal or vertical mirror symmetry of the nanoparticle. In contrast, for even harmonics the total electric dipole  $P_{y,x}$  is strongest for defects at top and bottom edges and vanishes only for defects that do not break the nanoparticle's  $x$  symmetry axis. Similar behaviour is seen for hexagonal particles (see **Section 5.5**).



**Figure 5.3** Total electric dipole moment as a function of the position of a single vacancy defect

The amplitude at each atom position (black dot) represents the total dipole moment of the particle when the atom is vacant. In the square particle, we can have 25 different defect positions. The top (bottom) row shows the dipole component parallel (orthogonal) to the  $x$ -polarized pump. Stacked images for different – either even or odd – harmonics show the same qualitative behaviour. ( $P_{y,y}$  and  $P_{x,y}$  are obtained by  $90^\circ$  rotation of the color maps in the top and bottom rows, respectively.)

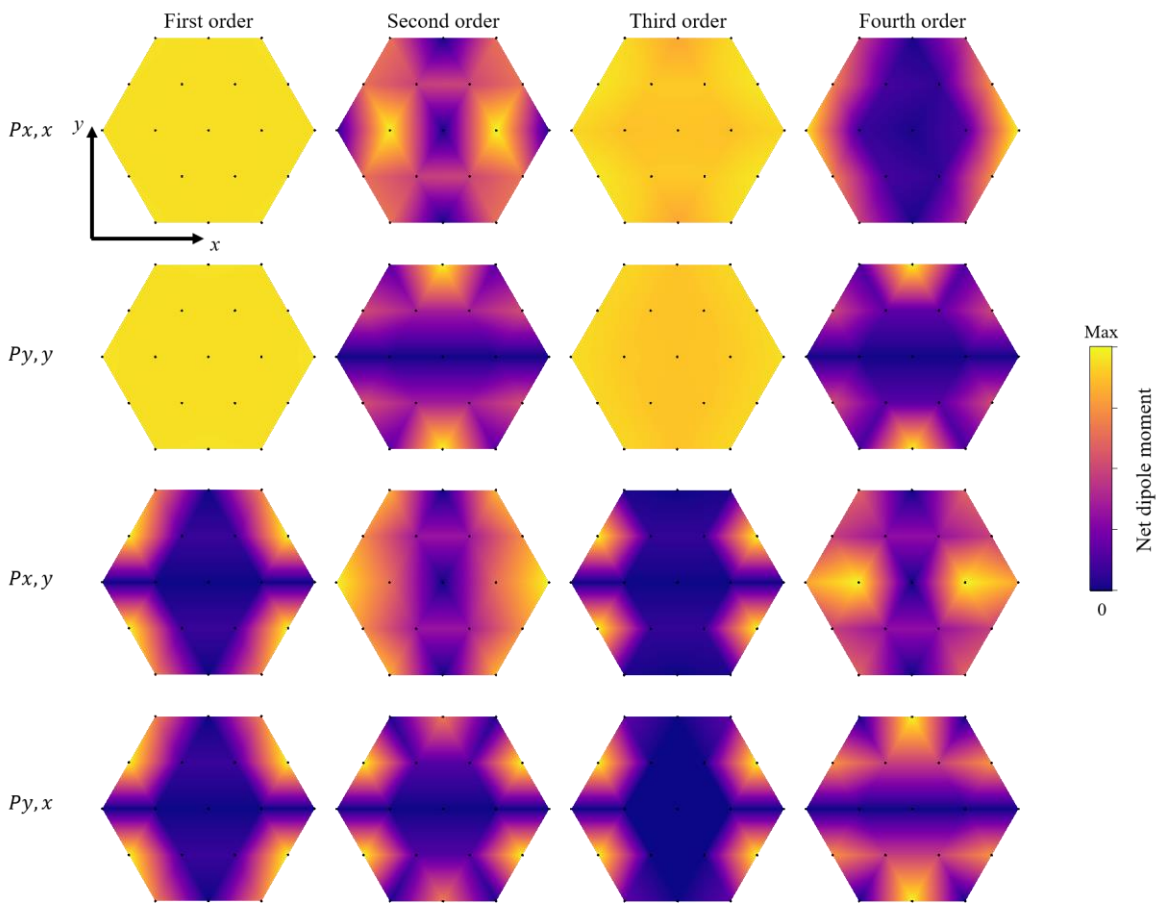
### 5.5 Defect induced nonlinearity in a hexagonal nanoparticle



**Figure 5.4 Harmonic generation in a hexagon nanoparticle without and with single defects**  
 Harmonic generation in a hexagonal nanoparticle (a) without and (b-d) with single defects in different positions of the hexagonal atomic lattice of D6 symmetry (insets). Frequency dependence of the electric dipole moment of the particles in response to optical pumping at frequency  $\omega_p$ .  $P_{\alpha,\beta}$  indicates the  $\alpha$ -component of the particle's electric dipole moment caused by  $\beta$ -polarized pumping at normal incidence. The arrows mark the magnitudes of  $P_{x,x}$ ,  $P_{y,y}$ ,  $P_{x,y}$  and  $P_{y,x}$  at the SH frequency.

To cover a wider range of even fold rotational symmetry, the influence of vacancy defects on harmonic generation by a hexagonal nanoparticle with 19 atoms (D6 symmetry, hexagonal lattice) is also analysed, shown by **Figure 5.4**. Electric dipole moments at even order harmonics are forbidden in the hexagonal particle without defects (**Figure 5.4a**), but emerge when a single vacancy defects breaks the symmetry of the particle (**Figure 5.4b-d**). The amplitudes of the electric dipole components excited by  $x$  and  $y$  polarized pumping depend on the defect position.

This dependence on the defect position is shown by **Figure 5.5**. Owing to the complete particle's symmetry, that includes mirror symmetry along  $x$  and  $y$ , the distributions of total electric dipole moment as a function of defect position are mirror-symmetric along  $x$  and  $y$ . Electric dipole moments at odd harmonics,  $P_{x,x}^{(1)}$ ,  $P_{y,y}^{(1)}$ ,  $P_{x,x}^{(3)}$ ,  $P_{y,y}^{(3)}$ , ..., which can be excited without defects (**Figure 5.4a**), do not depend strongly on the defect position. All other electric dipole components in **Figure 5.5** are forbidden in the complete particle and therefore depend strongly on the presence of defects in locations that affect the symmetry of the nanoparticle. Like for the square particle, pumping with  $x$  and  $y$  polarizations yields similar distributions of *odd-order* total electric dipole moment as a function of vacancy defect position. In contrast, due to lack of four-fold rotational symmetry of the hexagonal particle and its lattice, pumping with  $x$  and  $y$  polarizations yields distinctively different distributions of *even-order* total electric dipole moment as a function of defect position.



**Figure 5.5 Total electric dipole moment  $P$  as a function of defect position**

The amplitude at each atom (black dot) represents the total dipole moment when that atom is vacant. In the hexagonal particle, there are 19 possible defect positions. The four components of the particle's total electric dipole (rows) are shown for the first to fourth order harmonics (columns).

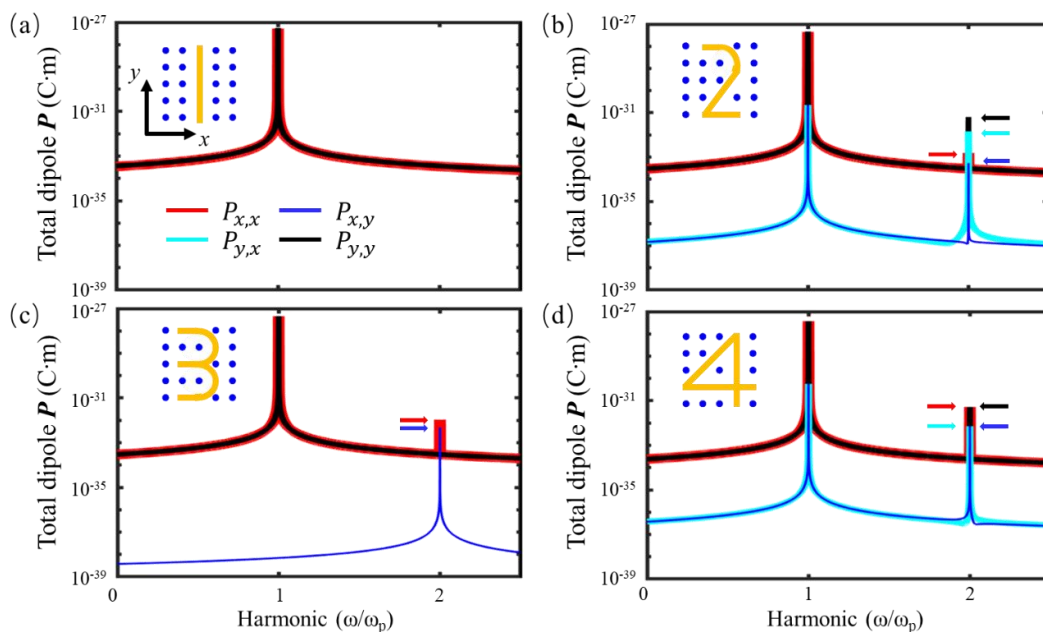
## 5.6 Nonlinear QR codes

The recent progress of 2D material fabrication demonstrates the feasibility of defect manipulation and postprocessing techniques. SHG has already been used for defect engineering monitoring in transition metal dichalcogenides. Our model is a suitable tool for instructing defect engineering. We argue that 2D defect patterns could act as 2D bar codes, i.e. QR codes, that could be read based on their nonlinear optical properties. **Figure 5.6** shows the frequency dependence of the total electric dipole moment of four defect patterns – “1, 2, 3, 4” – in a square lattice in response to a pump field  $E_0 \cos(\omega_p t)$ . We can identify each of them by looking into their second harmonic generation.

Defect pattern “1” does not generate a total electric dipole moment at the second harmonic frequency (**Figure 5.6a**), while for pattern “3” (**Figure 5.6c**) only the electric dipoles along x can be



generated at the second harmonic frequency. Although all four electric dipole components are allowed for defect patterns “2” and “4” (**Figure 5.6b,d**), components of equal amplitudes  $P_{x,x}=P_{y,y}$  and  $P_{x,y}=P_{y,x}$  are only observed for pattern “4”. Thus, the relative strength of the second harmonic total electric dipole components can be used to identify different defect patterns. We note that other polarizations and harmonics could also be considered. In general, both the number and position of defects affect a particle’s total electric dipole response. Indeed, odd harmonic total electric dipole moments ( $P_{x,x}$ ,  $P_{y,y}$ ) scale with the number of atoms, and could thus be used to reveal the number of occupied atom positions.



**Figure 5.6 Harmonic generation in a square nanoparticle with atomic defect patterns**

(a)-(d) Frequency dependence of the electric dipole moment of a square particle (insert) with defect patterns (a) “1”, (b) “2”, (c) “3”, (d) “4” in response to optical pumping at frequency  $\omega_p$ .  $P_{\alpha,\beta}$  indicates the  $\alpha$ -component of the particle’s electric dipole moment caused by  $\beta$ -polarized pumping.

In principle, a square lattice containing  $N$  atom positions can have  $2^N$  different defect states. Mirror symmetry with respect to  $x$  and  $y$  in **Figure 5.3** implies that up to four different defect states – that are related by reflections with respect to  $x$ ,  $y$ , or both – share the same nonlinear signature. (Fewer in case of defect states that have one or more relevant mirror symmetries.) Therefore,  $>2^{N-2}$  defect states may have distinguishable nonlinear signatures, suggesting that nonlinear detection of defect states could enable extremely high density optical data storage, in principle approaching 1 bit per atom. Arguably, such defect patterns would be the ultimate miniaturization of QR codes.

## 5.7 Summary

Optical nonlinearity depends on symmetry and symmetries vanish in the presence of defects. The emerging ability to manipulate defects in two-dimensional materials and nanoparticles provides an opportunity for engineering of optical nonlinearity. In this chapter, a model of defect induced harmonic generation in 2D nanoparticles described as a lattice of linear oscillators coupled by Coulomb interactions has been presented. The results in this chapter indicate that:

- (1) Defects have a large influence on even harmonic generation in 2D nanostructures. The presence of defects can enable even harmonic generation without and with polarization change which is not allowed in structures with even-fold rotational symmetry, such as square of D4 symmetry and hexagon of D6 symmetry.
- (2) Defects at particle edges have the largest influence on optical nonlinearity, i.e. contribute strongly to even-order optical nonlinearity.
- (3) Information could be encoded in atomic defects via defect engineering and read by its harmonic generation signature. Arguably, such nonlinear QR codes would be the ultimate miniaturization of 2D bar codes. This has been illustrated by showing that harmonic generation is controlled by the location of defects in square and hexagonal particles and by demonstrating harmonic-based character recognition.

The nonlinear QR codes in 2D nanostructures could be written by AFM-based techniques and read by scanning near-field microscopy techniques. The unique nonlinear signatures of different defect states could provide extremely high-density optical data storage, in principle approaching 1 bit per atom.

In parallel with modelling of second harmonic generation in nanostructures in **Chapter 2 to 5**, I designed a metamaterial for second harmonic generation. At that stage, simplicity of fabrication and resonant optical properties were key considerations, and therefore I chose a double-chevron structure as the meta-atom (more details in **Chapter 6**). With the development of the theoretical model, I found that a triangular shape offers several good features, for example, the SHG strength of a triangular structure is insensitive to the pump polarization and a triangular shape could have higher nonlinearity than chevron structures. Therefore, I optimized my design for high SH conversion efficiency and fabricated a new metamaterial of triangular meta-atoms (details in **Chapter 8** and **Appendix B**).

## Chapter 6 Design and fabrication of nonlinear fibre-integrated all-dielectric metasurface

### 6.1 Introduction

Nonlinear optics is crucial in many photonic applications. Efficient even-order nonlinear effects typically require thick non-centrosymmetric crystals with a strictly controlled orientation of the crystalline axes. These rigid requirements hamper the potential for miniaturization of photonic devices, which in turn limits the speed, efficiency and scalability of photonic technology. Recent progress in the field of metamaterials promises to revolutionize nonlinear optics, by providing a way to achieve desired nonlinear responses through design. Photonic two-dimensional metamaterials, often referred to as metasurfaces, could offer an alternative to traditional bulk nonlinear optics. Despite that, little effort has so far been dedicated to developing nonlinear photonic metamaterials on platforms suited for integration with waveguides.

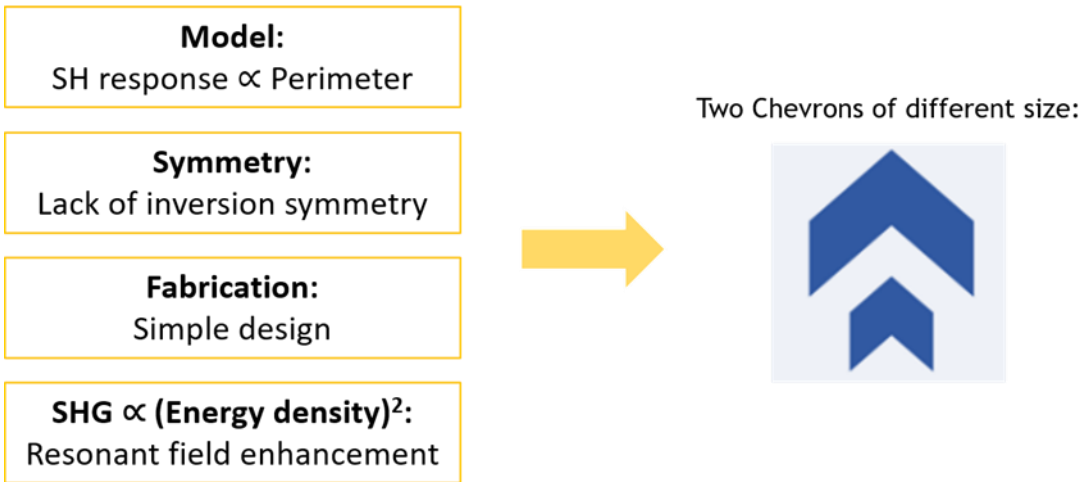
To demonstrate nanostructure induced second harmonic generation, a fibre-integrated all-dielectric nonlinear metasurface has been designed (**details in Section 6.2**) and fabricated (**details in Section 6.3**). The structure exhibits a resonance at about 1.5  $\mu\text{m}$  with a quality factor of 30 (**details in Section 6.4**). The metasurface will be used to demonstrate second harmonic generation in **Chapter 7**.

### 6.2 Design of fibre-integrated all-dielectric metasurface

When designing the fibre integrated metasurface for second harmonic generation, several factors needed to be considered, see **Figure 6.1**. According to the results in **Chapter 3** and **Chapter 4**, second harmonic generation by centrosymmetric materials is associated with boundaries, implying that a structure with reasonably long boundaries is desirable.

Also, according to the analysis of symmetry-allowed components of the second order susceptibility  $\chi^{(2)}$  tensor in **Chapter 1**, only the C1, D1, C3 and D3 point symmetry groups (no rotational symmetry or 3-fold rotational symmetry) have non-vanishing  $\chi^{(2)}$  tensors. Compared to C1, C3 and D3 symmetry groups, a chevron (D1 Symmetry)– two identical lines forming an angle – is arguably the simplest structure lacking an inversion centre, and chevrons can be easily fabricated and combined into a compact unit cell that is smaller than its resonant wavelength. In addition, the point symmetry group of D1 limits the allowed components of the second-order nonlinear

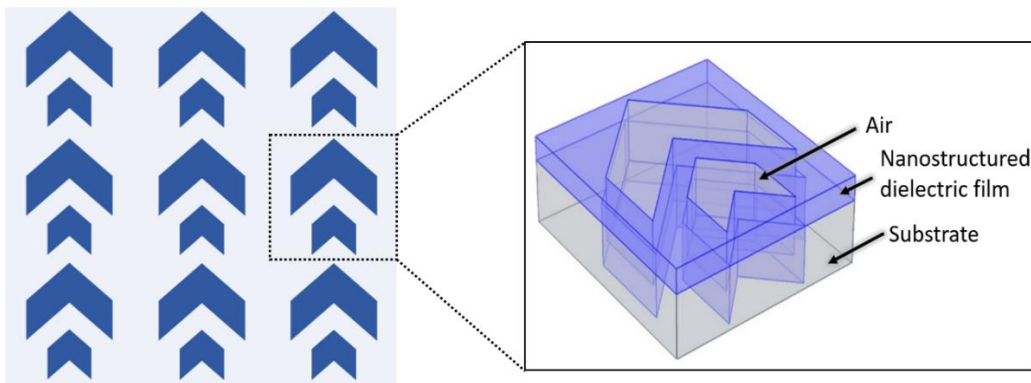
susceptibility tensor to:  $\chi_{yyy}^{(2)}, \chi_{yxx}^{(2)}, \chi_{xxy}^{(2)} = \chi_{xyx}^{(2)}$ , where the first index indicates the polarization of the second harmonic wave and the other indices indicate the polarizations of the pump wave.



**Figure 6.1 Nanostructure design criteria for second harmonic generation**

A unit cell of two chevrons is selected since it ① has a relatively long boundary, ② has D1 symmetry which supports second order nonlinearity, ③ is easily fabricated and ④ supports Fano resonances.

Since the second harmonic strength is proportional to the square of energy density, the structure should support resonances for higher conversion efficiency. In principle, resonances can help enhance the local field at the fundamental frequency as well as second harmonic frequency [62]. From these considerations, two chevrons of different size are chosen as the unit cell of the nonlinear metasurface, see **Figure 6.1**.

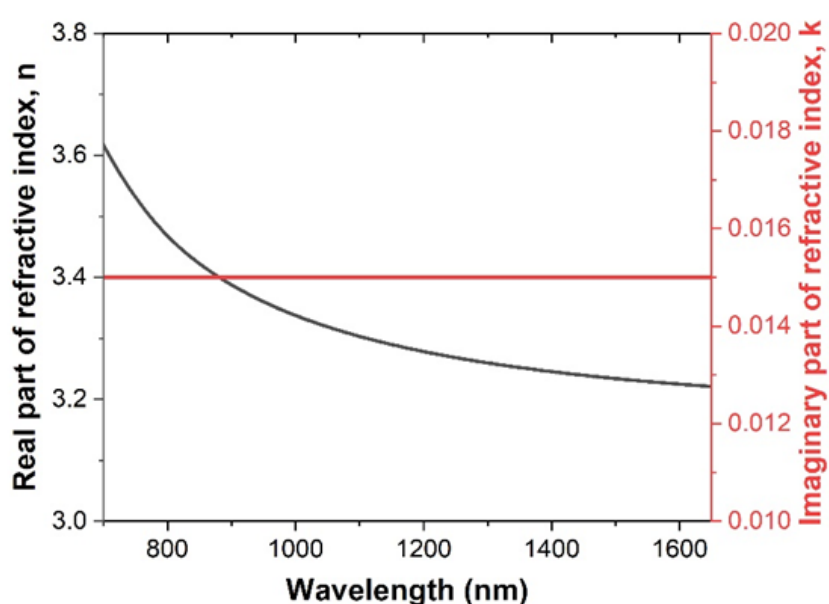


**Figure 6.2 Schematic of the metasurface fabricated from centrosymmetric dielectric**

The metasurface consists of an array of chevron groove pairs. The figure on the right is the unit cell of this metasurface. The blue area corresponds to the dielectric film (amorphous silicon), and the gray area corresponds to the substrate (silica).

Aiming for a Fano resonance within the technologically important telecommunications band around  $1.5\ \mu\text{m}$  wavelength, I designed a metamaterial, which is an array of chevron groove pairs, with unit cell dimensions of  $1.1 \times 1.0\ \mu\text{m}^2$ , milled into the core of a silica fibre and subsequently coated with a 90-nm-thick amorphous silicon layer, see **Figure 6.2**.

Silicon film is chosen because it has a relatively high refractive index and low loss at the telecommunication wavelength band (shown in **Figure 6.3**), which enables high quality factor resonances. Also, compared with metallic structures such as gold and silver, silicon has a higher damage threshold, and can therefore withstand higher pump laser intensity. Moreover, silicon is highly compatible with the optical fibre and semiconductor fabrication ecosystem, which enables developing integrated nonlinear photonic devices.

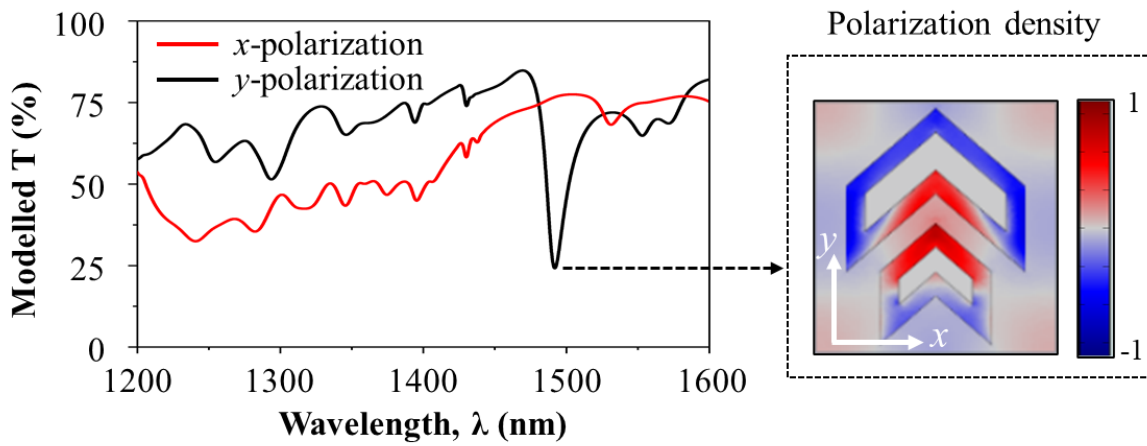


**Figure 6.3** Refractive index of the fabricated amorphous silicon thin film

The data is measured by ellipsometry of 90-nm thick amorphous silicon film (deposited in the same settings as the silicon of the metamaterial sample). The loss of the silicon film remains at a low level ( $k=0.015$ ) from 750 nm (second harmonic wavelength) to 1500 nm (our fundamental wavelength).

The sizes of the two chevrons contained in the unit cell are designed to be slightly different in order to excite a resonance with high quality factor at the pump wavelength [59-61]. The metamaterial's transmission spectra were modelled using **Comsol Multiphysics 5.4**, assuming a plane wave normally incident onto a unit cell with periodic boundary conditions (**Figure 6.4**). The simulations assume a real refractive index of 1.44 for glass and the complex refractive index of the silicon layer according to ellipsometry measurements are shown in **Figure 6.3**.

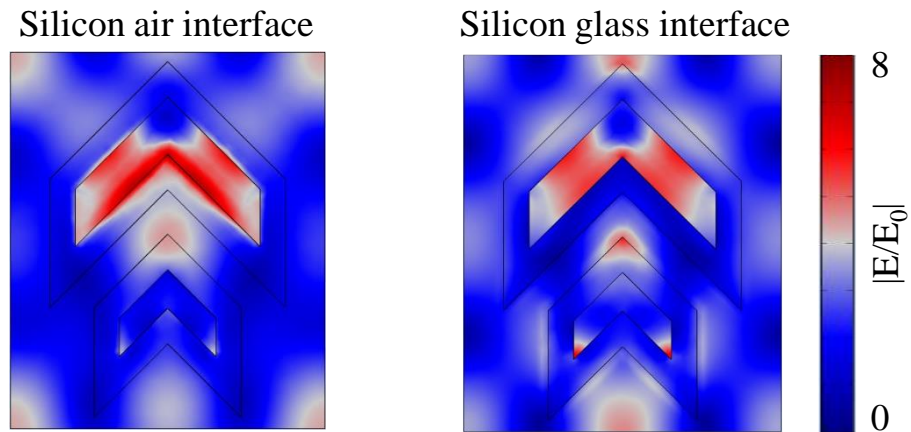
By adjusting the parameters of the asymmetric nanostructure, such as depth and the space between the two grooves, resonances of the metamaterial can be engineered. **Figure 6.4** shows the simulated transmission spectra and the field map at the resonance of the designed metamaterial. A closed-mode resonance is seen at a wavelength of 1.5  $\mu\text{m}$ , only under y-polarized illumination (along the symmetry axis). No clear resonance is observed when the metamaterial is illuminated with the orthogonal polarization.



**Figure 6.4 Simulated transmission spectra and field map of chevron groove pairs**  
 Modelled linear transmission spectra of the metamaterial as a function of wavelength for x (red) and y (black) polarization. The colormap shows the y component of the linear polarization density distribution at the resonance.

Since one unit cell contains a deep/wide chevron groove and a shallow/narrow chevron groove, the size difference contributes to different field distributions in the two grooves, see the colormap in **Figure 6.4**. The colormap shows the polarization density along the symmetry axis at the closed mode resonance. In the colormap, we see that charges in the two chevrons are oscillating in anti-phase which will trap the energy within the nanostructure. The slightly different size helps couple the field to free space. In our case, the closed mode increased the local field at the fundamental frequency, which, in turn, shall boost the SHG efficiency.

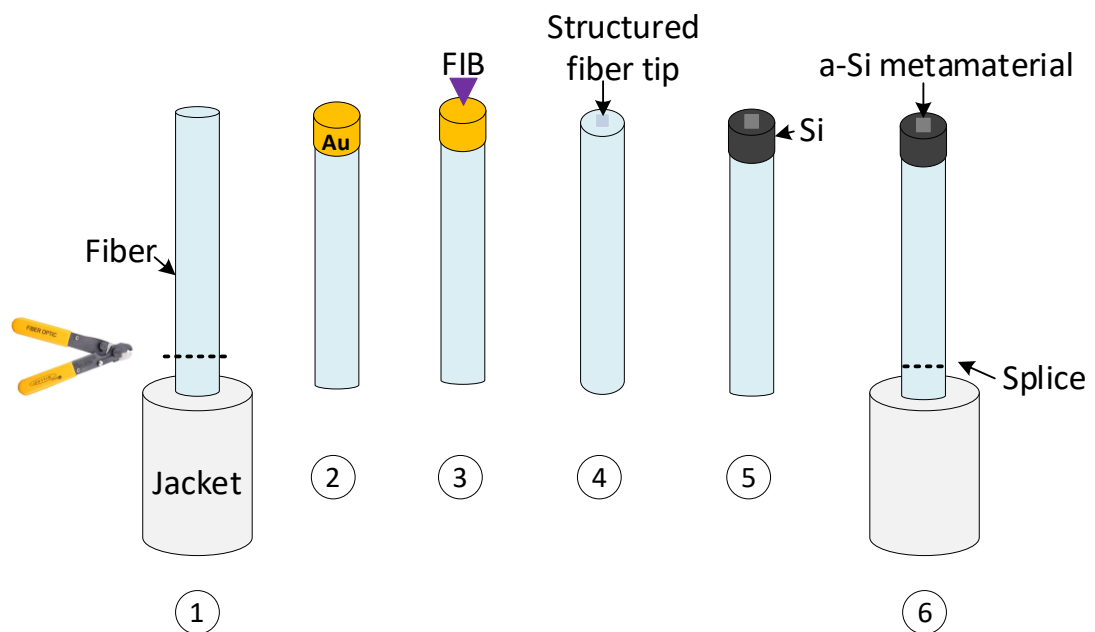
According to the simulations, the electric field at the silicon interfaces is up to 8× larger than the incident field, see **Figure 6.5**.



**Figure 6.5 Electric field enhancement at the silicon interfaces**

Field enhancement is shown relative to the amplitude  $|E_0|$  of the incident wave, for the case of a normally incident  $y$ -polarized wave at the  $1.5 \mu\text{m}$  wavelength resonance.

### 6.3 Fabrication of fibre-integrated all-dielectric metasurface

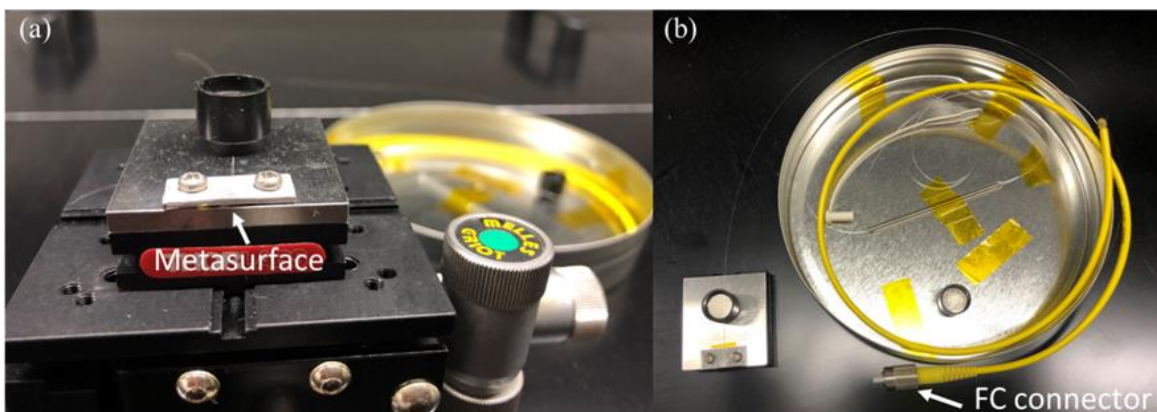


**Figure 6.6 Fabrication process diagram**

During fabrication, to reduce gallium deposits, the fibre tip is first coated with a thin layer of gold and then the V-shaped grooves are created by milling with a focused gallium ion beam through the gold layer to the depth of about  $256 \text{ nm}$  into silica. After removing the sacrificial gold layer through a wet etching process, a  $90\text{-nm}$  layer of amorphous silicon is deposited by PECVD on the entire patterned fibre tip.

The metamaterial structure was fabricated on the tip of an optical fibre. The fabrication process diagram is shown in **Figure 6.6**.

- ① The fabrication of amorphous silicon metamaterial on a fibre tip [149] is carried out by stripping a segment of single-mode silica fibre (Thorlabs SM980-5.8-125) of its protective polymer jacket, leaving a few centimeter long bare silica rod (125  $\mu\text{m}$  in diameter), to avoid the protective polymer jacket melting and destroying the metamaterial at high temperatures during the deposition processes (i.e. 200°C in PECVD process). One end of the fibre is then cleaved to create a smooth end-facet that will serve as the metamaterial’s substrate.
- ② The next step is followed by coating the cleaved fibre tip with a 50 nm thick sacrificial layer of gold using an e-beam evaporator. The sacrificial layer is introduced to reduce gallium deposits [61].
- ③ The centre (core area) of the gold-coated fibre tip is then patterned through the sacrificial layer to the depth of about 256 nm into silica using focused ion beam milling (FIB), see **Figure 6.8d**.
- ④ Following patterning, the metal layer is removed using gold etchants, leaving a nanostructured silica fibre tip. The injected gallium ions are mainly in the gold layer. After removing the gold film, only a small amount of gallium contamination in the patterned silica fibre tip remains.
- ⑤ Then, a 90-nm layer of amorphous silicon is deposited onto the entire patterned fibre tip using plasma enhanced chemical vapour deposition (PECVD).
- ⑥ Finally, the bare fibre segment is spliced to a single-mode fibre with a FC connector.



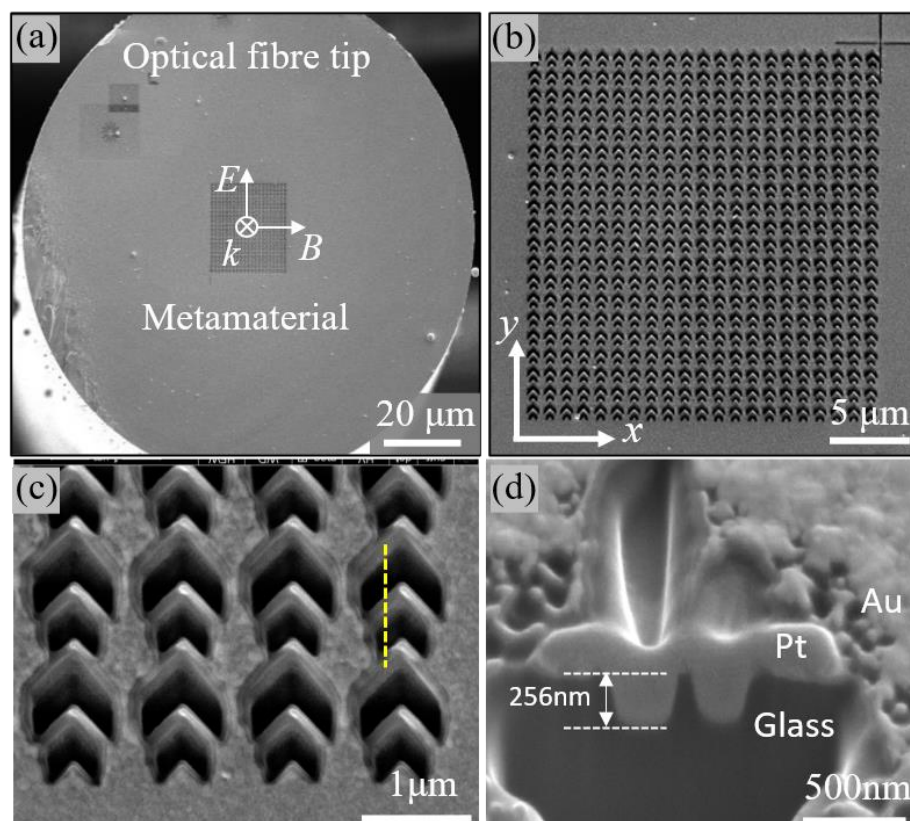
**Figure 6.7 Nonlinear silicon metamaterial on a fibre tip**

(a)-(b) Images of the nonlinear silicon metamaterial mounted on a fibre holder.

The fabricated metamaterial is then mounted in a fibre holder (Thorlabs HFV001). To avoid drifting, the fibre is clamped to the fibre holder using a metal plate, shown in **Figure 6.7a**. The spliced FC connector is used to directly collect and guide light transmitted or radiated by the metamaterial.



The SEM images of the metamaterial are shown in **Figure 6.8**. The size of the patterned area is  $20 \times 21 \mu\text{m}^2$ , covering the entire core of the fibre, which has a nominal diameter of  $10 \mu\text{m}$ , see **Figure 6.8a-b**. The structure is patterned to the depth of about  $256 \text{ nm}$  into silica substrate, see **Figure 6.8d**. Therefore, the metamaterial's thickness, from the lowest point of the  $90 \text{ nm}$  thick silicon layer at the bottom of the chevron grooves to its highest point at the silicon/air interface in between the chevron pairs, is  $L=346 \text{ nm}$ .



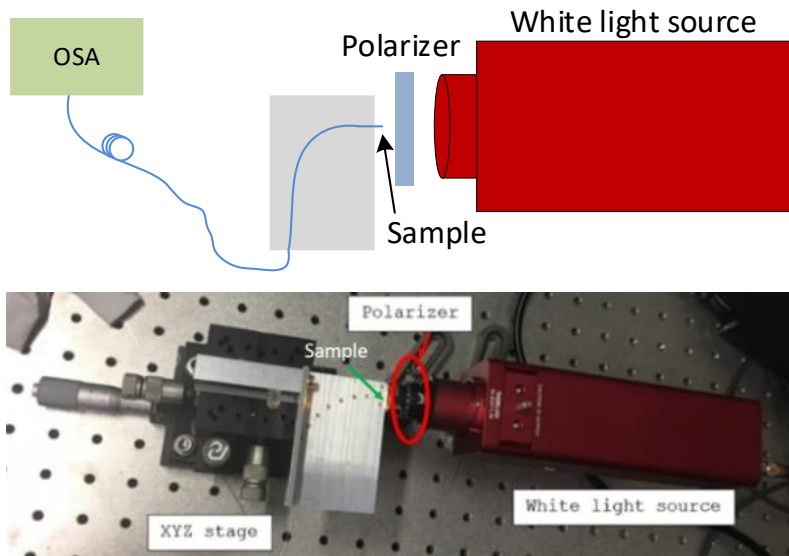
**Figure 6.8** SEM images of nonlinear silicon metamaterial on a fibre tip

(a) SEM image of the nonlinear metamaterial fabricated on the end-facet of a single-mode optical fibre. The metamaterial covers the core of a cleaved optical fibre and consists of pairs of chevron grooves in silica, coated with an amorphous silicon layer. (b) Magnified view of the entire metamaterial. (c) Magnified view of a metamaterial section. (d) Cross section of the nanostructure (i.e. along the yellow dashed line in c), showing the bottom layer of silica (glass) and an additional layer of platinum added for contrast (Pt). (To prevent charging, SEM imaging took place before the sacrificial gold coating was removed.)

#### 6.4 Linear optical property characterization

After the fabrication process, the transmission spectra of this sample were measured using the **ANDO AQ-6315E** optical spectrum analyser (OSA). The schematic and the experimental measurement setup are depicted in **Figure 6.9**. The structure's transmission spectra were

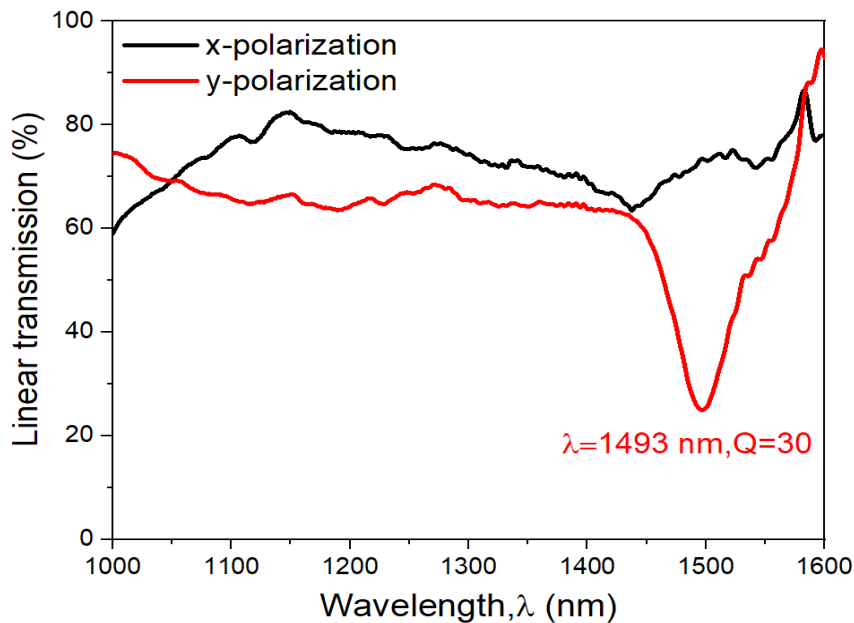
measured by illuminating the fibre tip with normally incident linearly polarized white light and detecting the transmitted light with the optical spectrum analyser, using an unstructured cleaved fibre without the silicon film as a reference.



**Figure 6.9 Experimental setup for transmission measurements**

Schematic and photo of the setup are shown.

The experimental transmission spectra of the sample for both x-polarized and y-polarized incident light are shown in **Figure 6.10**.



**Figure 6.10 Measured linear transmission spectrum of the metamaterial**

Metamaterial’s linear transmission as a function of the pump wavelength for x-polarization (black) and y-polarization (red).

The experimental spectra of the metamaterial are in qualitative agreement with the modelled transmission (**Figure 6.4**). Due to the size difference of the chevrons contained in each unit cell, the metamaterial exhibits an asymmetric resonance at about 1.5  $\mu\text{m}$  wavelength, when illuminated with light polarized along the chevron symmetry axis (y-axis in **Figure 6.8b**). However, no resonance is observed when the metamaterial is illuminated with the orthogonal polarization. The experimentally observed resonance at 1.5  $\mu\text{m}$  wavelength has a quality factor of  $Q=30$ , which is calculated by  $Q=\lambda_0/\Delta\lambda$ , where  $\lambda_0=1.5 \mu\text{m}$  is the resonance's central wavelength and  $\Delta\lambda$  is the resonance's full width at half maximum (FWHM).

Compared with the modelling, the measured resonance is wider due to fabrication-related residual contamination with gallium and inhomogeneous broadening (i.e. slight variations in sizes of key features across different unit cells).

## 6.5 Summary

In this chapter, a metamaterial for second harmonic generation has been designed and fabricated. The metamaterial is an array of chevron groove pairs integrated in a single mode fibre. The all-dielectric metamaterial supports a resonant response at wavelength  $\lambda_0=1.5 \mu\text{m}$  of quality factor  $Q=30$ . Based on its symmetry, it may support three allowed second-order nonlinear susceptibility tensors components:  $\chi_{yyy}^{(2)}, \chi_{yxx}^{(2)}, \chi_{xxy}^{(2)} = \chi_{xyx}^{(2)}$ .



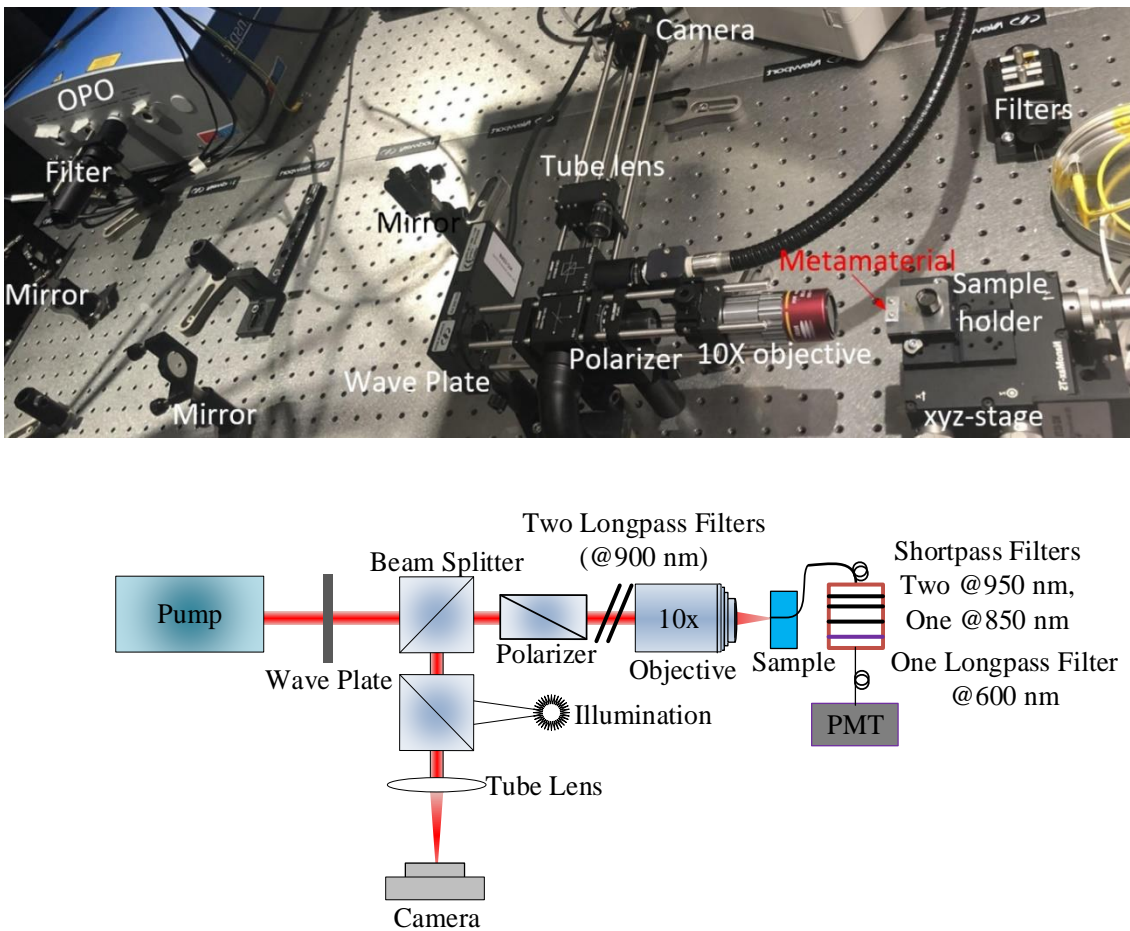
## Chapter 7 Second harmonic generation in a fibre integrated all-dielectric metasurface

### 7.1 Introduction

Second-order nonlinear optical processes are of considerable importance for laser technologies, quantum optics, materials characterization, spectroscopy and imaging. Over the last decade, a substantial effort has been focused on developing plasmonic [20, 22, 24, 26, 49, 150-152] and dielectric [48, 50, 93, 153] metamaterials [23] with large nonlinearities for second harmonic generation (SHG). In particular, in silicon-based photonics, second-order optical nonlinearities are required in various information processing schemes [29, 30]. In silicon, which is centrosymmetric, second-order optical nonlinearity can be imposed by strain, electric field and interfaces and has been observed in waveguides [154-160], nanoparticles [62], nanowires [161, 162], nanopillars [163], photonic crystal nanocavities [164], metamaterials [25, 165, 166] and multi-material stacks with silicon [167, 168]. Silicon metasurfaces have also been used to enhance the nonlinear response of materials with strong natural second-order nonlinearity [169, 170].

In this chapter, I will report second harmonic generation from the fibre-integrated metamaterial manufactured from amorphous silicon described in **Chapter 6** that achieves two orders of magnitude higher normalized conversion efficiency than prior state of the art [25]. First, the experimental setup for the second harmonic generation measurements is discussed in **Section 7.2**. Then, in **Section 7.3**, the enhanced generated second harmonic signal from the metamaterial is reported. The optical nonlinear conversion efficiency is calculated in **Section 7.4**. Finally, the second order nonlinear tensor of the metamaterial is characterized in **Section 7.5**.

## 7.2 Experimental setup for second harmonic generation measurements



**Figure 7.1** Photo and schematic of the experimental setup

A 200 fs ultrafast laser is used as the pump source and the laser light is guided to a cage system by three mirrors. The cage system is used for imaging and excitation of the metamaterial. The generated signal from the metamaterial is collected by its integrated fibre and detected by a photomultiplier tube (PMT). A wave plate and a polarizer are used to control the pump laser’s power and polarization. Several filters are used to make sure the detected signal is the second harmonic signal generated by the metamaterial.

The experimental setup for the SHG experiments includes two important parts, the metamaterial excitation part and SH detection part, as shown in **Figure 7.1**. Considering that second harmonic generation by unstructured interfaces vanishes at normal incidence [70] and in order to detect second harmonic generation caused by the metamaterial structure, we measure SHG with a normally incident pump beam, which also ensures that 0<sup>th</sup> order SHG diffraction is within the acceptance angle of the optical fibre. The second-order nonlinear response of the metamaterial is excited by illuminating it with linearly polarized 200 fs optical pulses with 80 MHz repetition rate from an ultrafast optical parametric oscillator (**Spectra Physics Inspire HF 100**, more detail in

**Appendix A**). The centre wavelength of the pulses is tuned from 1440 nm to 1610 nm. The excitation laser pulses were guided by three mirrors to a half-wave plate (**Thorlabs AHWP10M-1600**). The half-wave plate together with a Glan-Thompson polarizer (**Thorlabs GTH10M**) controlled the polarization and intensity of the excitation laser.

A beam splitter is used to divert light for imaging of the samples. Then, the polarized pump laser pulses of the main path are focused onto the metamaterial, which is located on the cleaved end of a single mode optical fiber (**Thorlabs SM980-5.8-125**) with a numerical aperture of  $\sim 0.13$ , by a 10x objective (**Mitutoyo Plan Apo NIR Objective**) with a numerical aperture of 0.26. The fibre's numerical aperture of 0.13 implies that only the 0<sup>th</sup>-order diffraction of generated second harmonic radiation will be collected. Two longpass filters cutting off at 900 nm wavelength (**Thorlabs FELH0900**) are used to make sure that only pump laser light is focused on the samples. The spot size of the focused beam is  $24.7 \mu\text{m}^2$ . The peak intensity of the focused beam is about  $6.3 \text{ GW}/\text{cm}^2$  at 25 mW average power.

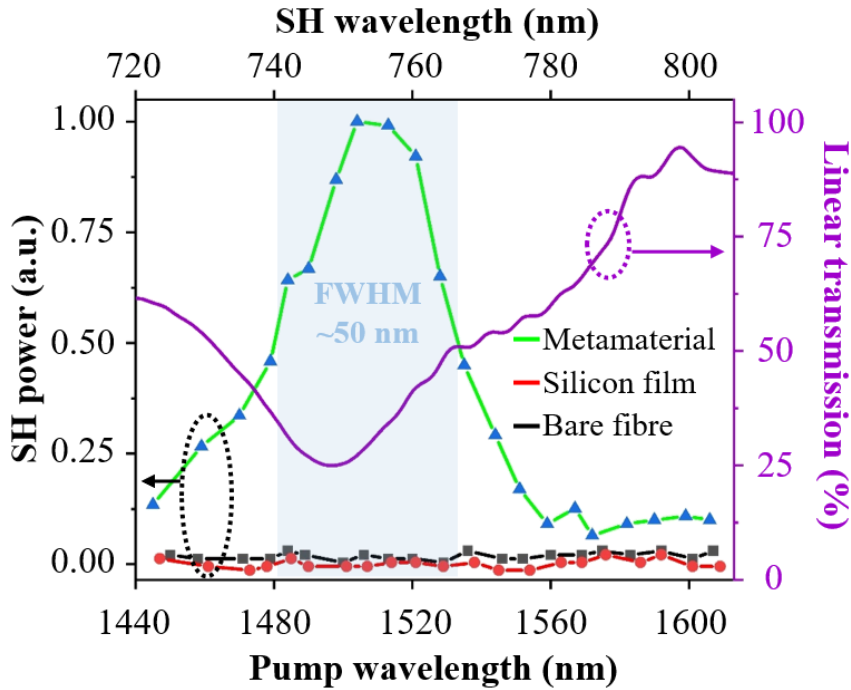
To separate the second harmonic signal from the fundamental pump laser, 3 shortpass filters (two **Thorlabs FESH0950**, one **Thorlabs FESH0850**) are used to block the pump and one longpass filter (**Thorlabs FELH0600**) is used to remove higher order nonlinear signals. These filters are mounted in two Thorlabs fiber optic filter mounts (**FOFMF/M**) and the total loss of these filters as well as the mounts is  $\sim 84\%$ .

The second harmonic signal of the power dependence experiment and the tensor characterization experiment is detected by a Hamamatsu photomultiplier tube (**H7421-50**), which has a counting efficiency of  $\sim 9\%$  at 750 nm (more details in **Appendix A**). The detector dark noise has been measured and subtracted from all second harmonic measurements.

### 7.3 Second harmonic signal arising from mesoscopic structuring

Second harmonic measurements are conducted with the metamaterial-bearing fibre and two unstructured reference fibres, one with and the other without the silicon film. Strong second harmonic emission is observed only for y-polarized pump light at 1510 nm wavelength with the metamaterial-bearing fibre. The detected second harmonic generation of the metamaterial as a function of the wavelength of the y-polarized pump beam is shown as green curve in **Figure 7.2**. The power of the second harmonic signal exhibits a resonantly enhanced feature. The second harmonic emission profile coincides with the metamaterial's resonance (purple curve), indicating that the nanostructure's resonance enhances the effective second order nonlinear response of the metamaterial. The FWHM of metamaterial's linear resonance is about 50 nm. This matches the observed width of the second harmonic generation peak. There is a 10 nm detuning between the

metamaterial’s transmission resonance and the peak of the second harmonic generation. This detuning may be caused by a small spectral shift between the absorption resonance and the transmission resonance[59, 171], where the absorption resonance plays the main role in enhancing second harmonic generation.



**Figure 7.2 Observation of second harmonic generation**  
 Detected spectral dependence of second harmonic (SH) emission by metamaterial on a cleaved fibre (green), unstructured silicon film on a cleaved fibre (red) and an unstructured bare cleaved fibre (black) alongside the metamaterial’s linear transmission spectrum (purple) for  $\gamma$ -polarized pump light.

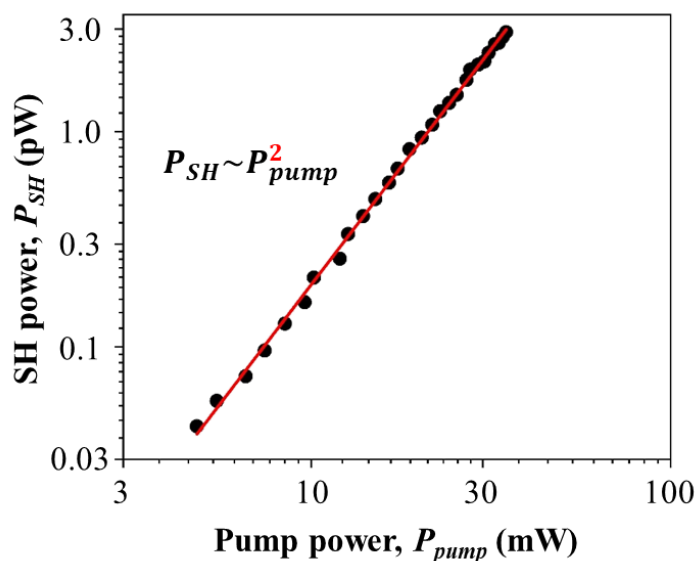
In order to confirm that the second harmonic generation is introduced by the metamaterial nanostructure, rather than the presence of the silicon film or the optical fibre, two control experiments were conducted on a bare fibre tip and on a tip of fibre covered by an unstructured 90-nm-thick layer of CVD-silicon. It is shown in **Figure 7.2** that no second harmonic generation above the noise level was detected in the control experiments on unstructured reference fibres with and without the silicon film, which confirms that the observed second harmonic generation is due to mesoscopic structuring.

### 7.4 Optical conversion efficiency

Then, power dependence measurements of the detected nonlinear signal have been performed to confirm the nonlinear order of the detected signal, for pumping at 1510 nm wavelength, shown in



**Figure 7.3.** The detected power exhibits a quadratic dependence on the incident pump power. Accounting for the detection efficiency of the photomultiplier tube as well as the losses in the detection optics (fibres and filters), 2.9 pW second harmonic power ( $P_{SH}$ ) has been observed for 35 mW  $y$ -polarized average pump power ( $P_{pump}$ ), corresponding to a second harmonic generation power conversion efficiency of at least  $\eta = P_{SH}/P_{pump} = 0.8 \times 10^{-10}$ , which is comparable with efficiencies in metallic structures [172, 173] and exceeds previously reported silicon metamaterial by four orders of magnitude [25]. We note that the fibre's refractive index of about 1.45 implies that some diffraction will occur into the fibre at free-space wavelengths shorter than 1.6  $\mu\text{m}$ , while diffraction into air occurs at wavelengths shorter than 1.1  $\mu\text{m}$ . The fibre's numerical aperture of 0.13 implies that only radiation propagating close to normal to the metamaterial will be collected. Therefore, the calculated efficiency of our structure only accounts for 0<sup>th</sup> order diffraction of SHG into the fibre. Diffraction of SHG up to the 1<sup>st</sup> order into air and up to the 2<sup>nd</sup> order into glass implies that the metamaterial's true SHG efficiency may be a few times higher. Besides, no saturation of SH intensity can be seen in **Figure 7.3**, which implies that the conversion efficiency is likely to become even larger with increasing pumping power.



**Figure 7.3 Power dependence of second harmonic generation by the metamaterial**

Power dependence of second harmonic generation by the metamaterial (black dots) with a quadratic fit (red curve) at 1510 nm pump wavelength for  $y$ -polarized pump light.

To allow comparison with other materials, we need to consider that phase-matched – sufficiently thin films are always phase matched – SH conversion efficiency increases linearly with pump peak intensity ( $I$ ) and quadratically with interaction length ( $L$ ).

The measured SH efficiency is  $\eta=0.8\times 10^{-10}$  at a pump intensity of  $I=8.8$  GW/cm<sup>2</sup>. The interaction length, which is the thickness of the metamaterial, is  $L=346$  nm. The normalized efficiency is given by:  $\frac{\eta}{IL^2} = 8 \times 10^{-3}/\text{GW}$ .

We assume SH generation with perfect phase matching, which is automatically satisfied for materials of sub-wavelength thickness. The effective nonlinear susceptibility  $\chi_{eff}^{(2)}$  can be estimated as [32]:

$$I_{SHG} = \frac{\omega_p^2 (\chi_{eff}^{(2)})^2 L^2}{2n_{SH} n_p^2 c^3 \epsilon_0} I^2 \quad (7.1)$$

$I_{SHG}$  is the intensity of the generated SH signal,  $\omega_p$  is the pump frequency.  $n_{SH}$  and  $n_p$  are the refractive index of silicon at SH wavelength and pump wavelength, respectively. The vacuum speed of light is  $c$  and the vacuum permittivity is  $\epsilon_0$ . If we assume  $n_{SH} = n_p = 3.5$  (for silicon), then  $\chi_{eff}^{(2)} = 0.3$  pm/V.

Therefore we arrive at a normalized efficiency of  $\eta/(IL^2) = 8 \times 10^{-3}/\text{GW}$  corresponding to  $\chi_{yyy}^{(2)} \sim 0.3$  pm/V, which is comparable to KDP [32]. The normalized efficiency reported here exceeds previous silicon metamaterial [25] by two orders of magnitude, see **Table 7.1**. This improvement is largely due to resonant enhancement of second harmonic generation at the closed-mode resonance of the double chevron structure.

**Table 7.1 Comparison of our Si metamaterial with the nearest state of the art:**

	<b>Our metamaterial</b>	<b>Si metamaterial [25]</b>
Material	a-Si on glass fibre tip	a-Si on glass
Meta-atom	Double chevron grooves	L-shape
Period, $\Lambda_x \times \Lambda_y$ (nm)	1000×1100	390×390
Thickness, $L$ (nm)	346	280
Pump wavelength, $\lambda$ (nm)	1510	840
Average pump power, $P_{pump}$ (mW)	35	~225
Repetition rate, $f_R$ (MHz)	80	80
Pulse width, $\tau$ (fs)	200	100
Pump peak intensity, $I$ (GW/cm <sup>2</sup> )	8.8	~0.36
SH conversion efficiency, $\eta$	$0.8 \times 10^{-10}$	$\sim 10^{-14}$
SH normalized efficiency, $\eta/(IL^2)$	$8 \times 10^{-3}/\text{GW}$	$\sim 3.6 \times 10^{-5}/\text{GW}$

## 7.5 Contribution of each allowed $\chi^{(2)}$ component

According to symmetry analysis, this metamaterial – and any other structure of D1 symmetry with symmetry axis  $y$  - has three allowed components of the second-order susceptibility:  $\chi_{yyy}^{(2)}$ ,  $\chi_{yxx}^{(2)}$  and  $\chi_{xyx}^{(2)} = \chi_{xxy}^{(2)}$ . However, second harmonic detection through the standard single-mode fibre, that hosts the nonlinear metamaterial and does not maintain polarization, does not allow direct polarization measurements on the generated second harmonic light. In order to probe the relative strengths of the allowed susceptibility components, the generated second harmonic power was detected while driving the metamaterial with left-circularly, right-circularly and linearly polarized pump fields at several orientations relative to metamaterial symmetry axis. The second-order susceptibility tensor components were extracted by fitting the pump-polarization-dependent intensity of generated second harmonic signal into the relation equations between the second order nonlinear tensors and the intensity of generated SH signal, shown in the following:

### 7.5.1 Pump field

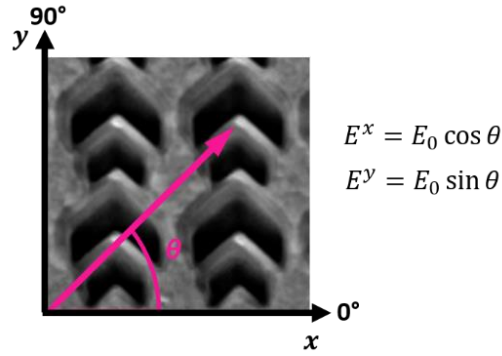
The incident field that drives the metamaterial is given by:

$$E(t) = \alpha \sqrt{P_{pump}} \cdot (\hat{x} \cos \theta + \hat{y} \sin \theta e^{i\phi}) e^{i\omega t} \quad (7.2)$$

Electric field and incident power  $P_{pump}$  are linked by a proportionality constant  $\alpha$ ,  $|E(t)|^2 = \alpha^2 P_{pump}$ . The angle  $\phi$  determines the polarization ellipticity of the incident light. In case of linearly polarized light ( $\phi=0$ ),  $\theta$  is the polarization azimuth measured relative to the  $x$ -axis. The  $y$ -polarization ( $\phi=0$ ,  $\theta=90^\circ$ ) is along the symmetry axis of the metamaterial, see **Figure 7.4**. Left and right circularly polarized pump light is given by  $\phi=\pm 90^\circ$  and  $\theta=45^\circ$ .

The observable field is given by the real part of the previous expression:

$$E_{obs}(t) = Re(E(t)) = \alpha \sqrt{P_{pump}} \cdot (\hat{x} \cos \theta \cos \omega t + \hat{y} \sin \theta \cos(\phi + \omega t)) \quad (7.3)$$



**Figure 7.4 Pump polarization angle relative to metamaterial**

Schematic of linearly polarized ( $\phi=0$ ) pump laser light of azimuth  $\theta$  incident on the metamaterial with symmetry axis  $y$ .

### 7.5.2 SHG intensity

Assuming the metamaterial has D1 symmetry with symmetry axis along  $y$ , the allowed second order nonlinear susceptibility tensor components are:  $\chi_{xxy}^{(2)} = \chi_{xyx}^{(2)}, \chi_{yxx}^{(2)}, \chi_{yyy}^{(2)}$ , where the first index indicates the second harmonic polarization, and the latter indices indicate the polarization of the pump wave.

It is convenient to parametrize them as:

$$\chi_{xyx}^{(2)} = \chi_{xxy}^{(2)} = ae^{i\gamma} \chi_{yyy}^{(2)} \tag{7.4}$$

$$\chi_{yxx}^{(2)} = be^{i\phi} \chi_{yyy}^{(2)} \tag{7.5}$$

Where  $a = |\chi_{xyx}^{(2)}/\chi_{yyy}^{(2)}|$ ,  $b = |\chi_{yxx}^{(2)}/\chi_{yyy}^{(2)}|$  are real-valued and non-negative. The second harmonic field is then (using Equation 7.2 and dropping  $\alpha$  and  $e^{i2\omega t}$  in the second step for simplicity):

$$\begin{aligned}
 E_{SH} \propto & (\chi_{xyx}^{(2)} + \chi_{xxy}^{(2)}) E_x E_y \cdot \hat{x} + (\chi_{yxx}^{(2)} E_x E_x + \chi_{yyy}^{(2)} E_y E_y) \cdot \hat{y} \\
 \propto & \chi_{yyy}^{(2)} P_{pump} \cdot \{2a \cos \theta \sin \theta \cdot e^{i(\phi+\gamma)} \cdot \hat{x} + (b \cos^2 \theta e^{i\phi} \\
 & + \sin^2 \theta e^{i2\phi}) \cdot \hat{y}\}
 \end{aligned} \tag{7.6}$$

The total second harmonic power is given by the sum of the  $x$ - and  $y$ -polarized second harmonic powers:

$$\begin{aligned}
 P_{SH} = P_{SH}^x + P_{SH}^y \propto & |E_{SH}^x|^2 + |E_{SH}^y|^2 \\
 \propto & |\chi_{yyy}^{(2)}|^2 P_{pump}^2 \cdot \{4a^2 \cos^2 \theta \sin^2 \theta + b^2 \cos^4 \theta + \sin^4 \theta \\
 & + 2b \cos^2 \theta \sin^2 \theta \cos(\phi - 2\phi)\}
 \end{aligned} \tag{7.7}$$

At this point we drop  $|\chi_{yyy}^{(2)}|^2$  and write this in terms of second harmonic photon counts  $N(\theta, \phi, P_{pump})$ , which correspond to the difference between the detected counts  $N_D(\theta, \phi, P_{pump})$  and the detector's dark-counts,  $N_{dark}$  that we assume to be constant. Important special cases are listed in **Table 7.1**.

$$\begin{aligned}
 N(\theta, \phi, P_{pump}) &= N_D(\theta, \phi, P_{pump}) - N_{dark} \\
 &\propto P_{pump}^2 \\
 &\cdot \{4a^2 \cos^2\theta \sin^2\theta + \sin^4\theta + b^2 \cos^4\theta \\
 &+ 2b \cos^2\theta \sin^2\theta \cos(\phi - 2\phi)\}
 \end{aligned} \tag{7.8}$$

**Table 7.2** Second harmonic photon counts for selected pump polarizations

Pump polarization	Second harmonic photon counts, $N(\theta, \phi, P_{pump})$
Circular $\phi=\pm 90^\circ, \theta=45^\circ$	$P_{pump}^2 \cdot \{a^2 + \frac{1}{4} + \frac{1}{4}b^2 - \frac{1}{2}b \cos(\phi)\}$
Diagonal linear $\phi=0^\circ, \theta=45^\circ$ or $135^\circ$	$P_{pump}^2 \cdot \{a^2 + \frac{1}{4} + \frac{1}{4}b^2 + \frac{1}{2}b \cos(\phi)\}$
x-polarization $\phi=0^\circ, \theta=0^\circ$	$P_{pump}^2 \cdot \{b^2\}$
y-polarization $\phi=0^\circ, \theta=90^\circ$	$P_{pump}^2 \cdot \{1\}$

### 7.5.3 Linear and circular polarization experiments

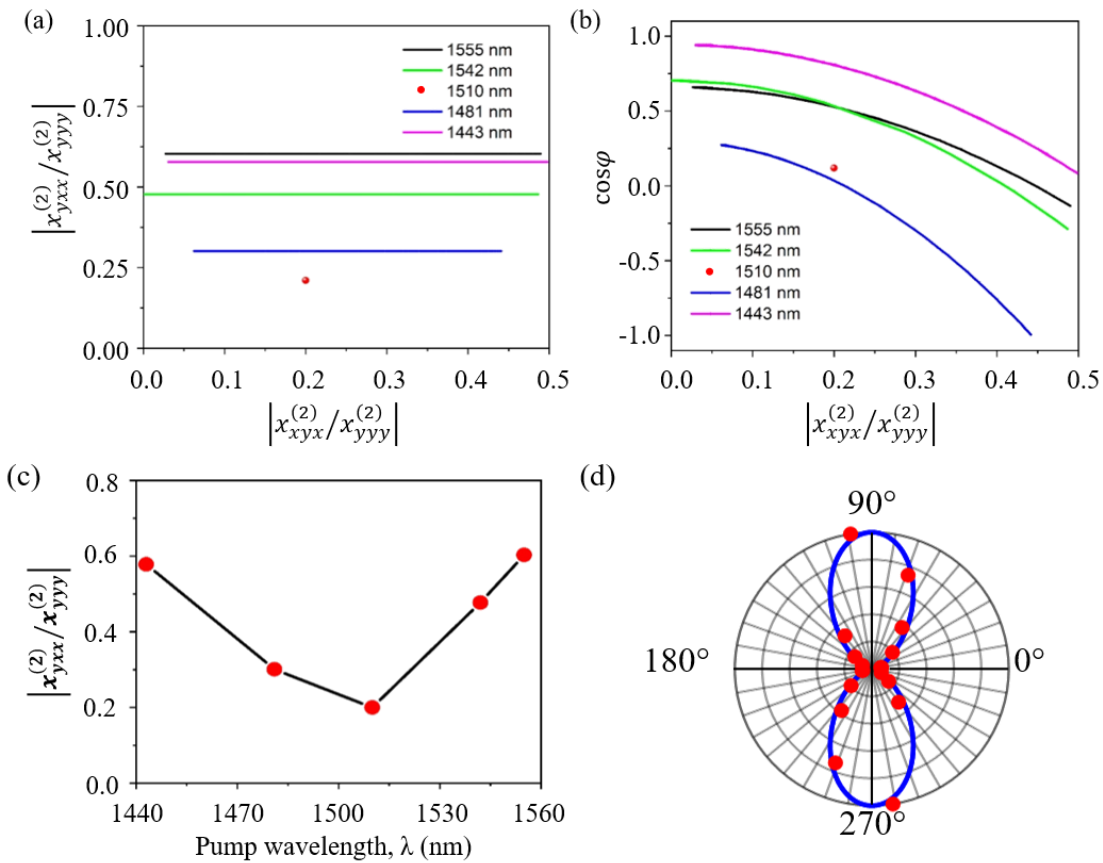
For linear pump polarization ( $\phi=0^\circ$ ) at fixed pump power  $P_{pump}$ , the pump azimuth ( $\theta$ ) dependence of second harmonic photon counts relative to the case of y-polarized pumping is given by:

$$\begin{aligned}
 \frac{N(\theta, 0, P_{pump})}{N(90^\circ, 0, P_{pump})} &= \frac{N_D(\theta, 0, P_{pump}) - N_{dark}}{N_D(90^\circ, 0, P_{pump}) - N_{dark}} \\
 &= 4a^2 \cos^2\theta \sin^2\theta + \sin^4\theta + b^2 \cos^4\theta + 2b \cos^2\theta \sin^2\theta \cos(\phi)
 \end{aligned} \tag{7.9}$$

The second harmonic photon counts as a function of the linear polarization angle  $\theta$  of the excitation laser were measured at five pump wavelengths and fitted by **Equation 7.9**. Brute-force lookup of all the possible values for  $a = |\chi_{xyx}^{(2)}/\chi_{yyy}^{(2)}|$ ,  $b = |\chi_{yxx}^{(2)}/\chi_{yyy}^{(2)}|$ , and  $\phi = \arg \chi_{yxx}^{(2)} - \arg \chi_{yyy}^{(2)}$  constrains the nonlinear susceptibility tensor components that are consistent with the experiments. The range of possible solutions is shown by **Figure 7.5**.  $|\chi_{yxx}^{(2)}/\chi_{yyy}^{(2)}|$  is well-constrained at each

pumping wavelength, see **Figure 7.5(a,c)**. However, experiments with only linear pump polarization yield a range of solutions for  $\left| \chi_{xyx}^{(2)} / \chi_{yyy}^{(2)} \right|$  and  $\cos \varphi$ , shown in **Figure 7.5(b)**.

To break this ambiguity and fully characterize the susceptibility tensor components of our metamaterial, we further measured second harmonic generation with circularly and linear polarized excitation at 1510 nm pump wavelength, where the second harmonic generation is strongest. **Figure 7.5d** shows generated second harmonic power as a function of the azimuth of the linear pump polarization at 1510 nm pump wavelength. The measurements were conducted at an average power of 12 mW. Through fitting the generated SH signal by the circular as well as linear polarized pump into **Equation 7.8** (see also **Table 7.1**), we found  $\left| \chi_{xyx}^{(2)} / \chi_{yyy}^{(2)} \right| = 0.2$ ,  $\left| \chi_{yxx}^{(2)} / \chi_{yyy}^{(2)} \right| = 0.2$  and  $\varphi = \pm 83^\circ$  at a pump wavelength of 1510 nm.



**Figure 7.5 Contribution of each allowed  $\chi^{(2)}$  component**

(a) Possible susceptibility ratios  $\left| \chi_{yxx}^{(2)} / \chi_{yyy}^{(2)} \right|$  as a function of possible ratios  $\left| \chi_{xyx}^{(2)} / \chi_{yyy}^{(2)} \right|$ . (b) Possible values of  $\cos \varphi$  as a function of possible ratios  $\left| \chi_{xyx}^{(2)} / \chi_{yyy}^{(2)} \right|$ . (c) The dependence of  $\left| \chi_{yxx}^{(2)} / \chi_{yyy}^{(2)} \right|$  on the pump wavelength. (d) The generated second harmonic power as a function of the azimuth of the linear pump polarization at 1510 nm pump wavelength (the resonance). Dots indicate measurements and the blue curve shows a fit according to **Equation (7.8)**.

## 7.6 Discussion

Beyond symmetry considerations and the observed Fano resonance, we note that the structure may also support guided modes within the metamaterial layer [174, 175], which could play a role in coupling resonators and SHG. Furthermore, while diffraction above the 0<sup>th</sup> order will not be guided by the fibre and thus cannot contribute directly to the detected SHG, it could affect the conversion efficiency indirectly.

Our results show how pumping at an anti-symmetric Fano-type resonance of a structure lacking inversion symmetry yields substantial second harmonic generation in an amorphous silicon metamaterial. We believe that the second-order nonlinearity can be increased further by increasing the Q-factor of this resonance and by engineering a second resonance at the SHG wavelength. This may be achieved by adjusting the metamaterial design, more accurate nanofabrication (to avoid inhomogeneous broadening) and by avoiding gallium ion implantation during nanofabrication (e.g. by using electron beam lithography or imprint techniques).

In fact, to further improve the SH conversion efficiency, I have already designed and fabricated a new sample with double triangles in one unit cell. This sample shows resonances at about 1.6  $\mu\text{m}$  and 810 nm, which can enhance local field at both fundamental as well as second harmonic wavelengths. More details about the sample with D3 symmetry structure can be found in **Appendix B**. Experimentally demonstrating SHG from this sample will be part of the future work (see **Chapter 8**).

## 7.7 Summary

In summary, I have demonstrated resonance enhanced second harmonic generation in a fibre integrated all-dielectric metasurface. The results in this chapter indicate that:

- (1) Strong second harmonic emission is observed for y-polarized pump light at 1510 nm wavelength, corresponding to a nonlinear susceptibility of  $x_{eff}^{(2)} = 0.3 \text{ pm/V}$ . No second harmonic generation exceeding the noise level has been detected in control experiments on unstructured reference fibres with and without the silicon film, confirming that the observed second harmonic generation is caused by the mesoscopic structuring.
- (2) The second harmonic emission peak coincides with the metamaterial's resonance, indicating that the nanostructure's resonance enhances the effective second order nonlinear response of the metamaterial.

- (3) A progressive decline in the level of second harmonic signal is observed as the polarization of the pump is turned from the y-axis towards the x-axis, which is consistent with  $\left| \chi_{xyx}^{(2)} / \chi_{yyy}^{(2)} \right| = 0.2$ ,  $\left| \chi_{yxx}^{(2)} / \chi_{yyy}^{(2)} \right| = 0.2$ .
- (4) A power conversion efficiency on the order of  $10^{-10}$  has been observed with a y-polarized 35 mW average power pump beam at the metamaterial's resonance wavelength, which is four orders of magnitude higher SH efficiency than previous silicon metamaterial. The normalized conversion efficiency is  $8 \times 10^{-3} / \text{GW}$  [149], which is two orders of magnitude higher than for previous silicon metamaterial [25].

Our findings demonstrate how mesoscopic structuring – that combines closed-mode resonances with a suitable choice of point group symmetry – enables the fabrication of metamaterials with quadratic optical nonlinearity from amorphous dielectrics. Second harmonic generation by the double-chevron metamaterial of D1 symmetry is most efficient for pump light polarized along its symmetry axis and all allowed total second-order nonlinear susceptibility tensor components have been determined. Ease of deposition of amorphous materials shall enable the fabrication of nonlinear elements of nanoscale thickness on complex non-planar platforms, such as end-facets of optical fibres and silicon photonics waveguides.



## Chapter 8 Conclusions and outlook

### 8.1 Conclusion

Second-order nonlinear optical processes are of considerable importance for laser technologies, quantum optics, materials characterization, spectroscopy, imaging, as well as wavelength conversion for optical signals and all optical information processing. Optical second harmonic generation inherently depends on the microscopic structure of materials and only occurs in media without inversion symmetry under dipole approximation. Efficient even-order nonlinear effects typically rely on thick non-centrosymmetric crystals, and hamper the potential for miniaturization of photonic devices, which in turn limits the speed, efficiency and scalability of photonic technology. Recent progress in the field of metamaterials promises to revolutionize nonlinear optics. Metamaterials can break limits of naturally available materials and artificially enhance and modify the materials' nonlinear properties (such as second harmonic generation) by nanostructuring using nanofabrication techniques. This thesis theoretically studied structuring enabled nonlinearity and experimentally demonstrated second harmonic generation in a fibre-integrated all dielectric metamaterials. In this thesis:

A Coulomb-coupled-oscillator model has been developed for predicting optical nonlinearity in 2D nanostructures and demonstrates that in the confined geometry of a two-dimensional nanoparticle the collective nonlinear response of the atomic array can arise from the Coulomb interactions of the optical electrons, even if the individual atoms exhibit no nonlinearity. The model was then applied to study harmonic and sum frequency generation in 2D nanostructures and shows that odd order and even order nonlinearities scale with the area and perimeter of nanoparticles, respectively. The model allows the simulation of large collections of atoms and mapping of the origin of harmonic and sum frequency generation in nanostructures. The model allows the design and optimization of nonlinear dielectric nanostructures for nanophotonics.

Even order harmonics are not allowed in structures with even-fold rotational symmetry, but defects can break the symmetry. A model of defect induced harmonic generation in 2D nanoparticles has been reported. The model shows that defects have a large influence on even harmonic generation of 2D nanostructures. Information could be encoded in atomic defects via defect engineering and read by their harmonic generation signature. Such information could be written by AFM-based techniques and read by scanning near-field microscopy techniques.

A fibre-integrated amorphous silicon metamaterial with meta-atoms of D1 symmetry has been designed and fabricated. The metamaterial is a double chevron array that supports a closed-mode

resonance for the fundamental wavelength at 1510 nm with a quality factor of 30. I have experimentally demonstrated second harmonic generation in the amorphous silicon metamaterial with a normalized second harmonic conversion efficiency of  $8 \times 10^{-3}/\text{GW}$ , which exceeds the previously achieved value for a silicon metamaterial by two orders of magnitude. This improvement is achieved by exploiting the double-chevron structure's closed-mode resonance. The findings demonstrate how mesoscopic structuring – that combines closed-mode resonances with a suitable choice of point group symmetry – enables the fabrication of metamaterials with quadratic optical nonlinearity from amorphous dielectrics. Ease of deposition of amorphous materials shall enable the fabrication of nonlinear elements of nanoscale thickness on complex non-planar platforms, such as end-facets of optical fibres and silicon photonics waveguides.

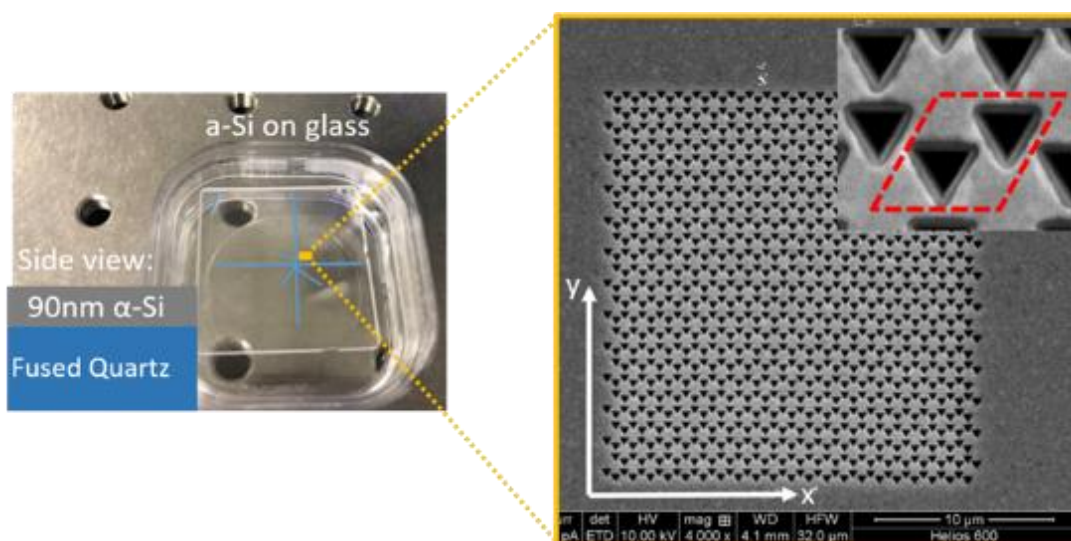
The results of this thesis can be applied to design nonlinear metamaterials and provide clear guidance on enhancing and controlling the nonlinear response of nanoscale planar optical devices and metamaterials.

## 8.2 Outlook

### 8.2.1 Further improve SH efficiency

In this Thesis, I mainly discussed second harmonic generation enabled by nanostructuring. SHG from an amorphous silicon metamaterial has been experimentally achieved with a power conversion efficiency of  $\sim 10^{-10}$ . However, the nonlinear efficiency can be further improved by enhancing local fields at both fundamental and SH wavelengths.

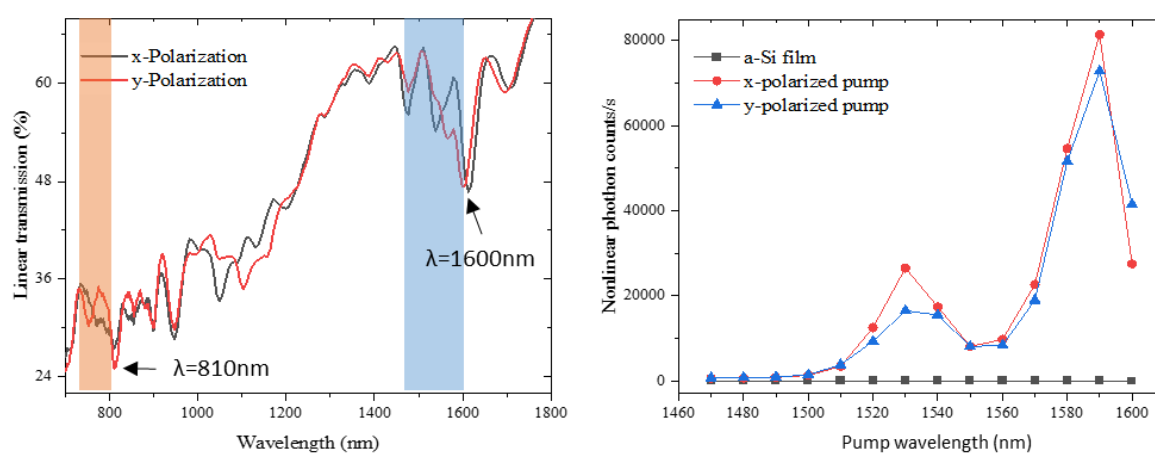
In fact, I have fabricated a new sample of D3 symmetry structures, which exhibits multi-resonances, as shown in **Figure 8.1** (Some details can be found in **Appendix B**). The resonances at two,  $\sim 1600$  nm and  $\sim 810$  nm, wavelengths can be used to enhance the fields at fundamental and SH wavelengths, respectively. In addition, the D3 symmetry only allows one independent second order susceptibility  $\chi_{xxy}^{(2)} = \chi_{xyx}^{(2)} = \chi_{yxx}^{(2)} = -\chi_{yyy}^{(2)}$ , which will simplify the interpretation of SHG measurements.



**Figure 8.1** Images of a multi-resonant metamaterial

The multi-resonant metamaterial is based on amorphous silicon and fabricated on a glass substrate (a piece of quartz glass). The inset shows SEM images of the entire and partial metamaterial. The red frame indicates the unit cell of the metamaterial - a pair of triangles.

Initial experiments reveal a resonantly enhanced nonlinear signal from the metamaterial as shown in **Figure 8.2b**. However, it is not confirmed whether the signal due to the second harmonic or higher harmonics, since power dependence experiments have not been conducted yet. However, it is pretty clear that the nonlinear signal is induced by the nanostructure, since in control experiments on an unstructured silicon film, no nonlinear signal is observed.

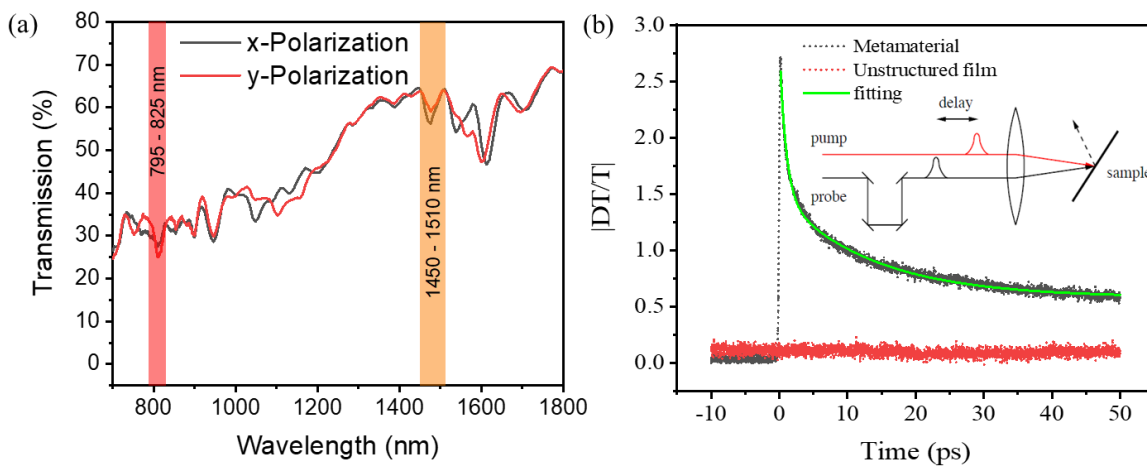


**Figure 8.2** Linear and nonlinear spectra of the new metamaterial

(a) Linear and (b) nonlinear transmission spectra of new metamaterial consisting of D3 symmetry nanostructures.

### 8.2.2 Explore other nonlinear effects

Beyond second harmonic generation, mesoscopic structuring of matter can also enable other nonlinear effects. The transient transmission spectra of the new metamaterial have been measured, using resonances at about 1450 nm-1510 nm as pump signal and at 795 nm-825 nm as probe signal. The pump probe process is illustrated as the insert in **Figure 8.3b**. The metamaterial has a resonance at the pump wavelength as well as at probe wavelength, while unstructured film has no resonances. As a result, the metamaterial introduces absorption, which is not presented in unstructured silicon film, as shown in **Figure 8.3b**.



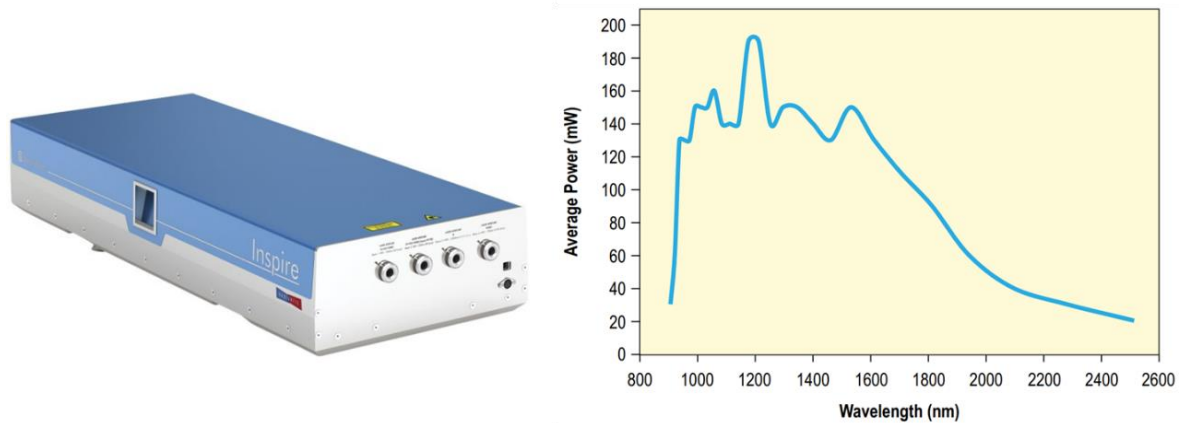
**Figure 8.3** Transient nonlinear transmission from the new metamaterial

(a) The measured transmission spectra of the new metamaterial. The pump and probe wavelengths are marked by the orange and red shadows, respectively. (b) The transient transmission from the new metamaterial and an unstructured silicon film. The insert shows the schematic of pump-probe experiments.

Moreover, the experimental demonstration of second harmonic generation in this thesis indicates that other second order nonlinear effects such as sum frequency, difference frequency generation are also possible. Spontaneous down conversion and optical rectification may also be present in the metamaterials, but their observation requires detectors with high enough sensitivity.

These results show that the metamaterials demonstrated in this thesis have the potential to be developed into multi-functional devices and can be integrated with optical fibres and silicon photonics waveguides, which indicates a potential for application in all-optical information processing.

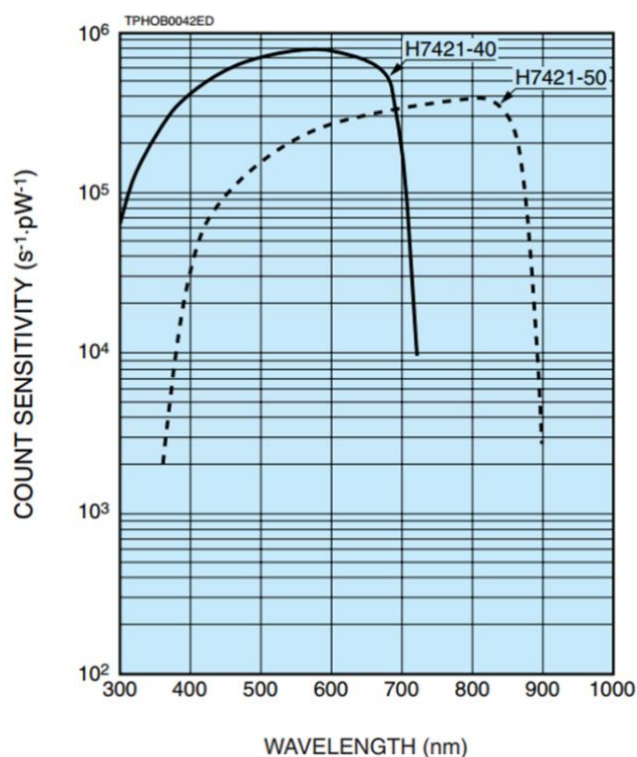
## Appendix A Specifications of major equipment



**Figure A1. Spectra Physics Inspire HF 100 ultrafast optical parametric oscillator**

Image and idler emission spectrum of the **Spectra Physics Inspire HF 100** ultrafast optical parametric oscillator.

The **Spectra Physics Inspire HF 100** ultrafast optical parametric oscillator is used as pump source for my second harmonic generation experiments on the fibre integrated all dielectric metasurface. The laser can emit ultrafast pulses from 930 nm to 2500 nm wavelength. The output power of the laser is fixed for each wavelength, as shown in **Figure A1**. To get the SH spectra (**Figure 7.2**), we calibrate the pump laser power and make sure the output power for wavelengths from 1440 nm to 1610 nm is at the same level.

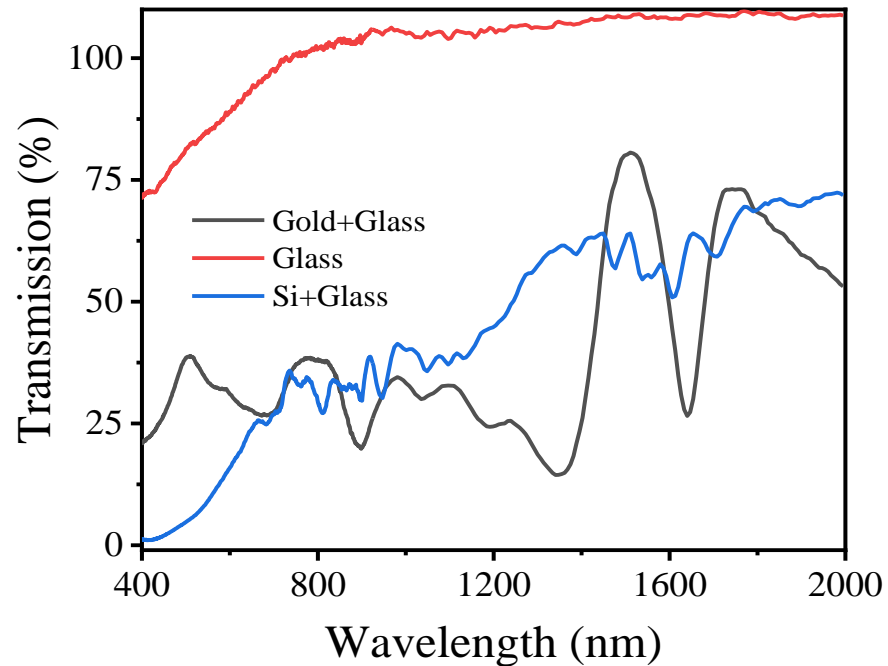


**Figure A2. H7421-50 Hamamatsu photomultiplier tube**

The image and counting sensitivity of H7421-50 Hamamatsu photomultiplier tube

The SH nonlinear spectrum in **Chapter 7** is detected by pumping from 1440 nm to 1610 nm wavelength, corresponding to SH wavelength from 720 nm to 805 nm. The H7421-50 Hamamatsu photomultiplier tube contains a GaAs photocathode and has a high counting sensitivity within the SH wavelength range, shown in **Figure A2**. For example, the counting efficiency is ~9% at 750 nm and ~10% at 800 nm. The PMT has a built-in thermoelectric cooler, allowing measurements with a good signal to noise ratio even at very low light levels. Its typical dark count is only ~50 counts/s.

## Appendix B Multi-resonant silicon metamaterial



**Figure B1** Transmission spectra after each fabrication step.

The metamaterial shown in **Figure 8.1** is fabricated using a similar process as the reported fibre-integrated all-dielectric metasurface in **Chapter 6**. The metamaterial is fabricated on a piece of quartz glass. First, a layer of 50 nm-thick Au film is deposited on the glass substrate, then the Au film is structured using FIB milling. The spectrum of the structured Au on glass is measured, see the black curve in **Figure B1**. A resonance at 1600 nm wavelength is observed. Then the Au film is removed through a wet etching process, leaving a structured glass, which shows no resonances (red curve in **Figure B1**). Finally, a 90 nm thickness amorphous silicon layer is deposited on the structured glass. At this stage, multiple resonances are exhibited by the metamaterial, see the blue curve in **Figure B1**.





## Appendix C      **Publications**

### C.1      **Journal publications**

- **Jie Xu**, Eric Plum, Vassili Savinov, and Nikolay I. Zheludev. **“Second harmonic generation in amorphous silicon-on-silica metamaterial.”** APL Photonics, 6(3) 036110 (2021)
- **Jie Xu**, Eric Plum, and Vassili Savinov. **“Toy model of second harmonic generation due to structuring of centrosymmetric films.”** Optics Express 28(22): 33346-33354 (2020)
- **Jie Xu**, Vassili Savinov, and Eric Plum. **“Toy model of harmonic and sum frequency generation in 2D dielectric nanostructures.”** Scientific Reports, 11: 20120 (2021)
- **Jie Xu**, and Eric Plum. **“Defect-induced nonlinearity in 2D nanoparticles.”** arXiv:2109.10308 (Accepted by Optics Express, in press)

### C.2      **Conference contributions**

- **J. Xu**, E. Plum, V. Savinov, and N. I. Zheludev, **Second harmonic generation by silicon metamaterial on a fibre tip**, CLEO Europe 2021 Virtual Conference, 21 - 25 June 2021 (Invited)
- **J. Xu**, E. Plum, V. Savinov, and N. I. Zheludev, **Second harmonic generation in a fiberized amorphous silicon metamaterial**, CLEO 2021 Virtual Conference, 9 - 14 May 2021 (Oral)
- **J. Xu**, V. Savinov, E. Plum, and N. I. Zheludev, **Optical second harmonic generation in amorphous silicon metamaterial**, Metamaterials' 2019, Rome, Italy, 16 - 21 Sep 2019 (Oral)
- **J. Xu**, V. Savinov, E. Plum, and N. I. Zheludev, **Second harmonic generation due to mesoscopic structuring in dielectric metamaterial**, Nanometa 2019, Seefeld, Austria, 3 - 6 Jan 2019 (Poster)



## Bibliography

1. Maiman, T.H., *Stimulated optical radiation in ruby*. Nature, 1960. **187**(4736): p. 493-494.
2. Smith, D.R., et al., *Composite medium with simultaneously negative permeability and permittivity*. Physical Review Letters, 2000. **84**(18): p. 4184-4187.
3. Shelby, R.A., D.R. Smith, and S. Schultz, *Experimental verification of a negative index of refraction*. Science, 2001. **292**(5514): p. 77-79.
4. Veselago, V.G., *The electrodynamics of substances with simultaneously negative values of  $\epsilon$  and  $\mu$* . Soviet Physics Uspekhi, 1968. **10**(4): p. 509.
5. Linden, S., et al., *Magnetic response of metamaterials at 100 terahertz*. Science, 2004. **306**(5700): p. 1351-1353.
6. Zhang, S., et al., *Midinfrared resonant magnetic nanostructures exhibiting a negative permeability*. Physical Review Letters, 2005. **94**(3): p. 037402.
7. Cai, W., et al., *Metamagnetics with rainbow colors*. Optics Express, 2007. **15**(6): p. 3333-3341.
8. Zhang, S., et al., *Experimental demonstration of near-infrared negative-index metamaterials*. Physical Review Letters, 2005. **95**(13): p. 137404.
9. Dolling, G., et al., *Simultaneous negative phase and group velocity of light in a metamaterial*. Science, 2006. **312**(5775): p. 892-894.
10. Podolskiy, V.A. and E.E. Narimanov, *Near-sighted superlens*. Optics Letters, 2005. **30**(1): p. 75-77.
11. Aydin, K., I. Bulu, and E. Ozbay, *Subwavelength resolution with a negative-index metamaterial superlens*. Applied Physics Letters, 2007. **90**(25): p. 254102.
12. Schurig, D., et al., *Metamaterial electromagnetic cloak at microwave frequencies*. Science, 2006. **314**(5801): p. 977-980.
13. Liu, R., et al., *Broadband ground-plane cloak*. Science, 2009. **323**(5912): p. 366-369.
14. Lapine, M., M. Gorkunov, and K. Ringhofer, *Nonlinearity of a metamaterial arising from diode insertions into resonant conductive elements*. Physical Review E, 2003. **67**(6): p. 065601.
15. Zharov, A.A., I.V. Shadrivov, and Y.S. Kivshar, *Nonlinear properties of left-handed metamaterials*. Physical Review Letters, 2003. **91**(3): p. 037401.
16. Agranovich, V.M., et al., *Linear and nonlinear wave propagation in negative refraction metamaterials*. Physical Review B, 2004. **69**(16).
17. Klein, M.W., et al., *Second-harmonic generation from magnetic metamaterials*. Science, 2006. **313**(5786): p. 502-504.
18. Wang, L., et al., *Nonlinear wavefront control with all-dielectric metasurfaces*. Nano Letters, 2018. **18**(6): p. 3978-3984.
19. Konishi, K., et al., *Polarization-controlled circular second-harmonic generation from metal hole arrays with threefold rotational symmetry*. Physical Review Letters, 2014. **112**(13): p. 135502.
20. Butet, J., P.F. Brevet, and O.J.F. Martin, *Optical second harmonic generation in plasmonic nanostructures: from fundamental principles to advanced applications*. ACS Nano, 2015. **9**(11): p. 10545-10562.
21. Czaplicki, R., et al., *Second-harmonic generation from metal nanoparticles: resonance enhancement versus particle geometry*. Nano Letters, 2015. **15**(1): p. 530-534.
22. Gennaro, S.D., et al., *The interplay of symmetry and scattering phase in second harmonic generation from gold nanoantennas*. Nano Letters, 2016. **16**(8): p. 5278-5285.
23. Minovich, A.E., et al., *Functional and nonlinear optical metasurfaces*. Laser & Photonics Reviews, 2015. **9**(2): p. 195-213.
24. Panoiu, N.C., et al., *Nonlinear optics in plasmonic nanostructures*. Journal of Optics, 2018. **20**(8): p. 083001.

## Bibliography

25. Bar-David, J. and U. Levy, *Nonlinear diffraction in asymmetric dielectric metasurfaces*. Nano Letters, 2019. **19**(2): p. 1044-1051.
26. Habibullah, Y.B., K. Iwata, and T. Ishihara, *Second-harmonic generation from complementary Au metasurfaces with triangular resonators*. Journal of the Optical Society of America B-Optical Physics, 2019. **36**(4): p. 1166-1175.
27. Husu, H., et al., *Metamaterials with tailored nonlinear optical response*. Nano Letters, 2012. **12**(2): p. 673-677.
28. Kauranen, M. and A.V. Zayats, *Nonlinear plasmonics*. Nature Photonics, 2012. **6**(11): p. 737.
29. Langrock, C., et al., *All-optical signal processing using  $\chi^{(2)}$  nonlinearities in guided-wave devices*. Journal of Lightwave Technology, 2006. **24**(7): p. 2579-2592.
30. Willner, A.E., et al., *All-optical signal processing techniques for flexible networks*. Journal of Lightwave Technology, 2019. **37**(1): p. 21-35.
31. Franken, P.A., et al., *Generation of optical harmonics*. Physical Review Letters, 1961. **7**(4): p. 118-119.
32. Boyd, R.W., *Nonlinear Optics*. 3rd ed. 2008, Burlington, MA: Academic Press.
33. Bloembergen, N., *Nonlinear optics: past, present, and future*. IEEE Journal of Selected Topics in Quantum Electronics, 2000. **6**(6): p. 876-880.
34. Zheludev, N.I. and V.I. Emel'yanov, *Phase matched second harmonic generation from nanostructured metallic surfaces*. Journal of Optics A: Pure and Applied Optics, 2004. **6**(1): p. 26-28.
35. Shen, Y.R., *Surface nonlinear optics: a historical perspective*. IEEE Journal of Selected Topics in Quantum Electronics, 2000. **6**(6): p. 1375-1379.
36. Shen, Y.R., *The principles of nonlinear optics*. 1984, New York: Wiley-Interscience.
37. Bloembergen, N., et al., *Optical second-harmonic generation in reflection from media with inversion symmetry*. Physical Review, 1968. **174**(3): p. 813-822.
38. Alexandrova, S., P. Danesh, and I.A. Maslyanitsyn, *Second harmonic generation in hydrogenated amorphous silicon*. Physical Review B, 2000. **61**(16): p. 11136-11138.
39. Kessels, W.M.M., et al., *Spectroscopic second harmonic generation measured on plasma-deposited hydrogenated amorphous silicon thin films*. Applied Physics Letters, 2004. **85**(18): p. 4049-4051.
40. Lettieri, S., et al., *Second harmonic generation analysis in hydrogenated amorphous silicon nitride thin films*. Applied Physics Letters, 2007. **90**(2): p. 021919.
41. Soukoulis, C.M. and M. Wegener, *Past achievements and future challenges in the development of three-dimensional photonic metamaterials*. Nature Photonics, 2011. **5**(9): p. 523-530.
42. Hess, O., et al., *Active nanoplasmonic metamaterials*. Nature materials, 2012. **11**(7): p. 573-584.
43. Zheludev, N.I. and Y.S. Kivshar, *From metamaterials to metadevices*. Nature Materials, 2012. **11**(11): p. 917-924.
44. Yu, N., et al., *Light propagation with phase discontinuities: generalized laws of reflection and refraction*. Science, 2011. **334**(6054): p. 333-337.
45. Kildishev, A.V., A. Boltasseva, and V.M. Shalaev, *Planar photonics with metasurfaces*. Science, 2013. **339**(6125).
46. Meinzer, N., W.L. Barnes, and I.R. Hooper, *Plasmonic meta-atoms and metasurfaces*. Nature Photonics, 2014. **8**(12): p. 889-898.
47. Yu, N. and F. Capasso, *Flat optics with designer metasurfaces*. Nature materials, 2014. **13**(2): p. 139-150.
48. Lochner, F.J.F., et al., *Polarization-dependent second harmonic diffraction from resonant GaAs metasurfaces*. Acs Photonics, 2018. **5**(5): p. 1786-1793.
49. Czaplicki, R., et al., *Less is more: enhancement of second-harmonic generation from metasurfaces by reduced nanoparticle density*. Nano Letters, 2018. **18**(12): p. 7709-7714.
50. Vabishchevich, P.P., et al., *Enhanced second-harmonic generation using broken symmetry III-V semiconductor Fano metasurfaces*. ACS Photonics, 2018. **5**(5): p. 1685-1690.

51. Popov, S., Y.P. Svirko, and N.I. Zheludev, *Susceptibility tensors for nonlinear optics*. 1995: CRC Press.
52. Jackson, J.D., *Classical electrodynamics*. 1999, American Association of Physics Teachers.
53. Hamermesh, M., *Group theory and its application to physical problems*. 2012: Courier Corporation.
54. Authier, A., *International tables for crystallography: Volume D: Physical properties of crystals*. 2003: Wiley Online Library.
55. Canfield, B.K., et al., *Linear and nonlinear optical responses influenced by broken symmetry in an array of gold nanoparticles*. *Optics Express*, 2004. **12**(22): p. 5418-5423.
56. Klein, M.W., et al., *Experiments on second-and third-harmonic generation from magnetic metamaterials*. *Optics Express*, 2007. **15**(8): p. 5238-5247.
57. Aouani, H., et al., *Multiresonant broadband optical antennas as efficient tunable nanosources of second harmonic light*. *Nano Letters*, 2012. **12**(9): p. 4997-5002.
58. Thyagarajan, K., et al., *Enhanced second-harmonic generation from double resonant plasmonic antennae*. *Optics Express*, 2012. **20**(12): p. 12860-12865.
59. Fedotov, V.A., et al., *Sharp trapped-mode resonances in planar metamaterials with a broken structural symmetry*. *Physical Review Letters*, 2007. **99**(14): p. 147401.
60. Aydin, K., I.M. Pryce, and H.A. Atwater, *Symmetry breaking and strong coupling in planar optical metamaterials*. *Optics Express*, 2010. **18**(13): p. 13407-13417.
61. Savinov, V. and N.I. Zheludev, *High-quality metamaterial dispersive grating on the facet of an optical fiber*. *Applied Physics Letters*, 2017. **111**(9): p. 091106.
62. Makarov, S.V., et al., *Efficient second-harmonic generation in nanocrystalline silicon nanoparticles*. *Nano Letters*, 2017. **17**(5): p. 3047-3053.
63. Zhang, Y., et al., *Three-dimensional nanostructures as highly efficient generators of second harmonic light*. *Nano Letters*, 2011. **11**(12): p. 5519-23.
64. Park, S., J.W. Hahn, and J.Y. Lee, *Doubly resonant metallic nanostructure for high conversion efficiency of second harmonic generation*. *Optics Express*, 2012. **20**(5): p. 4856-4870.
65. Ning, T., et al., *Enhancement of second-harmonic generation from silicon nitride with gold gratings*. *Optics Express*, 2015. **23**(24): p. 30695-30700.
66. Valev, V.K., et al., *Nanostripe length dependence of plasmon-induced material deformations*. *Optics Letters*, 2013. **38**(13): p. 2256-2258.
67. Park, I.-Y., et al., *Generation of EUV radiation by plasmonic field enhancement using nanostructured bowties and funnel-waveguides*. *Annalen der Physik*, 2013. **525**(1-2): p. 87-96.
68. Pfullmann, N., et al., *Nano-antenna-assisted harmonic generation*. *Applied Physics B*, 2013. **113**(1): p. 75-79.
69. Ning, T., et al., *Efficient second-harmonic generation in silicon nitride resonant waveguide gratings*. *Optics Letters*, 2012. **37**(20): p. 4269-4271.
70. Bloembergen, N., R.K. Chang, and C.H. Lee, *Second-harmonic generation of light in reflection from media with inversion symmetry*. *Physical Review Letters*, 1966. **16**(22): p. 986-989.
71. Wokaun, A., et al., *Surface second-harmonic generation from metal island films and microlithographic structures*. *Physical Review B*, 1981. **24**(2): p. 849-856.
72. Bloembergen, N., *Nonlinear optics - Past, Present, and Future*. *IEEE Journal of Quantum Electronics*, 1984. **20**(6): p. 556-558.
73. Dick, B., et al., *Determination of the nonlinear optical susceptibility  $\chi^{(2)}$  of surface-layers by sum and difference frequency generation in reflection and transmission*. *Applied Physics B-Photophysics and Laser Chemistry*, 1985. **38**(2): p. 107-116.
74. Cazzanelli, M. and J. Schilling, *Second order optical nonlinearity in silicon by symmetry breaking*. *Applied Physics Reviews*, 2016. **3**(1): p. 011104.
75. Tian, C.S. and Y.R. Shen, *Recent progress on sum-frequency spectroscopy*. *Surface Science Reports*, 2014. **69**(2-3): p. 105-131.
76. Crawford, M.J., et al., *Second harmonic generation from the air/water interface of an aqueous solution of the dipeptide Boc-Trp-Trp*. *Chemical Physics Letters*, 1994. **230**(3): p. 260-264.

## Bibliography

77. Byers, J.D., H.I. Yee, and J.M. Hicks, *A second harmonic generation analog of optical-rotatory dispersion for the study of chiral monolayers*. Journal of Chemical Physics, 1994. **101**(7): p. 6233-6241.
78. Maki, J.J., et al., *Comparison of linearly and circularly polarized probes of second-order optical activity of chiral surfaces*. Journal of Chemical Physics, 1996. **105**(2): p. 767-772.
79. Petrallimallow, T., et al., *Circular-dichroism spectroscopy at interfaces - A surface second harmonic-generation study*. Journal of Physical Chemistry, 1993. **97**(7): p. 1383-1388.
80. Gotz, T., et al., *Optical second-harmonic generation by supported metal-clusters - Size and shape effects*. Applied Physics a-Materials Science & Processing, 1995. **60**(6): p. 607-612.
81. Dadap, J.I., et al., *Second-harmonic rayleigh scattering from a sphere of centrosymmetric material*. Physical Review Letters, 1999. **83**(20): p. 4045-4048.
82. Shen, Y.R., *Surface contribution versus bulk contribution in surface nonlinear optical spectroscopy*. Applied Physics B-Lasers and Optics, 1999. **68**(3): p. 295-300.
83. Bozhevolnyi, S.I. and V.Z. Lozovski, *Second-harmonic scanning optical microscopy of individual nanostructures*. Physical Review B, 2002. **65**(23).
84. Finazzi, M., et al., *Selection rules for second-harmonic generation in nanoparticles*. Physical Review B, 2007. **76**(12): p. 125414.
85. Zeng, Y. and J.V. Moloney, *Volume electric dipole origin of second-harmonic generation from metallic membrane with noncentrosymmetric patterns*. Optics Letters, 2009. **34**(18): p. 2844-2846.
86. Zeng, Y., et al., *Classical theory for second-harmonic generation from metallic nanoparticles*. Physical Review B, 2009. **79**(23): p. 235109.
87. Zhou, R.L., et al., *Second-harmonic generation from a periodic array of noncentrosymmetric nanoholes*. Journal of the Optical Society of America B-Optical Physics, 2010. **27**(11): p. 2405-2409.
88. Capretti, A., et al., *Size-dependent second-harmonic generation from gold nanoparticles*. Physical Review B, 2014. **89**(12).
89. Smirnova, D., A.I. Smirnov, and Y.S. Kivshar, *Multipolar second-harmonic generation by Mie-resonant dielectric nanoparticles*. Physical Review A, 2018. **97**(1): p. 013807.
90. Linden, S., et al., *Collective effects in second-harmonic generation from split-ring-resonator arrays*. Physical Review Letters, 2012. **109**(1): p. 015502.
91. Kruk, S., et al., *Enhanced magnetic second-harmonic generation from resonant metasurfaces*. ACS Photonics, 2015. **2**(8): p. 1007-1012.
92. Salomon, A., et al., *Size and shape resonances in second harmonic generation from silver nanocavities*. The Journal of Physical Chemistry C, 2013. **117**(43): p. 22377-22382.
93. Liu, S., et al., *Resonantly enhanced second-harmonic generation using III-V semiconductor all-dielectric metasurfaces*. Nano Letters, 2016. **16**(9): p. 5426-5432.
94. Cox, J.D. and F. Javier García de Abajo, *Electrically tunable nonlinear plasmonics in graphene nanoislands*. Nature Communications, 2014. **5**: p. 5725.
95. Satitkovitchai, K., Y. Pavlyukh, and W. Hubner, *Ab initio embedded cluster study of optical second-harmonic generation below the gap of a NiO(001) surface*. Physical Review B, 2003. **67**(16).
96. Lefkidis, G. and W. Hubner, *Phononic effects and nonlocality contributions to second harmonic generation in NiO*. Physical Review B, 2006. **74**(15).
97. Mendoza, B.S., A. Gaggiotti, and R. Del Sole, *Microscopic theory of second harmonic generation at Si(100) surfaces*. Physical Review Letters, 1998. **81**(17): p. 3781-3784.
98. Mendoza, B.S. and W.L. Mochan, *Exactly solvable model of surface second-harmonic generation*. Physical Review B, 1996. **53**(8): p. 4999-5006.
99. Mochan, W.L. and B.S. Mendoza, *Second-harmonic generation at crystal-surfaces*. Journal of Physics-Condensed Matter, 1993. **5**(33A): p. A183-A184.
100. Schaich, W.L. and B.S. Mendoza, *Simple-model of second-harmonic generation*. Physical Review B, 1992. **45**(24): p. 14279-14292.
101. Mendoza, B.S. and W.L. Mochan, *Polarizable-bond model for second-harmonic generation*. Physical Review B, 1997. **55**(4): p. 2489-2502.

102. Bhagavantam, S. and P. Chandrasekhar, *Harmonic generation and selection rules in nonlinear optics*. Proceedings of the Indian Academy of Sciences - Section A, 1972. **76**(1): p. 13-20.
103. Valencia, C.I., E.R. Méndez, and B.S. Mendoza, *Second-harmonic generation in the scattering of light by two-dimensional particles*. Journal of the Optical Society of America B, 2003. **20**(10): p. 2150-2161.
104. Ray, P.C., *Size and shape dependent second order nonlinear optical properties of nanomaterials and their application in biological and chemical sensing*. Chemical Reviews, 2010. **110**(9): p. 5332-5365.
105. Sipe, J.E. and J. Van Kranendonk, *Macroscopic electromagnetic theory of resonant dielectrics*. Physical Review A, 1974. **9**(5): p. 1806-1822.
106. Adler, E., *Nonlinear optical frequency polarization in a dielectric*. Physical Review, 1964. **134**(A3): p. A728.
107. Scalora, M., et al., *Second- and third-harmonic generation in metal-based structures*. Physical Review A, 2010. **82**(4): p. 043828.
108. Balcou, P., A. L'Huillier, and D. Escande, *High-order harmonic generation processes in classical and quantum anharmonic oscillators*. Physical Review A, 1996. **53**(5): p. 3456-3468.
109. Tsui, Y.T., *An intuitive theory of optical second harmonic generation via coupled anharmonic Lorentz oscillator*. International Journal of Engineering Science, 1970. **8**: p. 525-528.
110. Mejia, J.E., et al., *Surface second-harmonic generation from Si(111)(1x1)H: Theory versus experiment*. Physical Review B, 2002. **66**(19): p. 195329.
111. Andreou, D. and L.M. Bali, *Frequency mixing in the scattering of light by harmonically bound electrons*. Nature, 1970. **225**(5239): p. 1239-1240.
112. Hayashi, M., et al., *Theory of time-resolved sum-frequency generation and its applications to vibrational dynamics of water*. The Journal of Physical Chemistry A, 2007. **111**(37): p. 9062-9069.
113. Gonella, G., et al., *Second harmonic and sum-frequency generation from aqueous interfaces Is modulated by interference*. Journal of Physical Chemistry C, 2016. **120**(17): p. 9165-9173.
114. Poutrina, E., et al., *Nonlinear oscillator metamaterial model: numerical and experimental verification*. Optics Express, 2011. **19**(9): p. 8312-8319.
115. Poutrina, E., D. Huang, and D.R. Smith, *Analysis of nonlinear electromagnetic metamaterials*. New Journal of Physics, 2010. **12**(9): p. 093010.
116. Shor Peled, M.H., et al., *Second-harmonic generation from subwavelength metal heterodimers*. Optics Express, 2020. **28**(21): p. 31468-31479.
117. Petschulat, J., et al., *Multipole nonlinearity of metamaterials*. Physical Review A, 2009. **80**(6): p. 063828.
118. Jiang, S., et al., *Crystal symmetry and polarization of high-order harmonics in ZnO*. Journal of Physics B: Atomic, Molecular and Optical Physics, 2019. **52**(22): p. 225601.
119. Svirko, Y.P. and N.I. Zheludev, *Polarization of light in nonlinear optics*. 1998: John Wiley & Sons.
120. Xu, J., E. Plum, and V. Savinov, *Toy model of second harmonic generation due to structuring of centrosymmetric films*. Optics Express, 2020. **28**(22): p. 33346-33354.
121. Savinov, V., V.A. Fedotov, and N.I. Zheludev, *Toroidal dipolar excitation and macroscopic electromagnetic properties of metamaterials*. Physical Review B, 2014. **89**: p. 205112
122. Shramkova, O. and A. Schuchinsky, *Harmonic generation and wave mixing in nonlinear metamaterials and photonic crystals (Invited paper)*. International Journal of RF and Microwave Computer-Aided Engineering, 2012. **22**(4): p. 469-482.
123. Kumar, N. and B. Suthar, *Advances in photonic crystals and devices*. 2019: CRC Press.
124. Slusher, R.E., *Nonlinear photonic crystals*. Vol. 10. 2003: Springer Science & Business Media.
125. Gómez, F.R., et al., *Defect mode in the bulk plasmon-polariton gap for giant enhancement of second harmonic generation*. Physical Review B, 2017. **96**(7): p. 075429.
126. Li, Z., et al., *Molecular construction from AgGaS<sub>2</sub> to CuZnPS<sub>4</sub>: defect-induced second harmonic generation enhancement and cosubstitution-driven band gap enlargement*. Chemistry of Materials, 2020. **32**(7): p. 3288-3296.

## Bibliography

127. Der Horst, C.A., S. Magnien, and S. Kapphan, *Variation of luminescence and second harmonic generation of defect polarization clusters induced by reduction in pure  $\text{KTaO}_3$  and  $\text{KTaO}_3: \text{Fe}$* . *Ferroelectrics*, 1996. **185**(1): p. 265-268.
128. Cunha, R., et al., *Second harmonic generation in defective hexagonal boron nitride*. *Journal of Physics: Condensed Matter*, 2020. **32**(19): p. 19LT01.
129. Tsai, T.E., et al., *Correlation of defect centers with second-harmonic generation in Ge-doped and Ge-P-doped silica-core single-mode fibers*. *Optics Letters*, 1989. **14**(18): p. 1023-1025.
130. Tanuma, R. and H. Tsuchida, *Three-dimensional imaging of extended defects in 4H-SiC by optical second-harmonic generation and two-photon-excited photoluminescence*. *Applied Physics Express*, 2014. **7**(2): p. 021304.
131. Zhang, C., et al., *Defect-enhanced second-harmonic generation in  $(\text{Si}_m\text{Ge}_n)_p$  superlattices*. *Applied Physics Letters*, 1998. **72**(17): p. 2072-2074.
132. Bertocchi, M., et al., *Defects and strain enhancements of second-harmonic generation in Si/Ge superlattices*. *The Journal of Chemical Physics*, 2014. **140**(21): p. 214705.
133. Neethling, P.H., et al., *Second harmonic generation as a technique to probe buried interfaces*. *South African Journal of Science*, 2009. **105**: p. 282-284.
134. Yeganeh, M.S., et al., *Influence of heterointerface atomic structure and defects on second-harmonic generation*. *Physical Review Letters*, 1992. **69**(24): p. 3579-3582.
135. Sow, B.M., et al., *Enriched fluorescence emission from  $\text{WS}_2$  monoflake empowered by Au nanoexplorers*. *Advanced Optical Materials*, 2017. **5**(14): p. 1700156.
136. Zhang, P., et al.,  *$\text{MoS}_2$  nanosheets decorated with gold nanoparticles for rechargeable Li- $\text{O}_2$  batteries*. *Journal of Materials Chemistry A*, 2015. **3**(28): p. 14562-14566.
137. Lu, J., et al., *Improved photoelectrical properties of  $\text{MoS}_2$  films after laser micromachining*. *ACS Nano*, 2014. **8**(6): p. 6334-6343.
138. Venkatakrisnan, A., et al., *Microsteganography on  $\text{WS}_2$  monolayers tailored by direct laser painting*. *ACS Nano*, 2017. **11**(1): p. 713-720.
139. Bogaert, K., et al., *Diffusion-mediated synthesis of  $\text{MoS}_2/\text{WS}_2$  lateral heterostructures*. *Nano Letters*, 2016. **16**(8): p. 5129-5134.
140. Zhang, X.-Q., et al., *Synthesis of lateral heterostructures of semiconducting atomic layers*. *Nano Letters*, 2015. **15**(1): p. 410-415.
141. Vargas, A., et al., *Tunable and laser-reconfigurable 2D heterocrystals obtained by epitaxial stacking of crystallographically incommensurate  $\text{Bi}_2\text{Se}_3$  and  $\text{MoS}_2$  atomic layers*. *Science Advances*, 2017. **3**(7): p. e1601741.
142. Rosa, H.G., et al., *Second-harmonic spectroscopy for defects engineering monitoring in transition metal dichalcogenides*. *Advanced Optical Materials*, 2018. **6**(5): p. 1701327.
143. Zhou, L., et al., *Nonlinear optical characterization of 2D materials*. *Nanomaterials*, 2020. **10**(11): p. 2263.
144. Antony, A., et al., *Defect engineering, microstructural examination and improvement of ultrafast third harmonic generation in  $\text{GaZnO}$  nanostructures: a study of e-beam irradiation*. *Physical Chemistry Chemical Physics*, 2020. **22**(7): p. 4252-4265.
145. Antony, A., et al., *Improved third harmonic nonlinear optical process upon e-beam irradiation in Cl:  $\text{ZnO}$  thin films*. *Materials Science in Semiconductor Processing*, 2020. **114**: p. 105077.
146. Pattanayak, A., M.M. S, and G. Dixit, *Influence of vacancy defects in solid high-order harmonic generation*. *Physical Review A*, 2020. **101**(1): p. 013404.
147. Iravani, H., K.K. Hansen, and L.B. Madsen, *Effects of vacancies on high-order harmonic generation in a linear chain with band gap*. *Physical Review Research*, 2020. **2**(1): p. 013204.
148. Mrudul, M.S., et al., *High-harmonic generation from spin-polarised defects in solids*. *npj Computational Materials*, 2020. **6**(1): p. 10.
149. Xu, J., et al., *Second harmonic generation in amorphous silicon-on-silica metamaterial*. *APL Photonics*, 2021. **6**(3): p. 036110.
150. Lee, J., et al., *Giant nonlinear response from plasmonic metasurfaces coupled to intersubband transitions*. *Nature*, 2014. **511**(7507): p. 65-69.



151. Nookala, N., et al., *Ultrathin gradient nonlinear metasurface with a giant nonlinear response*. Optica, 2016. **3**(3): p. 283-288.
152. Chang, T., et al., *Mimicking bio-mechanical principles in photonic metamaterials for giant broadband nonlinearity*. Communications Physics, 2020. **3**: p. 79.
153. Volkovskaya, I., et al., *Multipolar second-harmonic generation from high-Q quasi-BIC states in subwavelength resonators*. Nanophotonics, 2020. **9**(12): p. 3953-3963.
154. Alloatti, L., et al., *Second-order nonlinear silicon-organic hybrid waveguides*. Optics Express, 2012. **20**(18): p. 20506-20515.
155. Avrutsky, I. and R. Soref, *Phase-matched sum frequency generation in strained silicon waveguides using their second-order nonlinear optical susceptibility*. Optics Express, 2011. **19**(22): p. 21707-21716.
156. Cazzanelli, M., et al., *Second-harmonic generation in silicon waveguides strained by silicon nitride*. Nature Materials, 2012. **11**(2): p. 148-154.
157. Hon, N.K., et al., *Periodically poled silicon*. Applied Physics Letters, 2009. **94**(9): p. 091116.
158. Jacobsen, R.S., et al., *Strained silicon as a new electro-optic material*. Nature, 2006. **441**(7090): p. 199-202.
159. Rao, A. and S. Fathpour, *Second-harmonic generation in integrated photonics on silicon*. Physica Status Solidi (a), 2018. **215**(4): p. 1700684.
160. Castellán, C., et al., *On the origin of second harmonic generation in silicon waveguides with silicon nitride cladding*. Scientific Reports, 2019. **9**(1): p. 1088.
161. Khorasaninejad, M., et al., *Silicon nanowire arrays with enhanced optical properties*. Optics Letters, 2012. **37**(20): p. 4194-4196.
162. Wiecha, P.R., et al., *Enhanced nonlinear optical response from individual silicon nanowires*. Physical Review B, 2015. **91**(12): p. 121416.
163. Dev Choudhury, B., et al., *Surface second harmonic generation from silicon pillar arrays with strong geometrical dependence*. Optics Letters, 2015. **40**(9): p. 2072-2075.
164. Galli, M., et al., *Low-power continuous-wave generation of visible harmonics in silicon photonic crystal nanocavities*. Optics Express, 2010. **18**(25): p. 26613-26624.
165. An, Y.Q. and A.C. Diebold, *Transiently stimulated second-harmonic generation from silicon nanogratings*. Physical Review B, 2017. **96**(20): p. 201306.
166. Lee, K.T., et al., *Electrically biased silicon metasurfaces with magnetic Mie resonance for tunable harmonic generation of light*. ACS Photonics, 2019. **6**(11): p. 2663-2670.
167. Lin, H.H., et al., *Synthesis of second-order nonlinearities in dielectric-semiconductor-dielectric metamaterials*. Applied Physics Letters, 2017. **110**(11): p. 113103.
168. Lin, H.H., et al., *Electronic metamaterials with tunable second-order optical nonlinearities*. Scientific Reports, 2017. **7**(1): p. 9983.
169. Bernhardt, N., et al., *Quasi-BIC resonant enhancement of second-harmonic generation in WS<sub>2</sub> monolayers*. Nano Letters, 2020. **20**(7): p. 5309-5314.
170. Yuan, Q., et al., *Second harmonic and sum-frequency generations from a silicon metasurface integrated with a two-dimensional material*. ACS Photonics, 2019. **6**(9): p. 2252-2259.
171. Zhang, J., K.F. MacDonald, and N.I. Zheludev, *Near-infrared trapped mode magnetic resonance in an all-dielectric metamaterial*. Optics Express, 2013. **21**(22): p. 26721-26728.
172. Keren-Zur, S., et al., *Nonlinear beam shaping with plasmonic metasurfaces*. ACS Photonics, 2016. **3**(1): p. 117-123.
173. Segal, N., et al., *Controlling light with metamaterial-based nonlinear photonic crystals*. Nature Photonics, 2015. **9**(3): p. 180-184.
174. Gould, M., et al., *Ultra-thin silicon-on-insulator strip waveguides and mode couplers*. Applied Physics Letters, 2012. **101**(22): p. 221106.
175. Zou, Z., et al., *60-nm-thick basic photonic components and Bragg gratings on the silicon-on-insulator platform*. Optics Express, 2015. **23**(16): p. 20784-20795.